공학박사 학위논문

Development of wet-spinning process for manufacturing high-strength PAN fiber with improved spinnability

방사성이 향상된 고강도 PAN 섬유 제조를 위한 습식방사 공정 개발

2023 년 8 월

서울대학교 대학원

재료공학부

김 용 민

Development of wet-spinning process for manufacturing high-strength PAN fiber with improved spinnability

Advisor: Woong-Ryeol Yu

by

Yong Min Kim

2023

Department of Materials Science and Engineering Graduated School Seoul National University

Development of wet-spinning process for manufacturing high-strength PAN fiber with improved spinnability

방사성이 향상된 고강도 PAN 섬유 제조를 위한 습식방사 공정 개발

지도교수 유 웅 열

이 논문을 공학박사 학위논문으로 제출함

2023 년 8 월

서울대학교 대학원

재료공학부

김 용 민

김용민의 공학박사 학위논문을 인준함

2023 년 6 월

위 원 장 안 철 희 (인)

부 위 원 장 유 웅 열 (인)

위 원 이 명 규 (인)

위 원 이 병 선 (인)

위 원 양 호 성 (인)

Abstract

The use of polyacrylonitrile (PAN) fibers as precursors to carbon fibers has gained significant attention due to their excellent mechanical properties. Carbon fibers are widely employed in various fields for their high strength-to-weight ratio. However, while the industrial demand for the more advanced performance of the carbon fibers, have been rarely improved. Therefore, there is a need for research focused on enhancing the mechanical characteristics of PAN fibers, which directly affect carbon fiber performance.

In this study, electrochemical wet spinning was introduced to improve the mechanical properties of PAN fibers, and PAN design with enhanced spinnability was developed. Moreover, various variables in PAN wet spinning and electrochemical wet spinning were optimized to produce high-strength PAN fibers. By designing cations within PAN suitable for electrochemical wet spinning, PAN was polymerized and spun into fibers. Experimental evaluation of the resulting fibers' microstructure and mechanical properties confirmed their suitability for electrochemical wet spinning. The ionized PAN led to altered diffusion rates of solvents and non-solvents during the coagulation process, minimizing the formation of voids within the PAN fibers and enhancing their mechanical properties. Furthermore, it was challenging to introduce electrochemical wet spinning using commonly available cations without PAN. Hence, a PAN spinning solution with added lithium salt was prepared to achieve electrical conductivity. The inclusion of lithium salt in the spinning solution accelerated ionization upon the applied electrical

potential, maximizing the effect of electrochemical reactions on the enhancement of fiber properties. Additionally, various concentrations of lithium salt were explored to determine the optimum concentration within the spinning solution.

To investigate the influence of moisture on PAN fibers, uniform water vapor was applied to PAN. The PAN fibers with uniformly deposited moisture were then fabricated using conventional wet spinning and electrochemical wet spinning methods. The incorporation of a small amount of moisture minimized the formation of voids within the manufactured fibers and improved their mechanical properties. In the case of electrochemical wet spinning, higher moisture content resulted in further enhancements in mechanical characteristics.

To further enhance the mechanical properties and spinnability of PAN fibers, a bimodal molecular weight distribution of PAN was designed. The presence of low molecular weight PAN reduced the viscosity and increased the spinnability of the fibers. Moreover, the differential solidification process between high molecular weight PAN and low molecular weight PAN improved the crystalline structure within the fibers and enhanced their mechanical properties. Through the fabrication of bimodal molecular weight distribution PAN fibers with various mixing ratios and molecular weight ratios, an optimal combination was identified, resulting in improved spinnability and mechanical properties.

Keywords: PAN fiber, electrochemical wet-spinning, mechanical properties, microstructure, bimodal molecular weight distribution, spinnability,

Student number: 2017-27050

Contents

List of figures

List of tables

Chapter 1. Introduction

1.1. PAN polymerization

In 1949, fibers derived from acrylonitrile polymers and copolymers were introduced to the textile market, manufactured by DuPont de Nemours [1]. During the 1950s to 1960s, a range of production technologies utilizing different copolymers of acrylonitrile and employing various solvents were implemented in the development of polyacrylonitrile (PAN) fibers. PAN is widely recognized as one of the essential polymer materials for fiber development due to its lightweight nature, abrasion resistance, exceptional mechanical properties, and resistance to insects, among other advantages [1, 2]. Additionally, PAN is a highly versatile polymer thanks to its elevated carbon content. The presence of a carbon-carbon backbone ensures remarkable biostability and resistance to degradation [3].

The properties of PAN fiber are significantly influenced by its raw material, PAN. PAN is usually prepared by radical polymerization [4-6]. Radical polymerization is a polymerization process that involves the sequential addition of reactive monomers through the initiation, propagation, chain transfer, and termination steps. Initiation occurs when initiators decompose, generating radicals, through heat or light. The generated radicals initiate the polymerization process by reacting with other monomers, leading to the elongation of polymer chains, known as propagation. During propagation, chain transfer reactions can also occur, where radicals are transferred to other chains or monomers. Termination reactions take place when

radicals at the end of chains couple with other radicals, resulting in their annihilation, or when they react with impurities or inhibitors, leading to the termination of radicals. PAN can also be synthesized through ionic polymerization methods, such as anionic polymerization. [7-9]. However, in the case of ionic polymerization methods, including anionic polymerization, the "living" character of the polymerization process can be compromised due to side reactions [7].

Solution polymerization and suspension polymerization are commonly utilized methods in PAN polymerization, typically carried out through radical polymerization. [10]Solution polymerization is a method in which PAN is polymerized within a solvent capable of dissolving PAN, such as DMF, DMSO, or DMAc. In this process, the monomer and radical initiator are added to the solvent, and the PAN polymerization takes place within the solution [11].

Suspension polymerization is a method of PAN polymerization where the monomer and radical initiator are added to a non-solvent, such as water, in which PAN is not soluble. The polymerization reaction takes place within the non-solvent, resulting in the formation of PAN particles suspended in the medium [12]. Persulfate such as a,a'-azobis-isobutyronitile (AIBN) or redox initiators are commonly used as radical initiators in PAN polymerization.

Extensive research has been focused on improving the mechanical propertie s of PAN-based carbon fibers through the design of precursor sources. To a chieve this, two main approaches are commonly pursued: enhancing the prop erties of PAN fibers and improving the heat treatment.

To enhance the properties of PAN fibers and improving heat treatment, cop olymer designs to low stabilization temperature, reduced centralized heat rele ase [13-23], and increasing the spinnability [16, 24]. Many copolymers based on acrylonitrile (AN), including methyl acrylate (MA), methacrylic acid (MAA), itaconic acid (IA), methyl methacrylate (MMA), and acrylic acid (AA), have been extensively studied to enhance the stabilization and spinnability of PAN fibers [16]. Specifically, acidic comonomers such as MAA, IA, and AA are incorporated to lower the cyclization temperature and increase the hydrophilicity of PAN fibers. On the other hand, neutral comonomers like MA and MMA are utilized to improve the solubility, drawability, and spinnability of PAN fibers [16, 25].

In addition to enhancing the properties of PAN fibers, various strategies have been explored, including increasing the molecular weight of PAN [12, 26-28] and reducing the polydispersity index (PDI) [29-31]. It is widely recognized that there is a significant correlation between the increase in molecular weight and the improvement of mechanical properties. The high density of entanglement between polymer chains greatly contributes to the enhancement of their mechanical properties [12, 28]. However, it should be noted that an increase in molecular weight results in a significant rise in viscosity, leading to a decrease in spinnability. So, researchers have designed polymerization methods such as reversible addition-fragmentation chain-transfer (RAFT) [29, 31, 32] and atom transfer radical polymerization (ATRP) [30, 33] to reduce the viscosity of PAN

1.2. Conventional manufacturing of PAN fibers

In 1949, fibers derived from acrylonitrile polymers and copolymers were introduced to the textile market, manufactured by DuPont de Nemours [1]. During the 1950s to 1960s, a range of production technologies utilizing different copolymers of acrylonitrile and employing various solvents were implemented in the development of polyacrylonitrile (PAN) fibers. PAN is widely recognized as one of the essential polymer materials for fiber development due to its lightweight nature, abrasion resistance, exceptional mechanical properties, and resistance to insects, among other advantages [1, 2]. Additionally, PAN is a highly versatile polymer thanks to its elevated carbon content. The presence of a carbon-carbon backbone ensures remarkable biostability and resistance to degradation [3].

The remarkable strength-to-weight ratio displayed by carbon fiber makes it an incredibly sought-after material in industries such as aerospace, automotive, and sporting goods [34-39]. PAN, a polymer composed of interconnected carbon chains, is characterized by its rigid, dense, and relatively insoluble nature. Additionally, it exhibits a high melting point, making it a durable and robust material [40]. Indeed, PAN fiber is commonly employed as a precursor fiber in the production of carbon fibers. This is primarily due to its ability to yield a high carbon content, resulting in thermally stable fibers with exceptional mechanical properties after undergoing high-temperature treatment [40-44]. Figure 1-1 depicts a schematic of a two-step heat treatment process involved in the conversion of PAN fiber into carbon fiber [45]. During the stabilization stage, the linear structure of PAN undergoes a transformation

into a more thermally stable ladder bonding structure. In the carbonization process, non-carbon atoms are eliminated through side-group elimination [45, 46].

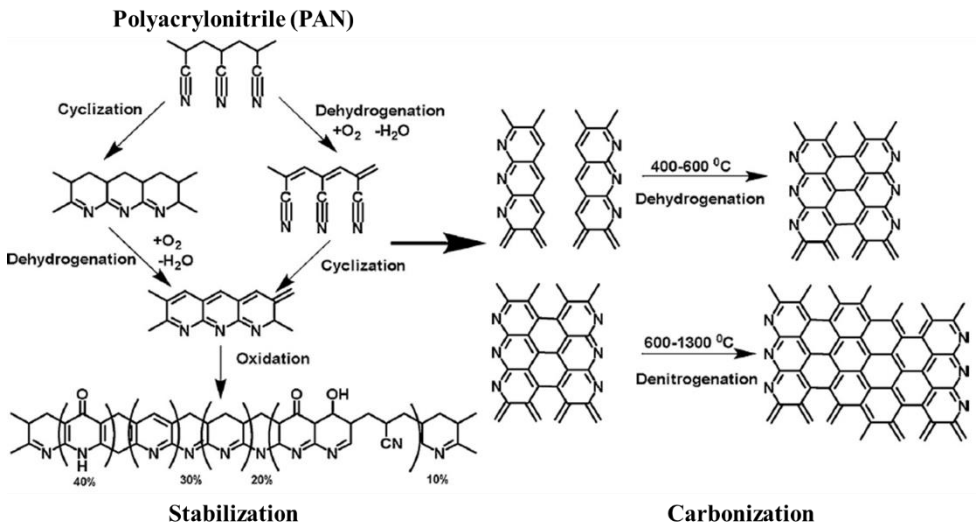

Figure 1-1. Two step processing of PAN into carbon fiber; oxidative stabili zation process (left); carbonization (right). Gained from reference [45].

PAN fiber exists in both semi-crystalline and amorphous forms, and its properties are influenced by the presence of defects. The physical, chemical, electrical, mechanical, and thermal characteristics of PAN fiber are strongly influenced by its crystalline structures and the presence of defects. Therefore, high-quality PAN fibers should possess essential properties such as high crystallinity, strong orientation, and low defect density to ensure optimal performance. [3, 47]. Extensive research has been dedicated to enhancing the mechanical properties of PAN fibers, with the aim of improving the mechanical performance of carbon fibers [34-36, 48-54].

Wet spinning is an established and well-developed technology used for the production of fibers from polymer solutions. Wet spinning is a process used to create fibers by extruding a polymer solution into a coagulation bath containing non-solvent. Figure 1-3 shows A schematic diagram of the wet spinning process [55]. Wet-spun fibers are fabricated by washing the nascent fibers generated in the coagulation bath with non-solvent in several washing baths and hot rollers, followed by drawing and drying at high temperatures. During the coagulation process, a dope solution is extruded into the coagulation bath, where the solvent of the dope solution diffuses into the mixed solution (solvent and non-solvent) in the bath. The non-solvent is absorbed into the dope solution to form nascent fibers [56, 57].

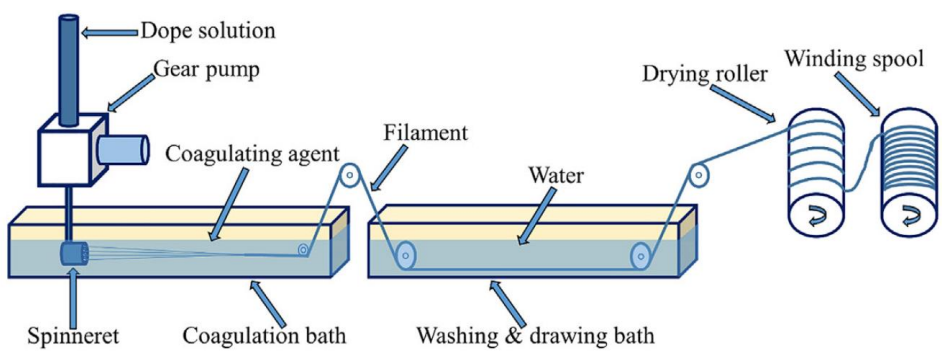

Figure 1-2. A schematic diagram of the wet spinning process. Gained from reference [55].

Due to melting temperature of PAN being higher than its thermal decomposition temperature at 317°C, melt spinning is not suitable for PAN fabrication. While electrospinning has been extensively researched, it is not suitable for large-scale production. Therefore, solution spinning methods are employed. PAN possesses

polarity due to the presence of nitrile (-CN) groups, which allows it to dissolve well in solvents such as DMF, DMSO, DMAc, and ionic liquids, making solution spinning a suitable option. Solution spinning can be carried out using dry spinning or wet spinning techniques. In dry spinning, the solvent must evaporate during extrusion, causing the fiber to solidify. However, PAN fibers produced through dry spinning face difficulties as the low evaporation rate of the solvent leads to reduced elongation properties. As a result, PAN fibers are generally produced using the wet spinning method.

Extensive research has been focused on improving the mechanical properties of PAN-based carbon fibers through the design of precursor sources. Studies have been conducted to optimize the process parameters related dope solution, coagulation bath and drawing process parameter of wet spinning in order to enhance the properties of PAN fibers [58-63]. The coagulation process in the wet-spinning is a critical step that significantly impacts the mechanical properties of the fabricated PAN fibers. Several factors, such as the, solution homogeneity [64-66], coagulation bath temperature [67], ratio of solvent and non-solvent [50], and jet-stretch [51], influence the coagulation process. These factors can affect diffusion rate of solvent and non-solvent in the coagulation bath. It is widely accepted that the diffusion rate of solvent and non-solvent plays a significant role in determining the microstructure and mechanical properties of the PAN fibers.

1.3. Electrochemical wet-spinning

Numerous research has been conducted on the wet-spinning process parameters for enhancing the properties of PAN fibers for a long time. As a result, optimization of the existing process parameters has been extensively studied. However, the demand for improved properties of PAN-based carbon fibers has been increasing. This is particularly evident in the quest for strength enhancement, as the current stre ngth of carbon fibers is less than 10% of the theoretical tensile strength [6 8].Therefore, new process parameters is necessary for enhancing mechanical properties of PAN fiber. Since the microstructure of PAN fibers fabricated by wet spinning is influenced by the coagulation process, new process parameters have been introduced to this stage. These new parameters aim to control the non-solvent diffusion rate in coagulation process, thereby affecting the resulting microstructure and enhancing the properties of PAN fibers.

In the coagulation process of wet spinning, the solvent from the dope solution diffuses into the coagulation bath, while the non-solvent in the bath diffuses into the extruded dope solution. Variations in the diffusion rates of the solvent and non-solvent have a direct impact on the resulting microstructure. When the diffusion rates of the solvent and non-solvent are comparable, the microstructure tends to exhibit greater perfection. However, in most cases, the diffusion rate of the solution is faster than that of the non-solvent. Consequently, increasing the diffusion rate of the non-solvent can contribute to achieving a more ideal microstructure. However, PAN, being a hydrophobic polymer, possesses hydrophobic characteristics due to its

molecular structure, specifically the nitrile (–CN) group found in its unit structure [69, 70]. and its hydrophobicity is attributed to its molecular structure; PAN is a polyethylene derivative having a nitrile (–CN) group in the unit structure [70]. Although the hydroneutral nitrile group can form hydrogen bonds with water molecules, the presence of strong dipole-dipole interactions among nitrile groups in PAN hinders bonding with water molecules [71]. Unfortunately, the conversion of the nitrile group into another group cannot be employed in the synthesis of carbon fiber precursors, as the presence of the nitrile group is essential for the formation of the carbonaceous microstructure during thermal treatment [72]. However, modifying the comonomer used in PAN copolymer fabrication can offer electrical potential solution to impart hydrophilic and hygroscopic characteristics to the precursor fiber.

An "Electrochemical wet-spinning" process was designed wherein electrical potential is applied to the dope solution [73]. Figure 1-3 illustrates the reactions occurring during the electrochemical wet-spinning process [73]. In Figure 1-3 (a), a schematic representation showcases the molecular changes and water absorption observed during the electrochemical wet-spinning process, with a focus on the spinneret and coagulation bath. Through electrochemical oxidation, the PAN undergoes ionization, leading to the formation of hydrophilic functional groups. These hydrophilic groups readily facilitate hydration, allowing for increased water uptake within the system [74, 75]. To introduce hydrophilic properties into the PAN copolymer, modification strategy involved the intentional design of methyl acrylate conversion. This conversion was targeted at achieving electrochemical

demethylation within the spinneret, effectively transforming the hydrophobic PAN copolymer into a hydrophilic and hygroscopic material. Under the influence of an electric potential, the methyl acrylate groups present in PAN copolymers, which were initially dissolved in DMF, underwent a conversion process, resulting in the formation of carboxylate moieties. Following this modification, the polymer was subjected to the solidification process in a water/DMF coagulation bath, leading to its hydration. The incorporation of water during this stage facilitated the solidification and transformation of the modified polymer into a hydrated state. In Figure 1-3 (b), a schematic representation illustrates the molecular transformations during heat-stretching in both conventional and electrochemical wet-spinning processes. During this stage, the polymer molecules undergo partial orientation, leading to improved alignment. As the coagulation process takes place, water molecules effectively penetrate both the polymer and DMF solvent molecules. This contributes to the solidification and hydration of the polymer, playing a significant role in shaping the final structure and properties of the fiber in both wet-spinning processes. In the conventional wet-spinning of PAN, the formed molecules exhibit a lamellar structure with relatively large voids. However, in the case of electrochemical wet-spinning of PAN copolymers, a distinct difference is observed. The copolymer molecules are arranged in a more parallel manner, resulting in smaller voids. This difference in morphology is attributed to the presence of absorbed water molecules during the electrochemical process. The absorbed water molecules play a vital role in enhancing the chain mobility of the polymer, facilitating a more organized and parallel arrangement of the copolymer molecules,

ultimately leading to the formation of a finer and more compact structure with reduced voids [76, 77]. So, the mechanical properties of the electrochemical wet-spun fibers stronger than those of conventional wet-spun fibers.

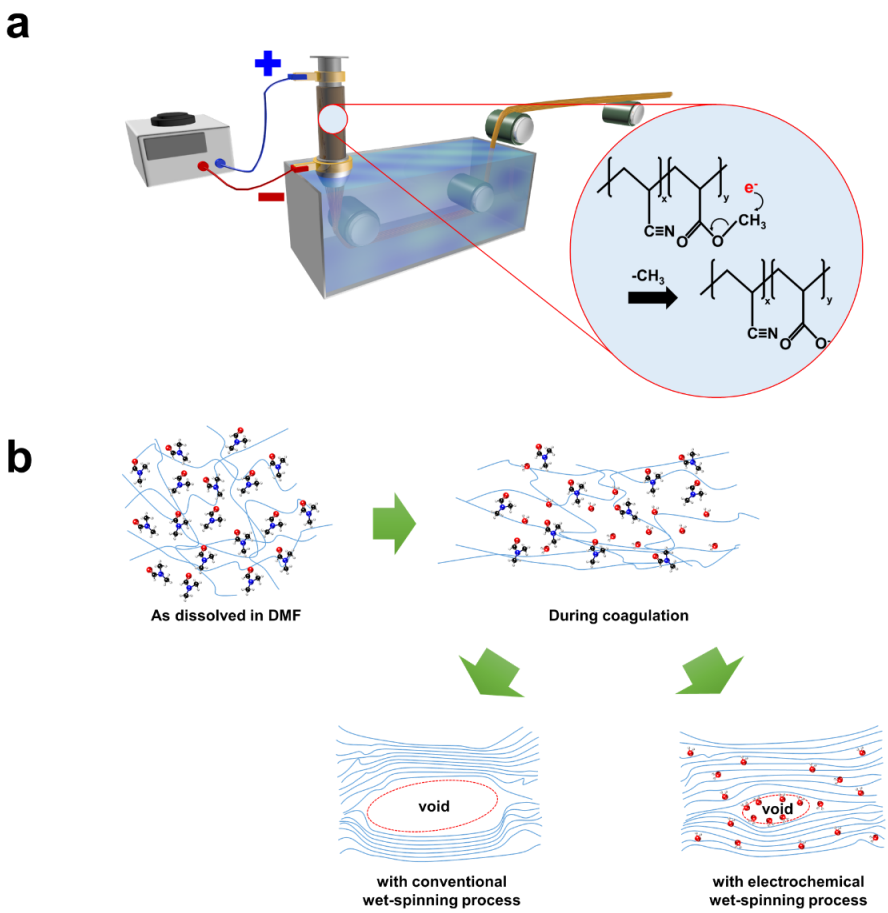

Figure 1-3 Schematic diagrams of (a) the electrochemical wet-spinning process and (b) the molecular changes occurring during the wet-spinning processes [73].

1.4. Research objectives

In this thesis, the main objective is development of wet-spinning process for manufacturing high-strength PAN fiber improved spinnabiltiy. For those purpose the wet spinning method was improved by introducing various process parameters, and a new PAN was designed accordingly.

In chapter 2, PAN was designed to be cations within PAN by applying an electrical potential, making it suitable for electrochemical wet-spinning. The PAN copolymer was modified to incorporate neutral comonomers that enhance spinnability, while specific modifications at the chain ends enabled ionization solely through electrical potential. The newly designed PAN solution was investigated for its reaction behavior under electrical potential, and PAN fibers were subsequently manufactured using both conventional and electrochemical wet-spinning methods. The microstructure was characterized using 2D-WAXS and 2D-SAXS, and the mechanical properties were evaluated through single fiber tensile tests.

In chapter 3, PAN dope solution was prepared by incorporating salt into a cations without PAN, aiming to achieve an effective electrochemical wet-spinning process. PAN fibers were then manufactured using conventional wet-spinning and electrochemical wet-spinning methods, utilizing a solvent capable of dissolving PAN and a lithium salt that could dissolve in the solvent. The impact of lithium salts on thermal treatment was examined using differential scanning calorimetry. The effects of lithium salts on the electrochemical wet-spinning process were assessed through

microstructural analysis and mechanical property measurements. The optimal lithium salt concentration for mechanical property of PAN fiber was experimentally demonstrated.

In chapter 4, the optimization of water content, which influences the properties of PAN fiber, was investigated. Complete removal of moisture from PAN was achieved, and for uniform water distribution, moisture was applied to PAN in high humidity condition. Furthermore, fibers were manufactured using conventional wet-spinning and electrochemical wet-spinning methods, and the microstructure and mechanical properties were examined. The study also presented the optimized water content for the wet-spinning process.

In chapter 5, bimodal molecular weight distribution PAN was designed to enhance the mechanical properties and spinnability of PAN fibers. Bimodal molecular weight distribution PAN fibers were manufactured by blending high molecular weight PAN for improved mechanical properties and low molecular weight PAN for enhanced spinnability. The spinnability of the PAN dope solution was characterized through rheological behavior analysis. Additionally, the microstructure analysis and mechanical property measurements of the bimodal molecular weight distribution PAN fibers were conducted to determine the optimal ratio of low and high molecular weight PAN. The study also presented the appropriate molecular weight ratio for bimodal molecular weight distribution PAN fibers with various molecular weight ratios.

Chapter 2. Cations in PAN polymer and electrochemical wet-spinning

In this chapter, the method is proposed to increase the hydrophilicity and hygroscopicity of the comonomer, thereby enhancing the diffusion rate of the non-solvent. This is achieved by employing redox polymerization to attach cations to the PAN polymer chain end, making it ionizable. Furthermore, an electrical potential is applied to the dope solution containing ionizable PAN to increase the concentration of cations around the nozzle. The higher concentration of cations stabilizes the carboxyl group inside the comonomer, resulting in the separation of the methyl group ($-CH_3$) By increasing the concentration of cations in the dope solution through the applied electric potential, the hydrophilic properties of PAN are intensified, and the diffusion rate of the non-solvent during the coagulation process is enhanced. Consequently, this leads to an increased formation of smaller voids due to the absorbed non-solvent [73].

2.1. Preparation of PAN with cations

2.1.1. Polymerization of PAN with cations

Suspension polymerization was used to polymerize PAN with cations (NaPAN) [12, 35]. The monomer materials used were acrylonitrile (AN, 99%, Dajung Chemical), and methyl acrylate (MA, Sigma-Aldrich) was used as a comonomer. The copolymer ratio in PAN was targeted at 6wt%, and dimethylsulfoxide (DMSO, 99.5%, Dajung Chemical) was used as the solvent. Ammonium persulfate (APS, ≧98.0%, Sigma-Aldrich) and sodium bisulfite (SBS, Sigma-Aldrich) were used as initiators, and iron(II) sulfate heptahydrate ($FeSO4 \cdot 7H2O$, ≥99.0%, Sigma-Aldrich) was used as the catalyst. On the other hand, solution polymerization was used to polymerize PAN without cations (nonPAN) [78, 79]. The same monomers and solvents were used as in the suspension polymerization. However, a,a'-azobis-isobutyronitile (AIBN, 99%, Dajung Chemical) was recrystallized and used as the initiator. To recrystallize AIBN, an excess of AIBN was dissolved in ethanol at 40°C and left at -5°C for 1 day, after which the precipitated AIBN crystals were filtered. In both polymerization methods, the resulting nonPAN and NaPAN was washed several times with distilled water and methanol and then dried in a vacuum environment at 80°C after washing with water and methanol.

Polymerized nonPAN and NaPAN were characterized by various methods to confirm that they were polymerized as intended. Molecular weights of nonPAN and NaPAN were measured by gel permeation chromatography (GPC, Ultimate 3000,

Thermo). The metal element (cation) content of nonPAN and NaPAN was analyzed using an inductively coupled plasma-atomic emission spectrometer (ICP-AES, OPTIMA 8300, Perkin-Elmer). The composition of the comonomer of nonPAN and NaPAN was measured using a nuclear magnetic resonance spectrometer (NMR, Advance III-500, Bruker).

Table 2-1 and Table 2-2 shows the GPC and ^{1}H NMR analysis of nonPAN and NaPAN. The molecular weight of nonPAN was 471,000, and the molecular weight of NaPAN was 367,000. Due to the difference in molecular weight between nonPAN and NaPAN, the dope solution concentrations were prepared differently. The nonPAN solution was prepared at 16 wt%, and the NaPAN solution was prepared at 18 wt%. The comonomer (MA) ratios of nonPAN and NaPAN have similar values. Therefore, there is not much difference between the nonPAN and NaPAN fibers in terms of the amount of MA.

Table 2-3 shows the ICP-AES analysis results of nonPAN and NaPAN. The Na, Li and Fe contents of nonPAN and NaPAN were analyzed. Na was present at 779.05 ppm in NaPAN, but was relatively absent at 7.00 ppm in nonPAN. In addition, since the content of Fe used as the suspension polymerization catalyst was very small at 11.44 ppm. It was confirmed that all residues were removed through washing process after polymerization. PAN polymerized through redox polymerization has Na^{+} or H at the end of the chain [80].

Table 2-1. Molecular weight and polydispersity index(PDI) of nonPAN and NaPAN.

Sample	M_w	PDI
nonPAN	471,000	2.45
NaPAN	367,000	2.17

Table 2-2. ^{1}H NMR analysis of nonPAN and NaPAN.

Sample	AN (mol%)	MA (mol%)
nonPAN	96.74	3.26
NaPAN	96.31	3.69

Table 2-3. ICP-AES analysis of nonPAN and NaPAN.

Sample	Na (ppm)	Li (ppm)	Fe (ppm)
nonPAN	7.00	No	5.71
NaPAN	779.05	No	11.44

2.1.2. Cations effect in PAN dope solution

The rheological properties of the dope solution were measured using a rheometer (DHR-2, TA Instruments). The parallel plate on which dope solutions were placed 40 mm diameter and the solution size was 1 mm. Viscosity of the dope solutions was measured using flow sweeps in the shear rate range of 0.01 − 500 s^{-1}. The homogeneity of the dope solutions was investigated using frequency sweeps in each frequency range of 0.1 − 500 rad s^{-1}. Solution conductivity of dope solution was measured by conductivity meter (Con 610, Oakton). Morphologies of the PAN films and fibers were observed using field-emission scanning electron microscopes (FE-SEM, SUPRA 55VP from Carl Zeiss and SU8010 from Hitachi Co.).

The viscosity of several dope solutions was measured, including a solution of nonPAN and NaPAN dissolved in DMF. The viscosity of the 16 wt% nonPAN dope solution was 47.09 Pa·s, while the viscosity of the 18 wt% NaPAN dope solution is 17.13 Pa·s. Although the molecular weight of nonPAN is higher than that of NaPAN, the concentration of the dope solution was prepared to be small. However, the difference in viscosity between the dop e solutions is large compared to the difference in molecular weight and concentration. This is due to the difference in polymerization method, which prevents the formation of branches through ketone formation during polymerization [81]. This results in lower interchain entanglement in the dope solution, reducing its viscosity. NaPAN solutions are transparent, whereas nonPAN solutions appear yellow, which is also due to the difference in polymerization methods. Coloration appears as a conjugated reaction of the nitrile

group (C≡N) of PAN, which occurs through interactions between intermolecular or intramolecular C≡N [82, 83]. nonPAN has many branches in the chain, leading to numerous interactions between C≡N, and it takes on the yellow coloration (Figure 2-1).

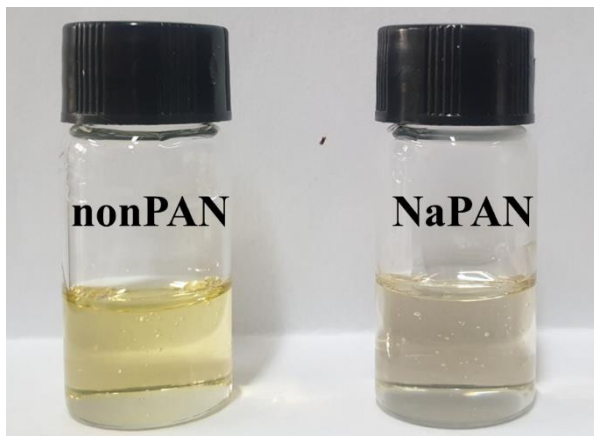

Figure 2-1. Photograph of nonPAN and NaPAN dope solution.

The conductivity of the prepared dope solutions was measured, and it was found that the solution conductivity of the NaPAN dope solution was 70.47 μS/cm, while that of the nonPAN dope solution was 2.04 μS/cm. Unlike nonPAN dope solution, NaPAN dope solution can conduct electricity in solution. When an electric potential is applied to the NaPAN solution, the Na^+ at the end groups of the polymer chains dissociate, allowing current to flow through the solution.

In order to analyze the chemical reaction occurring in the nozzle during electrochemical wet spinning, an insulating glass bottle and a nickel plate were used

as electrodes to apply an electric potential to the dope solution (Figure 2-2 (a), (b)). When a Ni plate is placed in the NaPAN dope solution and an electric potential is applied, bubbles and coloration occur at the (-) electrode of the solution. The colored NaPAN solution attached to the (-) electrode was dried at room temperature for one week to form a film, and the morphology and elements contained were measured by SEM and EDS. According to the EDS data, it was confirmed that Na was detected at a high percentage of 29.49% (Figure 2-2 (c)). In contrast, the nonPAN dope solution did not generate bubbles or coloration even when an electric potential was applied for a one week.

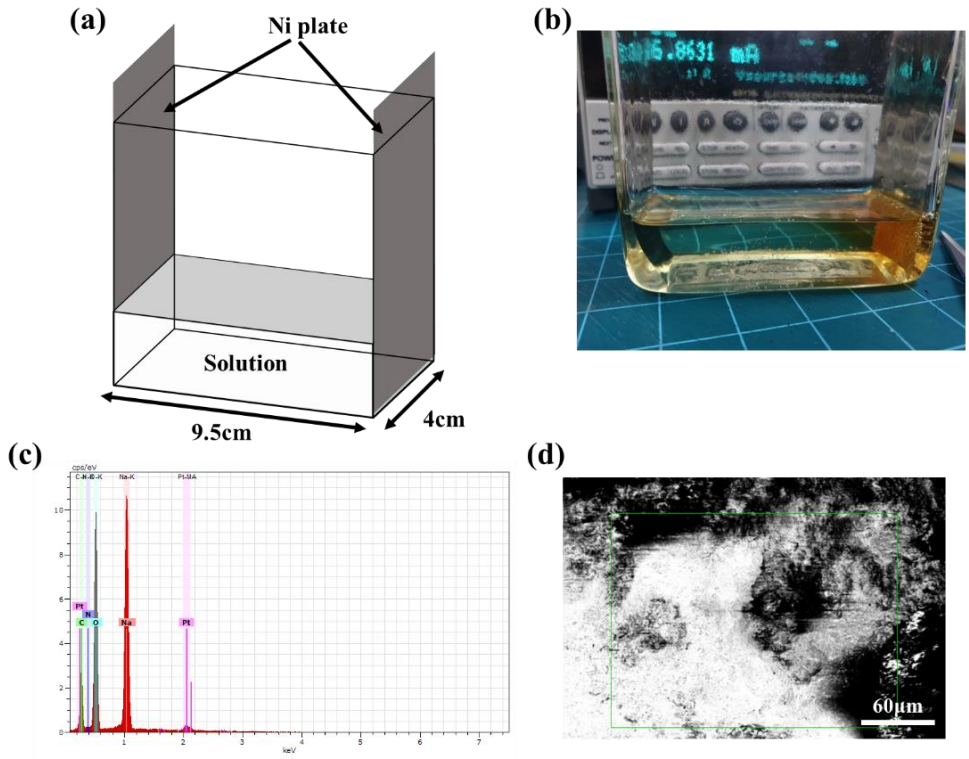

Figure 2-2. (a) Schematic illustrated reactor for applied electric potential at dope solution. (b) Photograph of reactor for applied electric potential at dope solution. (c) Energy-dispersive X-ray spectroscopy (EDS) data and (d) scanning electron microscopy (SEM) image of (-) electrode film of NaPAN dope solution.

The film attached to the (+) and (-) electrodes of NaPAN dope solution was analyzed by FT-IR (Figure 2-3). The FT-IR spectra of (+) electrode film display peaks due to AN and MA. Acrylonitrile peak is CH_2 vibrations (2930 and 2870 cm^{-1}, respectively), C≡N (2242 cm^{-1}), and CH_2 deformation (1452 cm^{-1})] and MA peak is C=O stretching (1732 cm^{-1}), CH_3-O deformation (1387 cm^{-1}), and C−O stretching (1253 and 1093 cm^{-1}) [84, 85]. Amide peak (1666 cm^{-1}) represented DMF in the film [86]. The FT-IR spectra of the (-) electrode film display peaks similar to that of stabilized PAN. Conjugate C=N stretching (1595 cm^{-1}) peak assigned cyclization reaction occurred in NaPAN dope solution [87]. When an electric potential is applied, the Na^+ trapped in NaPAN gather at the (-) electrode [88]. Due to the increase of Na^+, the interaction between CN and $COOCH_3$ occurs, leading to C≡N conjugated. As a result, coloration and cyclization reactions occur in (-) electrode of NaPAN dope solution.

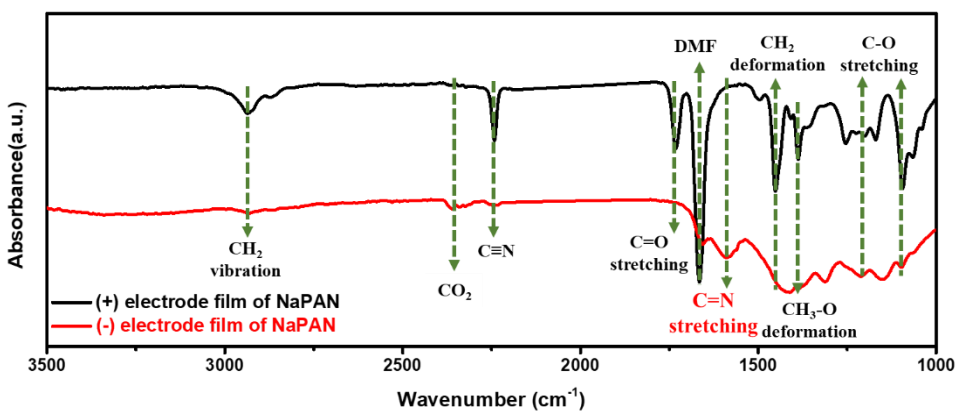

Figure 2-3. Fourier transform infrared (FT-IR) spectra of NaPAN film with both electrodes.

2.2. Electrochemical wet-spinning of PAN fibers

2.2.1. Process condition and characterization method

PAN was dissolved in N,N-Dimethylformamide (DMF; purity : 99.8%; high performance liquid chromatography (HPLC) grade, Daejung Chemical) to prepare a dope solution. The NaPAN and nonPAN were dissolved at concentrations of 18wt% and 16wt%, respectively. Lab-scale wet-spinning equipment setup consisting of a syringe pump, syringe set for electrochemical wet-spinning(insulated syringe, 100 holes conductive nozzle(100 μm in diameter) and conductive plunger), coagulation bath, three washing baths, drying unit, and winding unit was used to fabricate PAN fibers [73, 89]. The dope solutions were extruded to the coagulation bath filled with DMF and distilled water mixture (7:3) at a rate of 23.6 mL h^{-1} at room temperature. The jet stretch was 0.94. The coagulated PAN fibers were washed and stretched in three washing baths. The first washing bath filled with the DMF and water mixture (5:5) with a stretch ratio of 1.91, the second washing bath filled with water at 70 °C with a stretch ratio of 2.11, and the third washing bath filled with distilled water at 90 °C with a stretch ratio of 2.16. Residual DMF and water with fibers were removed at 70 °C in the drying zone. The PAN fibers were wound at the winding unit at a total stretch ratio of 8.18. Electrochemical wet- spinning was performed by applying 100 V via an electrometer (6517B, Keithley) to the conductive nozzle and plunger in syringe set for electrochemical wet-spinning.

Morphologies of the PAN fibers were observed using field-emission scanning

electron microscopes (FE-SEM, SUPRA 55VP from Carl Zeiss and SU8010 from Hitachi Co.). Chemical bonds in the films and fibers were assessed by fourier-transform infrared spectroscopy (FT-IR, Nicolet 6700, Thermo Fisher Scientific). The cyclization temperature of the fibers analysis by differential scanning calorimetry (DSC, 200 F3 Maia, NETZSCH) and thermos gravimetric analyzer (TGA, Discovery TGA, TA instruments). Temperature was increased to 400 °C heated at 10 °C/min under N_2. The microstructures of fibers were characterized by 2D wide-angle X-ray diffraction (2D-WAXD, D8 Discover; Bruker) and 2D small-angle X-ray scattering (2D-SAXS, Xeuss 2.0, Xenocs) [90, 91]. The radiation wavelength of 2D-WAXD and 2D-SAXS was 0.154 nm (Cu Kα). The mechanical properties of PAN fibers were measured using a single-fiber tester (FAVIMAT, Textechno, Mönchengladbach) with a 20 mm gage length and a crosshead speed of 20 mm/min. The tensile strength was analyzed using fiber diameters measured from FE-SEM images.

2.2.2. Basic characterization

The cross-section and surface morphology of the fibers were observed using SEM (Figure 2-4). Fibers fabricated of nonPAN were denoted nonPAN_C fiber and nonPAN_E fiber based on the manufacturing method, where nonPAN_C fiber was fabricated by conventional wet-spinning, and nonPAN_E fiber was fabricated by electrochemical wet-spinning. Likewise, Fibers fabricated of NaPAN were denoted NaPAN_C fiber and NaPAN_E fiber. The average diameters of the nonPAN_G, nonPAN_E, NaPAN_C and NaPAN_E fibers were measured as 11.87 ± 0.69, 11. 95 ± 0.84, 11.85 ± 1.34, and 11.49 ± 0.74 μm, respectively. There was little difference in morphology among the different polymers and fabrication methods. The cross-sectional shape of both nonPAN_C and nonPAN_E fibers was close to circular, with no significant difference between the two fibers. Comparing NaPAN_C fiber with the nonPAN_C fiber, some wrinkles appeared in NaPAN_C fiber due to the difference in diffusion rates of the solvent and non-solvent during the coagulation process [92]. The diffusion rate of the solvent and non-solvent changes due to the ion in the polymer and the molecular weight of the polymer. The increased Na^+ concentration in NaPAN_C fiber is believed to have increased the diffusion rate of the non-solvent. Comparing NaPAN_C fiber and NaPAN_E fiber, NaPAN_E fiber had relatively more wrinkles. Wrinkles were created because the diffusion rate of non-solvent increased due to the increase in Na^+ concentration. The increased diffusion rate of the non-solvent causes rapid solidification of the surface [93]. This restricts the diffusion inside the fiber, making the hard surface and flexible core,

which causes the fiber to contract and cause many wrinkles [35].

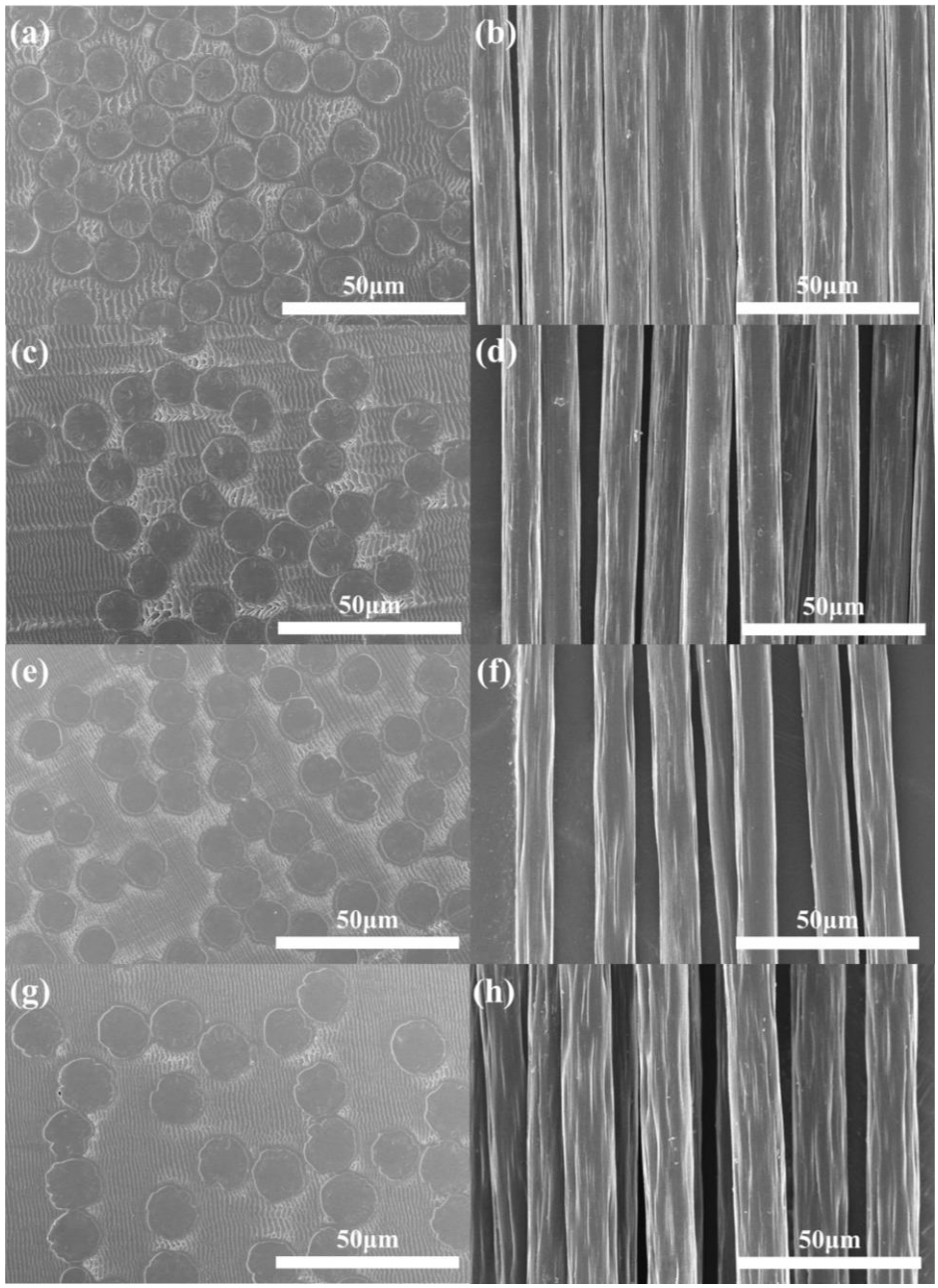

Figure 2-4. Scanning electron microscopy (SEM) images of the cross section and surface morphology (a,b) nonPAN_C, (c,d) nonPAN_E, (e,f) NaPAN_C and (g,h) NaPAN_E.

The chemical composition of the fibers was analyzed using FT-IR spectroscopy (Figure 2-5). Acrylonitrile peak is CH_2 vibrations (2930 and 2870 cm^{-1}, respectively), C≡N (2242 cm^{-1}), and CH_2 deformation (1452 cm^{-1})] and MA peak is C=O stretching (1732 cm^{-1}), CH_3-O deformation (1387 cm^{-1}), and C−O stretching (1253 and 1093 cm^{-1}) [84, 85]. Amide peak (1666 cm^{-1}) represented DMF in the film [86]. nonPAN_C, nonPAN_E, NaPAN_C and NaPAN_E fibers have simillar peak.

nonPAN_C, nonPAN_E, NaPAN_C and NaPAN_E fibers were analyzed by DSC to obtain heat flow values (Figure 2-6). It is observed that the peak values of nonPAN_C and nonPAN_E fibers are smaller than those of NaPAN fibers. This is a result of the difference in polymerization method. As described earlier, NaPAN polymerized through redox polymerization inhibits branching reactions due to ion-dipole bonding and aqueous state reactions. This facilitates intermolecular reactions and lowers the peak temperature [94]. When comparing NaPAN_C and NaPAN_E fibers, it can be seen that NaPAN_E fibers are broader than NaPAN_C fibers. This is similar to highly branched PAN, as the conjugation ratio increases with Na^+.

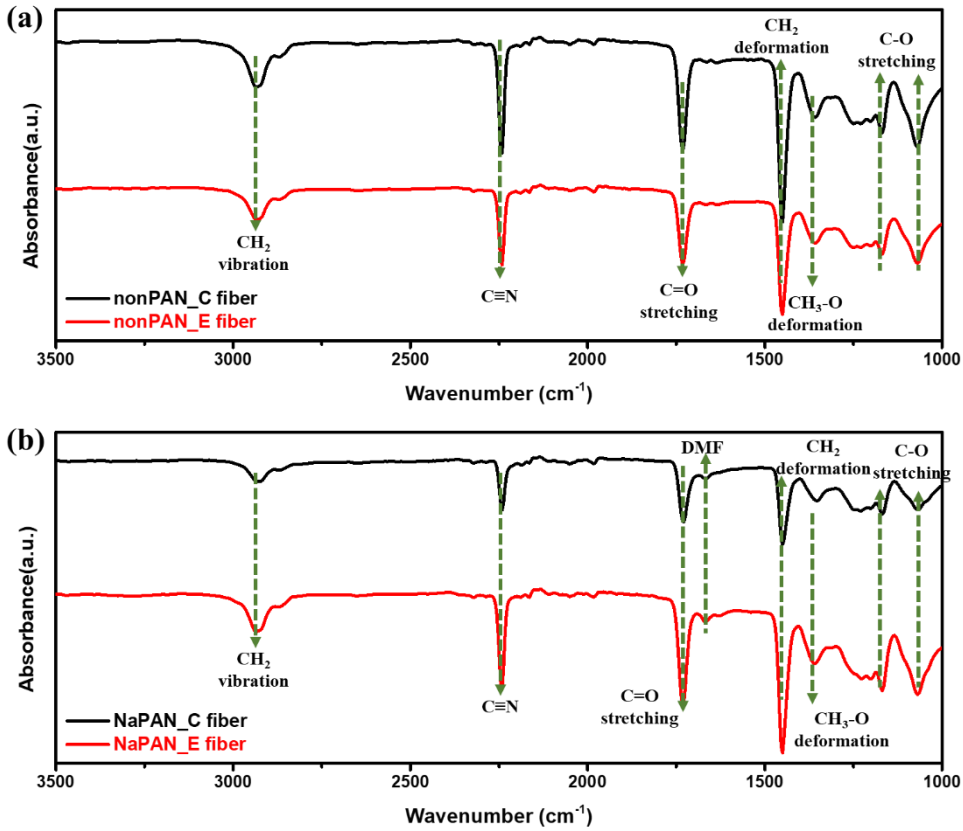

Figure 2-5. Fourier transform infrared spectra (FT-IR) of (a) nonPAN fibers, (b) NaPAN fibers.

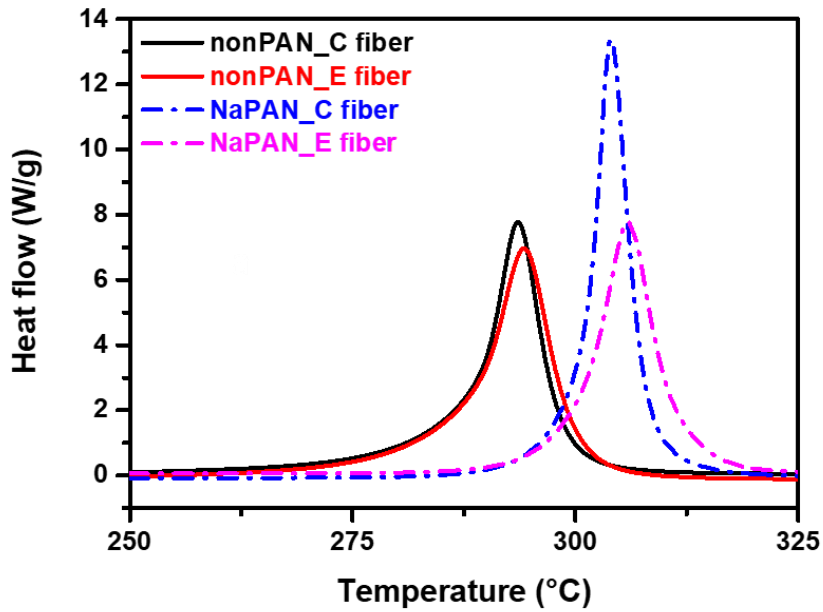

Figure 2-6. Differential scanning calorimetry (DSC) analysis of nonPAN and NaPAN fibers.

2.2.3. Microstructural characterization

The microstructure of a fiber critically affects its mechanical properties. And electrochemical wet-spinning significantly impacts on the microstructure [73, 89]. To investigate the microstructural changes induced by cation and electrochemical wet-spinning, 2D-WAXS and 2D-SAXS were used. The microstructure of the fibers was found to consist of polymer crystals, amorphous regions, and voids [89]. The polymer crystals were examined in detail using 2D-WAXD, which revealed that they had a preferred orientation along the fiber axes (Figure 2-7 (a)-(d)). Equatorially extracted one-dimensional WAXD curves showed two peaks, with a strong peak at $2\theta = 17°$ assigned to the (100) direction of the crystal, and a weaker peak at $2\theta = 27°$ assigned to the (110) direction of the PAN crystal [95].

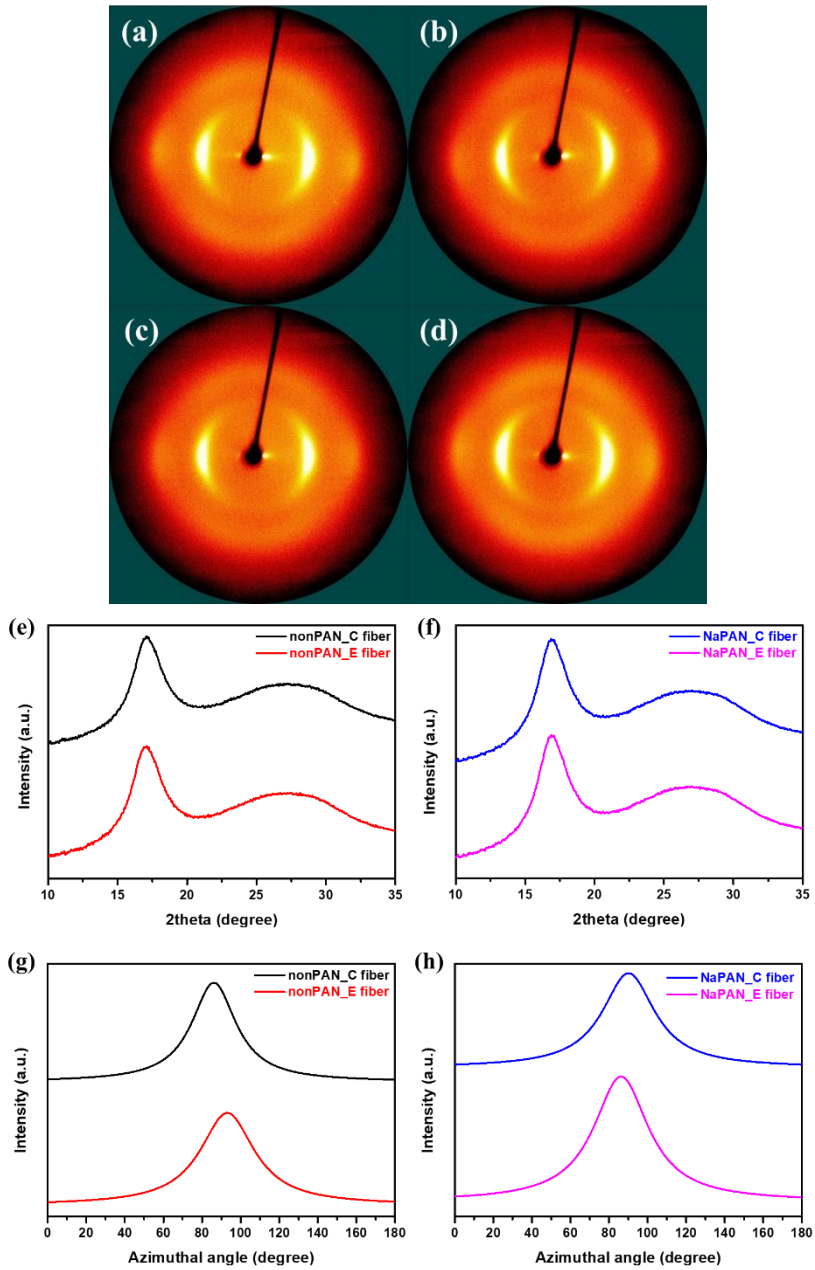

Figure 2-7. Microstructural characterization of the PAN fibers. Two-dimensional w ide-angle X-ray diffraction (2D-WAXD) images of (a) nonPAN_C fiber, (b) nonPAN_E, (c) NaPAN_C, and (d) NaPAN_E. Equatorially extracted one-dimensional WAXD curves of (e) nonPAN and (f) NaPAN fibers. Azimuthal scans at $2\theta = 17°$ of (g) nonPAN and (h) NaPAN fibers.

The crystallinity of the fibers was calculated using Hinrichsen's method (Equation (1)) [95, 96]. The calculated crystallinity of the nonPAN_C, nonPAN_E, NaPAN_C and NaPAN_E fibers were 57.56, 57.28, 56.17 and 55.91%, respectively (Table 2-4). The nonPAN_C and nonPAN_E fibers has slightly higher crystallinity than NaPAN_C and NaPAN_E fibers. The crystal size of the fibers was calculated using Equation (2), but it was found that the polymer and fabrication methods did not significantly affect the crystal size. The calculated crystal sizes for nonPAN_C, nonPAN_E, NaPAN_C and NaPAN_E, fibers were 3.40, 3.40, 3.33, and 3.42 nm, respectively (Table 2-4).

$$Crystallinty = \frac{A_c}{A_a + A_c} \tag{1}$$

where A_c is the sum of the areas of peaks and A_a is the sum of the amorphous areas.

$$L_c = \frac{K\lambda}{\beta cos\theta} \tag{2}$$

where L_c is the crystal size, K is the Scherrer parameter (0.89), λ is the wavelength (0.154 nm), and β is the full-width at half maximum(FWHM) of the peak at approximately 2θ = 17° [58, 97, 98].

The preferred orientations of fibers were calculated from peak integrations of the azimuthal scans at 2θ = 17° (Figure 2-7 (g), (h)). Preferred orientation which ranged from 80.24 to 84.05% also did not show significant differences between fibers. Due to polymerization and fabrication methods, there was no significant difference in the crystal structure of the fibers.

Table 2-4. Crystallinity and crystal size of nonPAN and NaPAN fibers.

Sample	Crystallinity (%)		Crystal size (nm)	
	Conventional	Electrochemical	Conventional	Electrochemical
nonPAN	57.56	57.28	3.40	3.40
NaPAN	56.17	55.91	3.33	3.42

Voids are considered as the starting point of fiber breakage and thus have a critical effect on mechanical properties of fiber. The voids in a fiber can be defined by their length and angle with axes of the fiber. Since the voids are initially formed in a cylindrical shape during coagulation and then elongate into a needle shape during fiber stretching. Ruland's streak method, which involves azimuthal scan of various scattering factors of 2D-SAXS, can be used to measure the void length and angle in the fiber (Figure 2-8) [58, 73, 99, 100].

$$s = |s| = 2\sin\theta/\lambda \tag{3}$$

where θ is the Bragg angle and λ is the wavelength of the incident X-ray beam (0.154 nm). The integral breadth $B_{obs}(s)$ was obtained by fitting the azimuthal distribution with the Gaussian function for each s and calculated using Equation (4).

$$B_{obs}(s) = \frac{1}{I(s,\frac{\pi}{2})} \int I(s,\varphi)d\varphi \tag{4}$$

where φ is the azimuthal angle, $I(s,\frac{\pi}{2})$ is the peak height in the azimuthal scan at π/2 for a particular s, and $\int I(s,\varphi)d\varphi$ is the area of the peak in the azimuthal scan.

$$s^2 B_{obs}^2(\mathrm{s}) = 1/L_c^2 + s^2 B_{eq}^2 \quad (5)$$

where L_c is the average void length and B_{eq} is the average void angle.

The void structure of the nonPAN_C, nonPAN_E, NaPAN_C and NaPAN_E fibers was measured using 2D-SAXS (Figure 2-8). The void angle was calculated as the square root of the slope, and the void length was calculated as the square root of the y-intercept through linear fitting of s^2 and $s^2 B_{obs}^2$ calculated by Equation (5) (Figure 2-9 (a), (c)). The void lengths and angles of nonPAN_C fiber (292.24 nm, 14.06°) and nonPAN_E fiber (295.21 nm, 14.54°) were similar (Figure 2-9 (b) and Table 2-5). These indicates no change in microstructure (crystal structures, void lengths and angles) due to electrochemical wet-spinning using PAN with no cations. This suggests that cations are the main process variable in electrochemical wet-spinning. The void length of NaPAN_E fiber (312.16 nm) was smaller than that of NaPAN_C fiber (378.80 nm), while the void angle of NaPAN_E fiber (19.86°) was larger than that of NaPAN_C fiber (16.99°) (Figure 2-9 (d)). Electrochemical wet-spinning induces demethylation by increasing the concentration of cations. Carboxylate groups and cations absorb non-solvent and exhibit plasticizing effects. Moreover, void elongation is mitigated due to absorbed non-solvent, resulting in a decrease in void length and an increase in void angle [73].

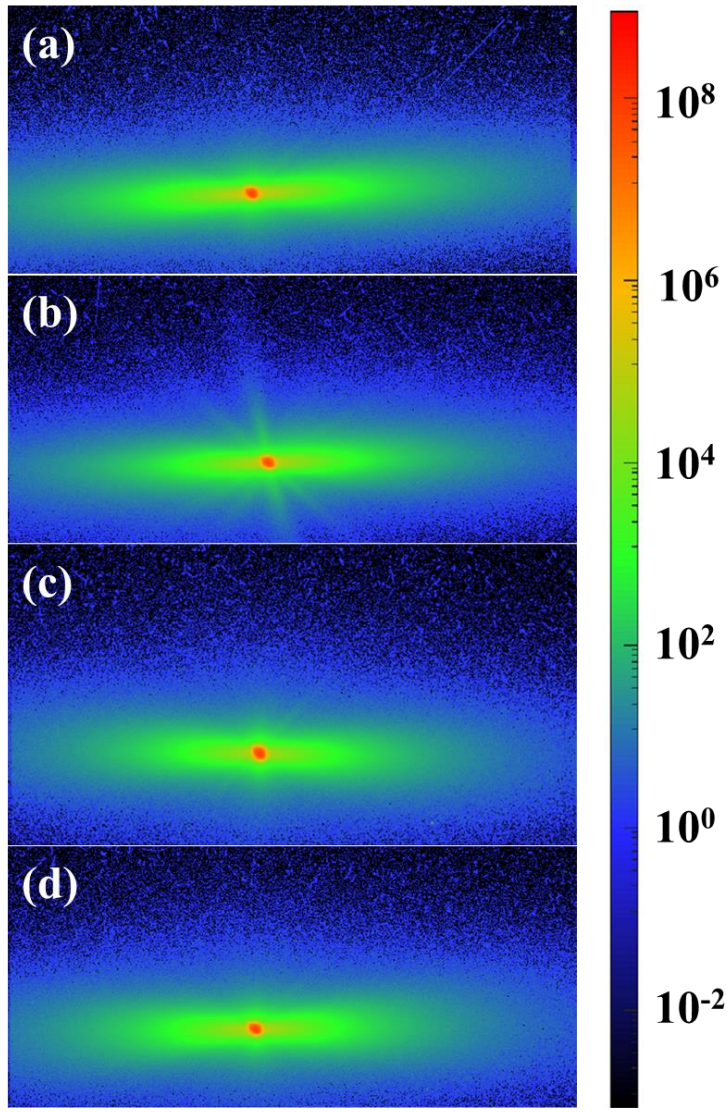

Figure 2-8. Two-dimensional small-angle X-ray scattering (2D-SAXS) images of (a) nonPAN_C, (b) nonPAN_E, (c) NaPAN_C and (d) NaPAN_E fibers.

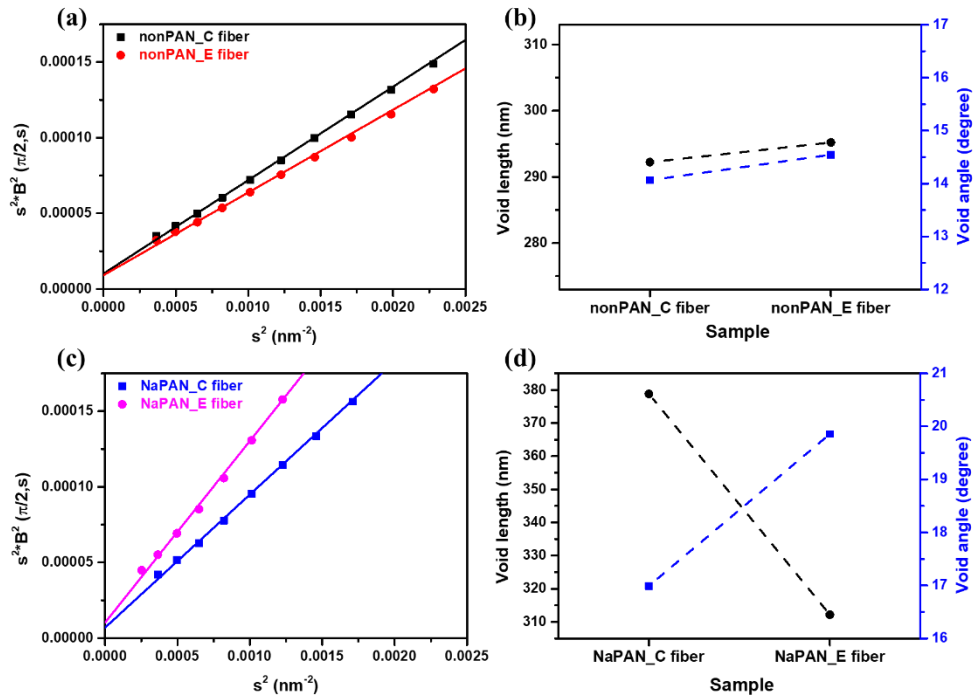

Figure 2-9. Void structure characterizations of the fibers. (a) Ruland's linear fittings and (b) void length and orientation of nonPAN_C and nonPAN_E fibers. (c) Ruland's linear fittings and (d) void length and orientation of NaPAN_C and NaPAN_E fibers.

Table 2-5. Void length and angle of nonPAN and NaPAN fibers.

Sample	Void length (nm)		Void angel (degree)	
	Conventional	Electrochemical	Conventional	Electrochemical
nonPAN	292.24	295.21	14.06	14.54
NaPAN	378.80	312.16	16.99	19.86

2.2.4. Mechanical properties

The single-filament mechanical properties were measured to compare the cation effect between conventional and electrochemical wet-spinning processes. Figure 2-10 shows the mechanical properties of nonPAN_C, nonPAN_E, NaPAN_C, and NaPAN_E fibers. The mechanical properties of nonPAN_C and nonPAN_E fibers are similar. The mechanical properties of NaPAN_C fibers are relatively greater than those of nonPAN_C fibers because NaPAN has fewer polymer chain branches than nonPAN. This is due to the difference in polymerization method. The redox polymerization method in which NaPAN is polymerized prevents the polymer chain branchs through ketone formation during polymerization [81]. The breakage strength of NaPAN_E fiber increased by 12.51% compared to NaPAN_C fiber (Figure 2-10 (d)). The improved mechanical properties due to electrochemical wet-spinning are attributed to the small voids resulting from the plasticizing effect due to an increase in non-solvent diffusion rate with increasing Na^+ concentration.

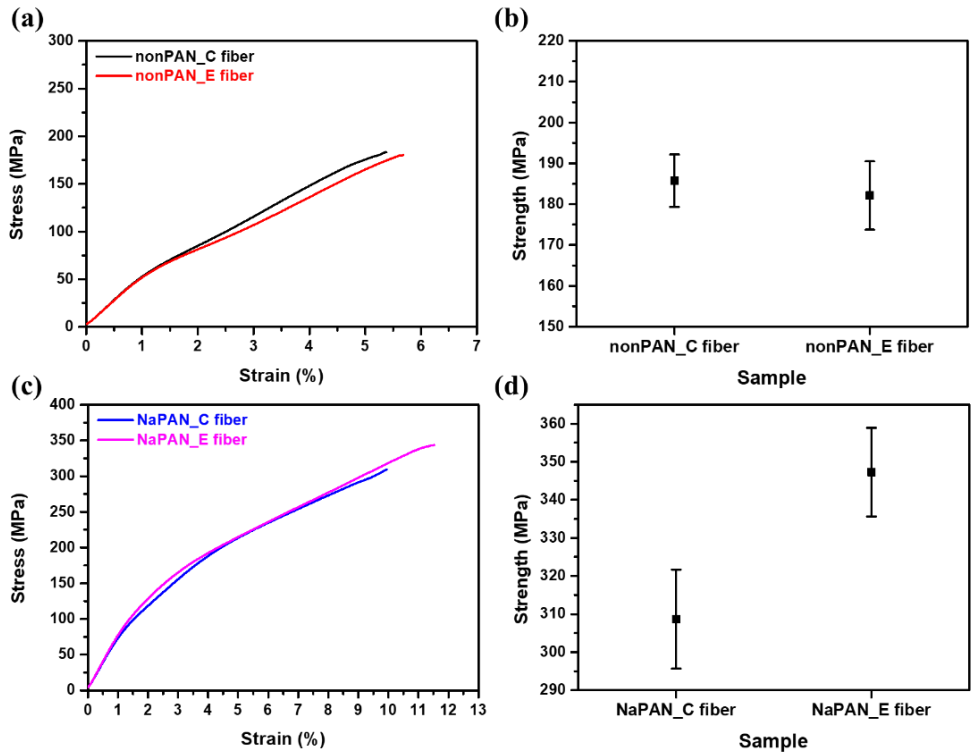

Figure 2-10. Mechanical properties of the (a) stress−strain curves of fittings and (b) strength comparison of nonPAN_C and nonPAN_E fibers. (c) Stress-strain curves of fittings and (d) strength comparison of NaPAN_C and NaPAN_E fibers.

2.3. Summary

The effects of cations within PAN and electrochemical wet-spinning on the mechanical properties of PAN fibers were examined. Applying an electrical potential to the cations within PAN dope solution resulted in an elevated concentration of cations within PAN, causing changes in the comonomer structure. Consequently, the diffusion rate of the non-solvent is accelerated during the coagulation process. Void length, a critical factor in determining mechanical properties, was reduced fibers with cations fabricated by electrochemical wet-spinning compared to conventional wet-spinning and this was calculated through 2D-SAXS. The influence of cations on other microstructural elements, including crystallinity, crystal size, and preferred orientation, showed minimal variations. The electrochemical wet-spinning process resulted in a substantial and simultaneous improvement in the mechanical properties of cations within PAN fibers.

Chapter 3. External salts in PAN dope and electrochemical wet-spinning

Previous studies on PAN fibers with salts have been conducted using post-spinning chemical treatments. Post spinning chemical treatment with an aqueous solution of alkali metal [101], succinic acid [102], zinc chloride [103] and ammonium iron(II) [104] has the advantage of lowering the stabilization temperature. Since the stabilization process is the most time-consuming and energy-intensive process in the carbon fiber manufacturing process, reducing the stabilization temperature is crucial in saving energy [14, 105]. However, despite the benefits of reducing the stabilization temperature, the non-uniform diffusion of chemicals into the PAN fibers and the utilization of additional post-processing resources offset these advantages. Moreover, as the chemicals slowly diffuse into the fibers after solidification, the distribution of the chemicals in the fibers becomes non-uniform, which slightly decreases the mechanical properties of the resulting carbon fibers [104].

In this chapter, to enhance the responsiveness of PAN to electric potential during the electrochemical wet-spinning process, salts were introduced into the dope solution. This modification led to improved mechanical properties of PAN fibers. The PAN dope solution containing Li^+ can interact with both solvent and non-solvent through solvation structure [106, 107], reducing the diffusion rate of solvent in the coagulation bath. Because of this, reducing the rate of surface solidification of the fibers. This leads to reduced void length and angle in the fibers and increased

homogeneity [35, 79, 93].

3.1. Preparation of PAN dope with external salt

3.1.1. Polymerization of PAN without cation

The organic solvents used in wet spinning have limited ability to dissolve salts, but lithium salts have solubility in both organic solvents and water [108, 109]. However, Lithium salts cannot be used as initiators for suspension polymerization. The cations without PAN (nonPAN) was synthesized following the identical procedure outlined in Chapter 2. The monomer materials used were acrylonitrile (AN, 99%, Dajung Chemical), and methyl acrylate (MA, Sigma-Aldrich) was used as a comonomer. The copolymer ratio in PAN was targeted at 6wt%, and dimethylsulfoxide (DMSO, 99.5%, Dajung Chemical) was used as the solvent. A,a'-azobis-isobutyronitile (AIBN, 99%, Dajung Chemical) was recrystallized and used as the initiator. To recrystallize AIBN, an excess of AIBN was dissolved in ethanol at 40°C and left at -5°C for 1 day, after which the precipitated AIBN crystals were filtered. In both polymerization methods, the resulting nonPAN was washed several times with distilled water and methanol and then dried in a vacuum environment at 80°C after washing with water and methanol.

3.1.2. PAN dope with external salts

PAN was dissolved in N,N-Dimethylformamide (DMF; purity : 99.8%; high performance liquid chromatography (HPLC) grade, Daejung Chemical) to prepare a dope solution. The nonPAN was dissolved at concentrations of 16wt%. To prepare the LiPAN0.5, LiPAN1.0, LiPAN3.0, and LiPAN5.0 solutions, we dissolved Lithium acetate anhydrous (Li acetate, 98.0%, Daejung Chemical) in a 16 wt% nonPAN solution. Lithium acetate is soluble in both solvent (DMF) and non-solvent (water). The numbers refer to the concentration of Li acetate. The Li acetate was added to DMF and allowed to dissolve for 1 day before adding nonPAN to prepare the solution.

3.2. Electrochemical wet-spinning of PAN fibers

3.2.1. Process condition and characterization method

The experimental setup for lab-scale wet-spinning and electrochemical wet-spinning followed the procedures outlined in Chapter 2. Dope solutions were extruded into a coagulation bath comprising a mixture of DMF and distilled water (7:3 ratio) at a flow rate of 23.6 mL/h and room temperature. A jet stretch ratio of 0.94 was applied. The resulting coagulated PAN fibers underwent a series of washing and stretching steps in three separate baths. The first bath contained a 5:5 DMF-water mixture with a stretch ratio of 1.91, followed by a second bath with water at 70 °C and a stretch ratio of 2.11. Lastly, the fibers were washed in distilled water at 90 °C with a stretch ratio of 2.16. After removing residual DMF and water at 70 °C during the drying phase, the PAN fibers were wound with a total stretch ratio of 8.18. Electrochemical wet-spinning was conducted by applying a 100 V using an electrometer (6517B, Keithley).

Morphologies of the PAN fibers were observed using field-emission scanning electron microscopes (FE-SEM, SUPRA 55VP from Carl Zeiss and SU8010 from Hitachi Co.). Chemical bonds in the PAN fibers were assessed by fourier-transform infrared spectroscopy (FT-IR, Nicolet 6700, Thermo Fisher Scientific). The cyclization temperature of the fibers analysis by differential scanning calorimetry (DSC, 200 F3 Maia, NETZSCH) and thermos gravimetric analyzer (TGA, Discovery TGA, TA instruments). Temperature was increased to 400 °C heated at

10 °C/min under N_2. The microstructures of fibers were characterized by 2D wide-angle X-ray diffraction (2D-WAXD, D8 Discover; Bruker) and 2D small-angle X-ray scattering (2D-SAXS, Xeuss 2.0, Xenocs). The radiation wavelength of 2D-WAXD and 2D-SAXS was 0.154 nm (Cu Kα). The mechanical properties of PAN fibers were measured using a single-fiber tester (FAVIMAT, Textechno, Mönchengladbach) with a 20 mm gage length and a crosshead speed of 20 mm/min. The tensile strength was analyzed using fiber diameters measured from FE-SEM images.

3.2.2 The effect of salts on electrochemical wet-spinning

Fibers fabricated of nonPAN were denoted nonPAN_C fiber and nonPAN_E fiber based on the fabrication method, where nonPAN_C fiber was fabricated by conventional wet-spinning, and nonPAN_E fiber was fabricated by electrochemical wet-spinning. Likewise, Fibers fabricated of LiPAN were denoted LiPAN_C fiber and LiPAN_E fiber. (Figure 2-4 (a)-(d) and Figure 3-1). The average diameters of the nonPAN_G, nonPAN_E, LiPAN_C and LiPAN_E fibers were measured as 11.87 ± 0.69, 11.95 ± 0.84, 11.75 ± 0.66, and 12.15 ± 1.03 μm, respectivel y. The cross-section of the LiPAN_C and LiPAN_E fibers is circular with some wrinkles. These wrinkles appear due to the difference in diffusion rates of the solvent and non-solvent during the coagulation process [92].

Li^+ not only accelerates the diffusion rate of the non-solvent but also reduces the diffusion rate of the solvent. Comparison of the FT-IR spectra of LiPAN_C and LiPAN_E fibers revealed a solvation sturctue in LiPAN_E fibers (figure 3-2). Lithium ions bind with solvent molecules to form a solvation structure, which hinders diffusion from the dope solution to the coagulation bath [110]. As a result, this slows down the solidification of the surface, promoting uniform solidification of the fibers and reducing wrinkles, leading to increased homogeneity of the fiber's sheath and core [35, 93].

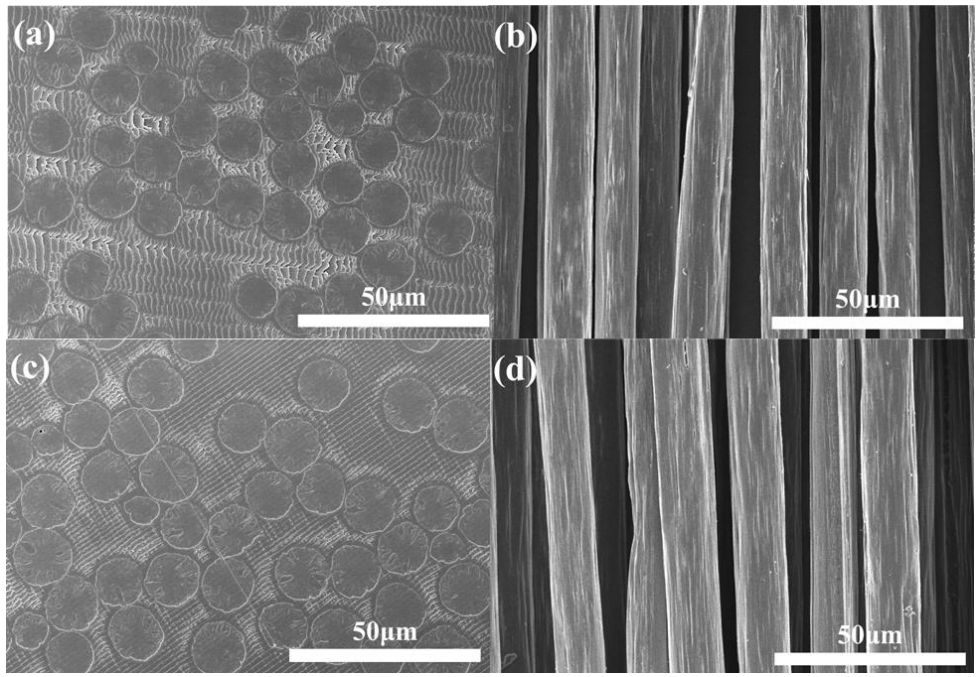

Figure 3-1. Scanning electron microscopy (SEM) images of the cross section and surface morphology (a,b) LiPAN_C and (c,d) LiPAN_E fibers.

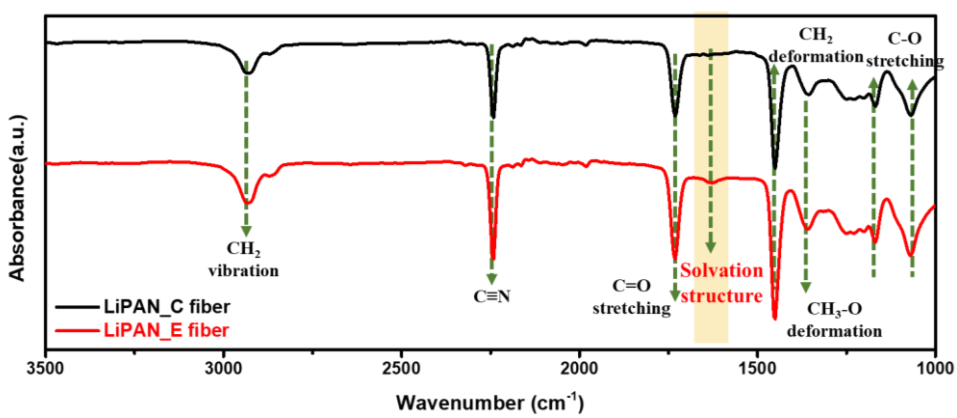

Figure 3-2. Fourier transform infrared (FT-IR) spectra of LiPAN fibers.

LiPAN_C and LiPAN_E fibers were compared using FT-IR spectroscopy, which revealed a C=O stretching peak in the LiPAN_E fibers. This peak indicates the presence of a solvation structure between DMF and Li^{+}. Through this observation, it can be confirmed that there is an interaction between Li^{+} and DMF. The FT-IR data in Figure 3-3 represents nascent fibers collected from a point in the LiPAN coagulation bath that is located 5 cm, 20 cm and 35 cm away from the nozzle. The samples are denoted as C_5cm, C_20cm, C_35cm, E_5cm, E_20cm, and E_35cm, where C and E represent the conventional and electrochemical wet-spinning fabrication methods, respectively. The numbers indicate the coagulation bath length. The intensity of the DMF peak in C_5cm, normalized to the PAN peak intensity, is 9.49, while the water peak intensity is 1.00. In E_5cm, the DMF peak intensity is 10.46, and the water peak intensity is 1.39 (Figure 3-3 (a), (c)). From these results, it can be concluded that the diffusion rate of the non-solvent (water) increases, and the diffusion rate of the solvent (DMF) decreases due to the electrical potential in the electrochemical wet-spinning process. The intensity of the DMF peak in C_20cm is 9.34 and the water peak is 1.04. Also, the intensity of the DMF peak in C_35cm is 9.33 and the water peak is 1.25 (Figure 3-3 (a), (c)). FT-IR peaks of LiPAN_E nascent fibers were also quantified. The intensity of the DMF peak in E_20cm is 10.09 and the water peak is 1.39. Also, the intensity of the DMF peak in C_35cm is 9.33 and the water peak is 1.40 (Figure 3-3 (b), (c)). As the coagulation bath length increased in both conventional and electrochemical wet-spinning processes, the amount of water increased while the amount of DMF decreased. Moreover, nascent fibers produced through electrochemical wet-

spinning contained higher levels of DMF and water compared to those produced through conventional wet-spinning. However, at the maximum coagulation length, both types of fibers contained similar amounts of DMF, indicating a slower coagulation process for the electrochemical wet-spun fibers, which fully coagulated at 35 cm. Additionally, the electrochemical wet-spun fibers contained a higher water content compared to the conventional wet-spun fibers. This phenomenon can be attributed to the addition of salt to the PAN solution during electrochemical wet-spinning, which reduces the diffusion rate of DMF and enhances the diffusion rate of water.

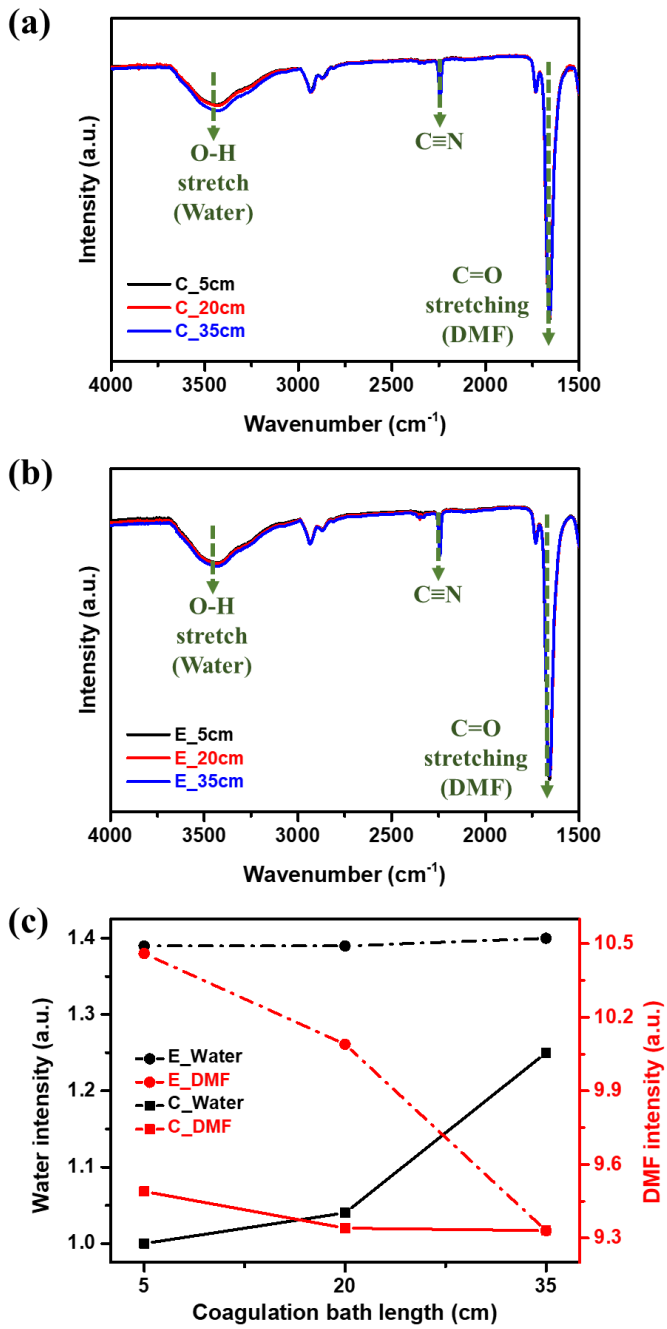

Figure 3-3. Fourier transform infrared (FT-IR) spectra of (a) LiPAN_C and (b) LiPAN_E nascent fibers with different coagulation bath lengths. (c) The normalization intensity of water and DMF in LiPAN_C and LiPAN_E nascent fibers.

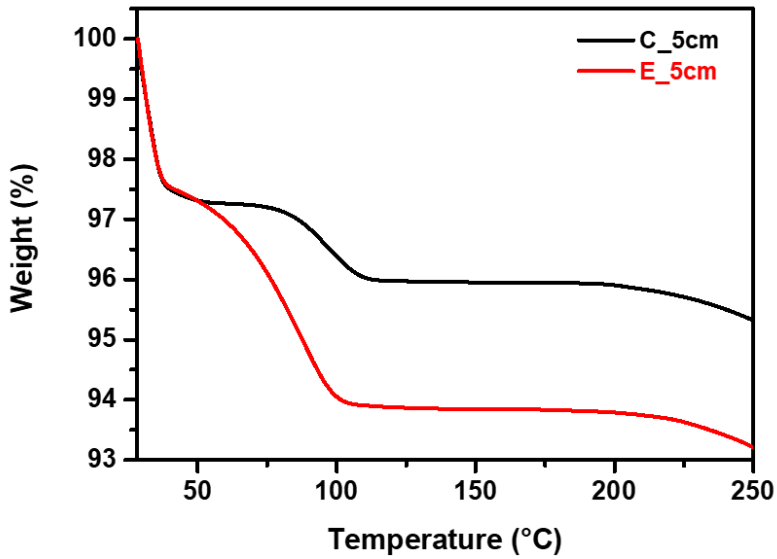

Figure 3-4. Thermogravimetric analyzers (TGA) of LiPAN nascent fibers.

Figure 3-4 represents the TGA data of nascent fibers dried in ambient conditions for 1 day. When the nascent fibers were directly subjected to TGA measurements, water easily evaporated, resulting in inaccurate measurements. To overcome this issue, the water was evaporated over the course of 1 day by utilizing the difference in vapor pressure between water and DMF. After an initial preheating step below 50°C, the remaining water evaporated, followed by a decrease in weight due to the evaporation of DMF. C_5cm exhibited a decrease of 1.41%, while E_5cm showed a decrease of 3.52%. This can be attributed to the interaction (solvation structure) between Li^+ ions generated through the electrical potential, which subsequently decreased the diffusion rate of DMF.

The thermal properties of nonPAN and LiPAN fibers were analyzed by DSC (Figure 3-5 (a)). According to the DSC results, the onset and peak temperatures decreased

with the addition of Li acetate. This is a result of Li^+ and acetate ions being partially present in the fiber. This means that the stabilization process requires a lower temperature to start and that a little amount of energy is saved during the stabilization process [104]. Also, the peak of the LiPAN_E fiber is broader compared to that of the LiPAN_C fiber. The lower and broader peak indicates that the LiPAN_E fiber avoids centralized heat release during the stabilization process [16]. nonPAN_C, nonPAN_E, LiPAN_C, and LiPAN_E fibers were analyzed by TGA to obtain the DTA values (Figure 3-5 (b)). In the DTA graph, the peak temperature of nonPAN_C fiber is 292.3°C, while the peak temperature of nonPAN_E fiber is 292.0 °C, which is similar. The peak temperature of LiPAN_C fiber is 285.6°C, and the peak temperature of LiPAN_E is 285.0°C, which is also similar. The peak temperature of fibers with Li acetate decreased by about 7°C. The reason for this peak temperature change is that the ions act as a catalyst in the cyclization step [104].

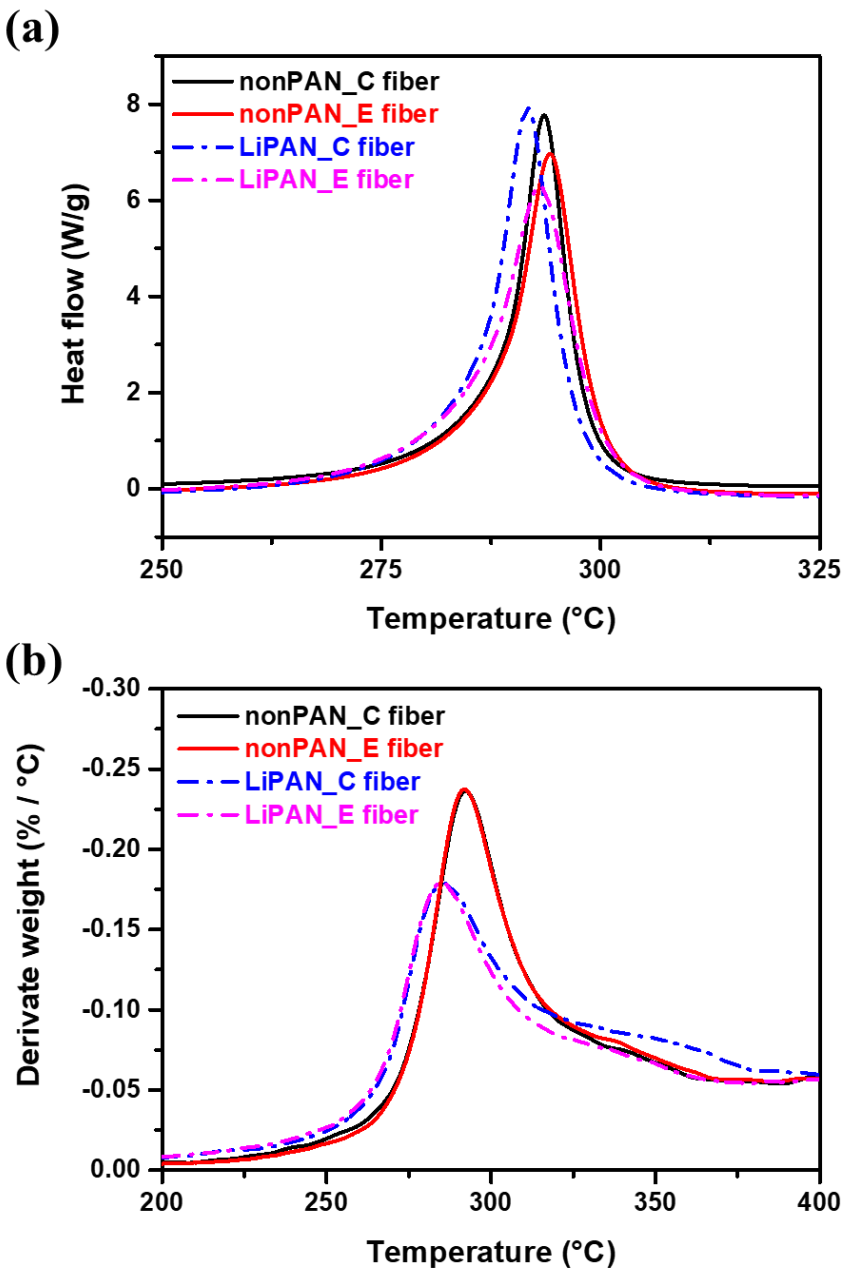

Figure 3-5. Thermal properties of nonPAN and LiPAN fibers. (a) Differential scanning calorimetry (DSC) analysis and (b) differential thermal analysis(DTA) curves.

3.2.3. Microstructural and mechanical characterization

The crystal structures of the LiPAN fibers were measured using 2D-WAXD (Figure 3-6). The crystallographic (crystallinity, crystal size and preferred orientation) of the nonPAN and LiPAN fibers were calculated using the same method as described in Chapter 2. The crystallinity of the fibers was calculated according to Hinrichsen's method [96]. Calculated crystallinity and crystal size shows in Table 3-1. The calculated crystallinity values for nonPAN_C, nonPAN_E, LiPAN_C, and LiPAN_E fibers were 57.56%, 57.28%, 56.75%, and 56.98%, respectively. nonPAN and LiPAN fibers showed similar crystallinity. The calculated crystal sizes for nonPAN_C, nonPAN_E, LiPAN_C, and LiPAN_E fibers were 3.40 nm, 3.40 nm, 3.40 nm, and 3.44 nm, respectively. Similarly, the crystal size was not significantly affected by the addition of Li acetate or the fabrication method. The preferred orientations of the fibers were calculated from peak integrations of the azimuthal scans at $2\theta = 17°$ (Figure 3-6 (d)). The preferred orientation, which ranged from 80.63% to 84.05%, did not show significant differences between nonPAN and LiPAN fibers. In summary, there were no significant differences in the crystal structure of the fibers due to the addition of Li acetate and the fabrication method.

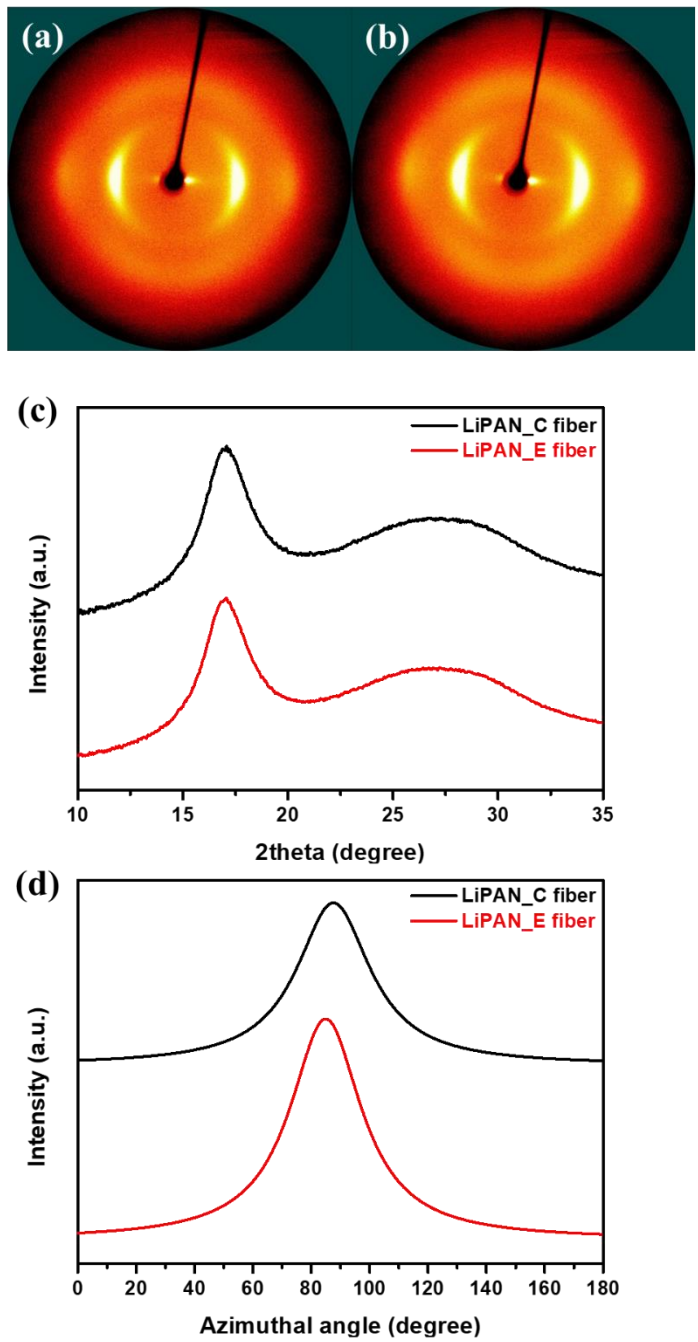

Figure 3-6. Microstructural characterization of the PAN fibers. Two-dimensional w ide-angle X-ray diffraction (2D-WAXD) images of (a) LiPAN_C and (b) LiPAN_E fibers. (c)Equatorially extracted one-dimensional WAXD curves and (d) azimuthal scans at 2θ = 17° of LiPAN_C and LiPAN_E fibers.

Table 3-1. Crystallinity and crystal size of nonPAN and LiPAN fibers.

Sample	Crystallinity (%)		Crystal size (nm)	
	Conventional	Electrochemical	Conventional	Electrochemical
nonPAN	57.56	57.28	3.40	3.40
LiPAN	56.57	56.98	3.40	3.44

The void structure of the LiPAN fibers was measured using 2D-SAXS (Figure 3-7). The void angle was calculated as the square root of the slope, and the void length was calculated as the square root of the y-intercept through linear fitting of s^2 and $s^2 B_{obs}^2$ calculated by Ruland's streak method described in Chapter 2 (Figure 3-8 (a)). The void length of LiPAN_C fiber (287.12 nm) was smaller than that of nonPAN_C fiber (292.24 nm). The void angle of nonPAN_C fiber (14.06°) was similar that of LiPAN_C fiber (14.07°) (Figure 3-8 (b) and Table 3-2). The addition of lithium salt to the dope solution in conventional wet spinning resulted in a decrease in void length within PAN fibers. The void length of LiPAN_E fiber (274.05 nm) was smaller than that of LiPAN_C fiber (287.12 nm). The void angle of LiPAN_E fiber (12.91°) was smaller than that of LiPAN_C fiber (14.07°) (Figure 3-8 (c)). During electrochemical wet spinning, the concentration of cations in the dope solution increases. Depending on the type of cation included in PAN dope solution, the Na^+ concentration increases in NaPAN, and the Li^+ concentration increases in LiPAN. Since Lithium salts, being soluble in organic solvents, can interact with the solvent, leading to a reduction in solvent diffusion rate during the coagulation

process [106]. Consequently, the skin of the fiber is formed relatively slowly. This increased the orientation of the fibers during coagulation, resulting in a relatively reduced initial void angle [111]. Therefore, the void angle of the final fiber also decreases.

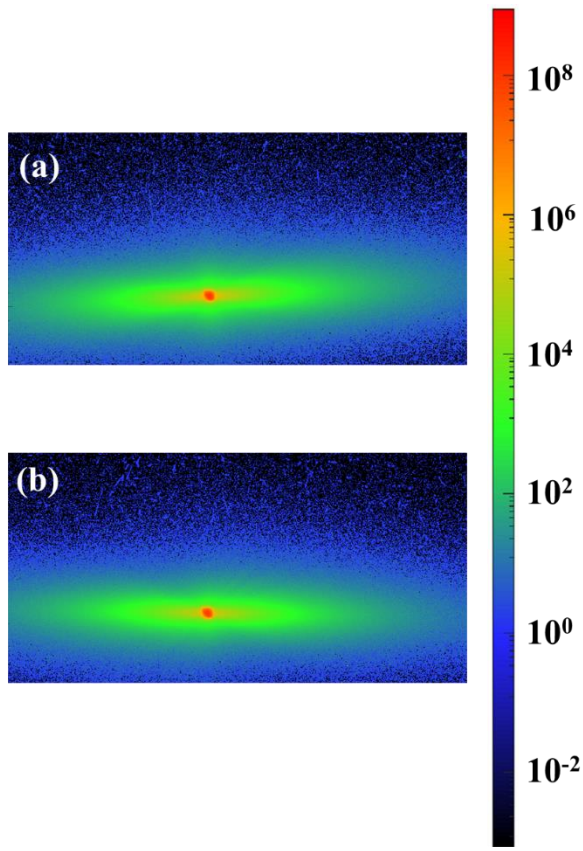

Figure 3-7. Two-dimensional small-angle X-ray scattering (2D-SAXS) images of (a) LiPAN_C and (b) LiPAN_E fibers.

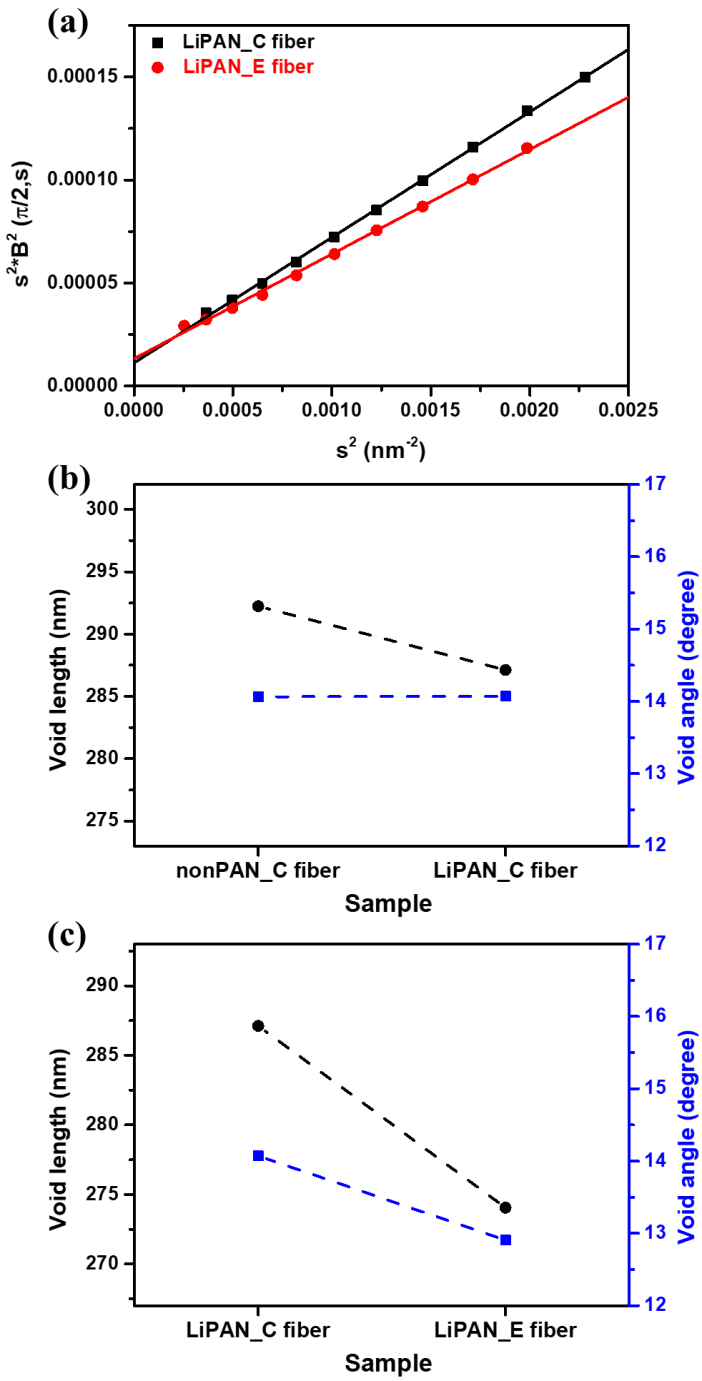

Figure 3-8. Void structure characterizations of the fibers. (a) Ruland's linear fittings of LiPAN_C and LiPAN_E fibers. Void length and orientation of (b) nonPAN_C and LiPAN_C fibers and (c) LiPAN_C and LiPAN_E fibers.

Table 3-2. Void length and angle of nonPAN and LiPAN fibers.

Sample	Void length (nm)		Void angel (degree)	
	Conventional	Electrochemical	Conventional	Electrochemical
nonPAN	292.24	295.21	14.06	14.54
LiPAN	287.12	274.05	14.07	12.91

The single-filament mechanical properties were measured to assess the effect of Li^+ in the conventional and electrochemical wet-spinning processes. LiPAN_C showed higher showed higher strength, strain, and modulus compared to nonPAN_C (Figure 3-9 (a), (b)). The breakage strength of LiPAN_E fiber increased by 27.45% compared to LiPAN_C fiber (Figure 3-9 (b)). The improved mechanical properties observed in nonPAN_C are attributed to small voids resulting due to an increase in non-solvent diffusion rate. LiPAN_E showed higher showed higher strength, strain, and modulus compared to LiPAN_C (Figure 3-9 (c), (d)). The breakage strength of LiPAN_E fiber increased by 16.12% compared to LiPAN_C fiber (Figure 3-9 (d)). The improved mechanical properties observed in LiPAN_E are attributed to small and oriented voids resulting from the plasticizing effect due to an increase in non-solvent diffusion rate, and longer skin formation time due to a decrease in solvent diffusion rate with increasing Li^+ concentration.

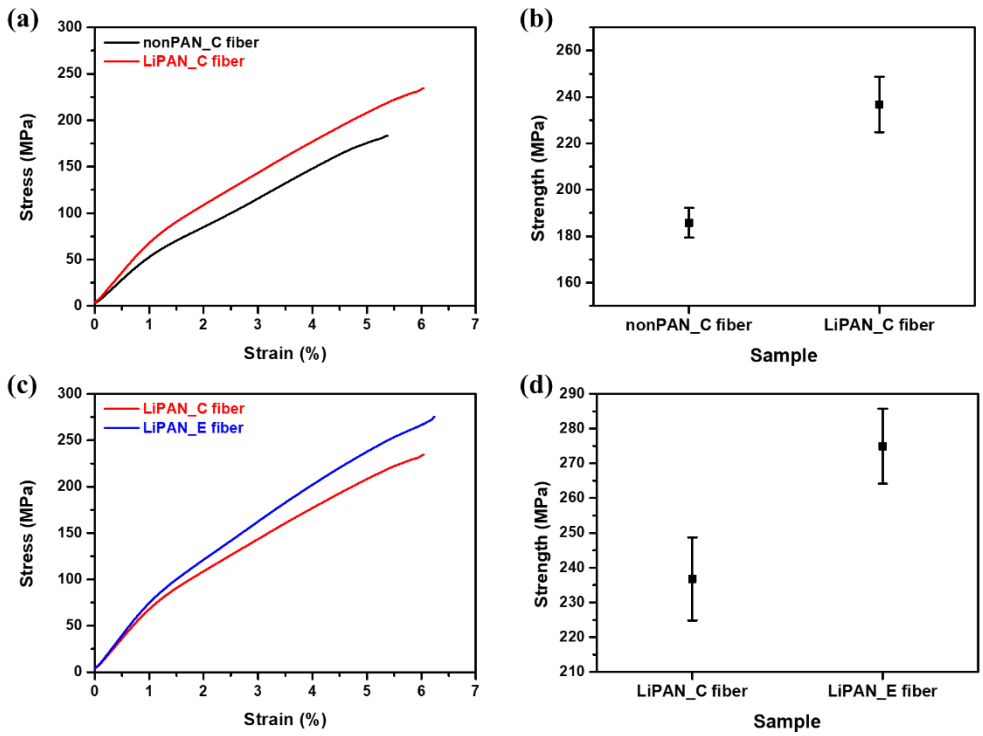

Figure 3-9. Mechanical properties of the nonPAN_C, LiPAN_C and LiPAN_E fibers. (a) Stress−strain curves and (b) strength comparison of nonPAN_C and LiPAN_C fibers. (c) Stress−strain curves and (d) strength comparison of LiPAN_C and LiPAN_E fibers.

3.2.4. Optimization of external salt concentration

In order to investigate the effect of cation concentration, a series of dope solutions were prepared with varying amounts of Li acetate. Note that the LiPAN is the same as LiPAN1.0. Single-filament mechanical properties were measured to determine the effect of cation concentration on both conventional and electrochemical wet-spinning processes. Figure 3-10 displays surface scanning electron microscopy (SEM) images of PAN fibers at varying concentrations of lithium salt. The average diameters of the LiPAN0.5_C, LiPAN0.5_E, LiPAN3.0_C, LiPAN3.0_E, LiPAN5.0_C and LiPAN5.0_E fibers were measured as 12.27 ± 0.79, 11.63 ± 0.65, 11.88 ± 0.43, 12.56 ± 0.62, 12.64 ± 0.85 and 11.38 ± 0.61 μm, respect ively. The mechanical properties of fibers containing Li acetate were found to be increased (Figure 3-11). LiPAN1.0_C and LiPAN1.0_E fibers have the greatest mechanical properties. In electrochemical wet-spinning, the dissociation degree of Li acetate increases due to electric potential, and the Li^+ concentration in the nozzle increases, thereby maximizing the effect of increasing mechanical properties [112]. Since Li acetate does not have a high degree of dissociation in organic solvents, it acts as an impurity when coagulation occurs. Therefore, if the content of Li acetate is excessive, it can damage the fiber and deteriorate its mechanical properties. This can be observed in morphology (Figure 3-10 (c)-(f)). LiPAN3.0_C, LiPAN3.0_E, LiPAN5.0_C, and LiPAN5.0_E fibers were found to be non-uniform and have large damage in the surface. A small amount of Li acetate increased the mechanical properties of the fiber, but an excessive amount of Li acetate decreased the

mechanical properties. In summary, fibers fabricated using dope solution containing cation and electrochemical wet-spinning can improve mechanical properties, and the optimal cation concentration reduces the diffusion rate of the solvent and increases the diffusion rate of the non-solvent to improve mechanical property.

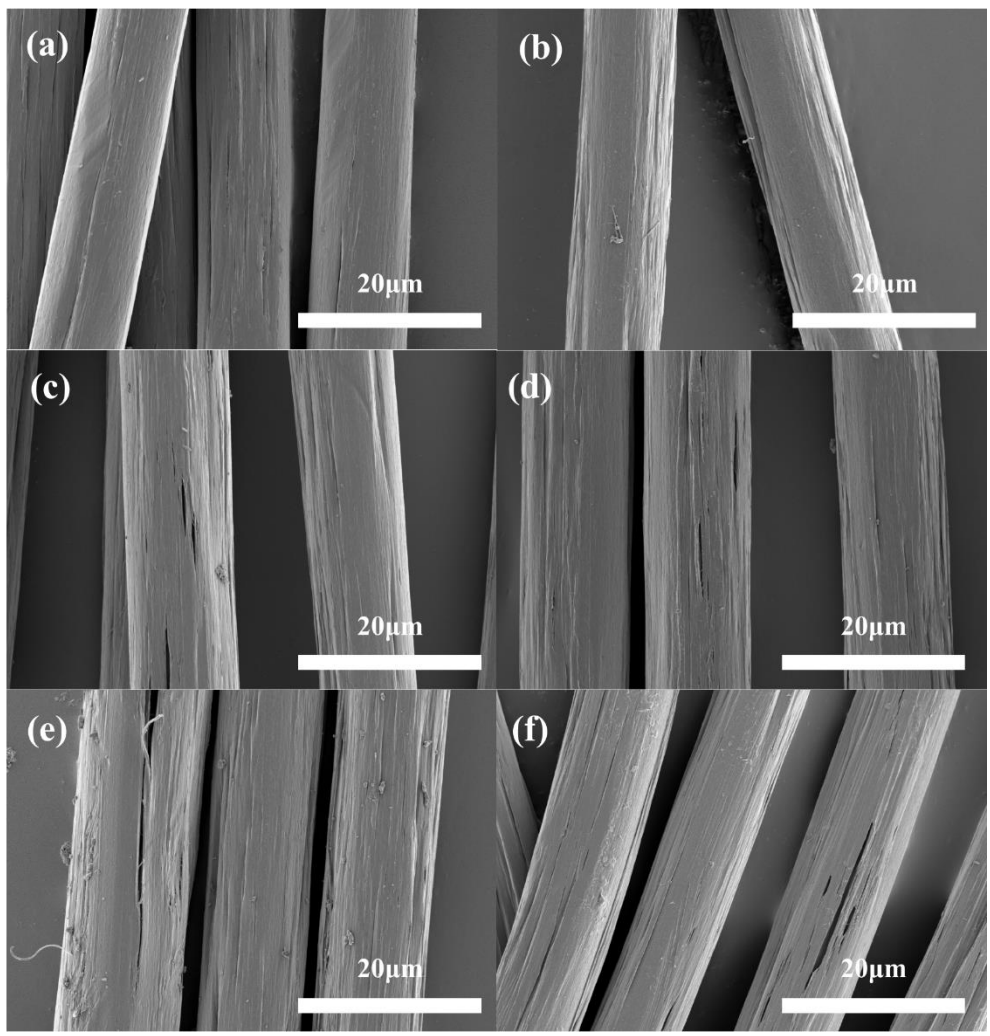

Figure 3-10. Scanning electron microscopy (SEM) images of the surface morphology (a) LiPAN0.5_C, (b) LiPAN0.5, (c) LiPAN3.0_C, (b) LiPAN3.0_E, (c) LiPAN5.0_C and (d) LiPAN5.0_E.

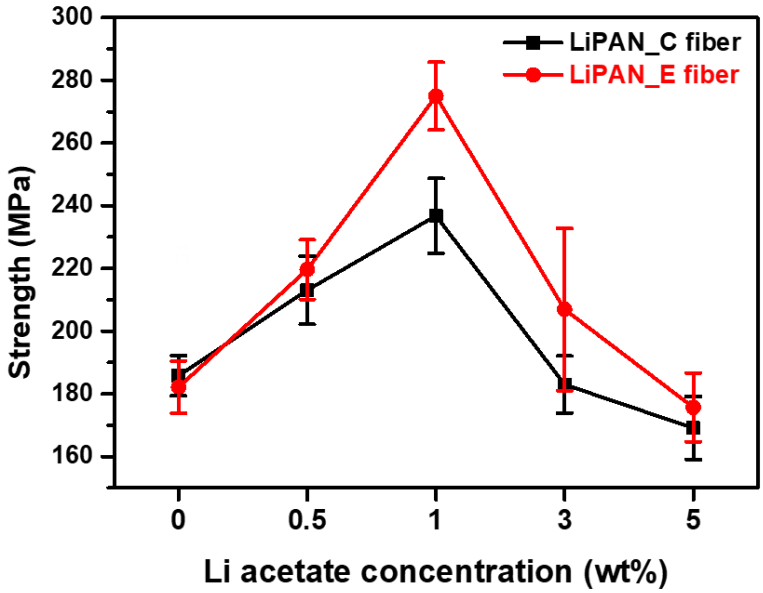

Figure 3-11. Mechanical properties of LiPAN_C and LiPAN_E fibers as a function of Li acetate concentration.

3.3. A mechanism for electrochemical wet-spinning

Figure 3-12 (a) illustrated the molecular structure change of PAN due to cations when ionized salts are included in dope solution. The cation stabilizes the carboxyl group inside MA, and the methyl group (-CH_3) is separated [101, 113]. When the methyl group is separated, a carboxyl group (-COO-) remains. This causes a cyclization reaction with an adjacent nitrile group (-CN) [104]. Figure 3-12 (b) shows the solidification process that occurs as the cation concentration increases due to the voltage applied to the dope solution. When the concentration of cations in the dope solution is increased by electrical potential, the hydrophilic property of PAN increases and the diffusion rate of the non-solvent increases during the coagulation process, thereby increasing the coagulation rate. Absorbed non-solvent increases chain mobility and creates smaller voids [73].

The PAN dope solution containing Li acetate, which dissolves well in both solvent (DMF) and non-solvent (DI water), increases the concentration of cation in the nozzle by applying voltage. Li^+ can interact with both solvent and non-solvent[106, 107]. This reduces the rate of diffusion of the solvent in the coagulation bath. Not only does the absorption of non-solvents become faster, but the diffusion rate of the solvent is also slowed down. This reduces the rate of surface solidification of the fibers, which reduces the void length and angle in the fibers [79]. In addition, t The reduced solvent diffusion rate prevents rapid solidification of the surface, allowing the non-solvent to diffuse uniformly into the fiber. Therefore, the homogeneity of the skin and core of the fiber increases [35, 93]. So, the addition of a Lithium salt in an

organic solvent is expected to maximize the electrochemical effect and improve mechanical properties. In addition, the improvement of the stabilization process is expected due to the catalytic role of ions in the stabilization reaction reported in previous studies [104].

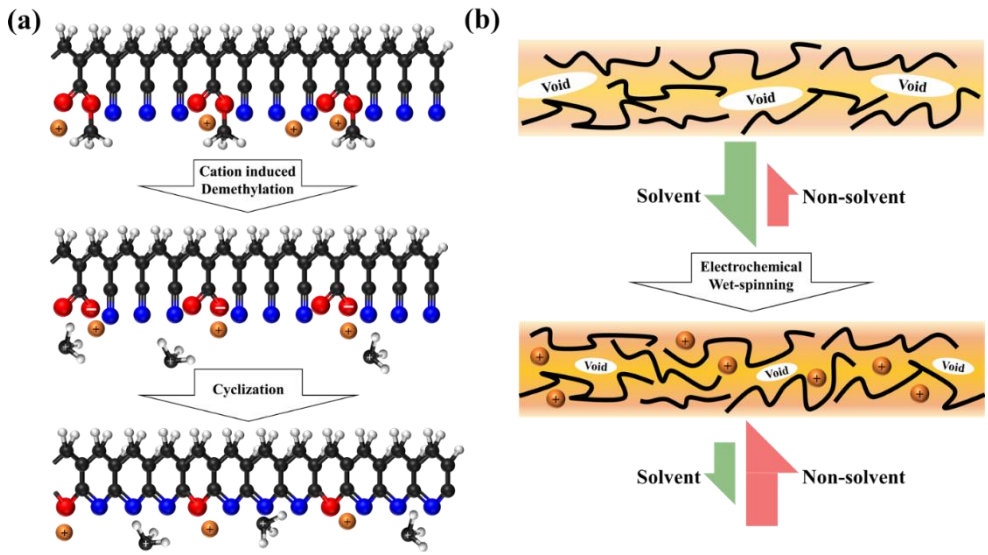

Figure 3-12. Schematic illustration of cation-enhanced wet spinning (electrochemical wet-spinning with cation) in (a) conductive nozzle (b) coagulation process.

3.4. Summary

The effect of cations on conventional wet-spinning and electrochemical wet-spinning was investigated by comparing cations without PAN(nonPAN) with salt (LiPAN). The salt in the PAN fibers caused a decrease in the cyclization temperature of the fibers. The void plays a crucial role in determining the mechanical properties of fibers. Both conventional and electrochemical wet-spinning processes, when incorporating cations, led to a decrease in void length. Notably, electrochemical wet-spinning resulted in a more significant reduction in void length compared to conventional wet-spinning, as assessed using 2D-SAXS analysis. Void angle decreased only LiPAN_E fibers. This is because Li^+ interacts with both the solvent and the non-solvent, it reduces the diffusion rate of the solvent and increases that of the non-solvent, thereby increasing the homogeneity and orientation of the fiber. However, an excessive amount of salt damaged the fibers and reduced the mechanical properties of the fibers. Therefore, the mechanical properties of PAN fibers with cation can be improved by electrochemical wet spinning. Optimal cation concentration can modulate the diffusion rate of solvent and non-solvent to minimizing voids and increase mechanical properties.

Chapter 4. The effect of moisture on wet-spinning behavior

Water plays a critical role as a non-solvent in the wet-spinning process of PAN fibers, especially during the coagulation stage. The diffusion of water during phase separation in the coagulation bath is a key factor influencing the properties of PAN fibers. Consequently, research has been conducted to investigate the water ratio and temperature in the coagulation bath [50, 67]. Additionally, researchers have explored incorporating water into the dope solution. The addition of water to the dope solution affects the diffusion rate of the solvent and non-solvent in the coagulation bath, leading to changes in the microstructure and properties of PAN fiber [114-117]. However, an excessive amount of water in the dope solution can result in increased inhomogeneity due to coagulation among PAN molecules, causing gel formation [118-120]. Therefore, determining the optimal water content is crucial for achieving the best mechanical properties by minimizing void structures.

In this chapter, to achieve a more uniform binding between PAN polymer chains and water molecules, a different approach was employed compared to previous studies. Instead of using liquid water, vaporized water molecules (moisture) were utilized. This method aimed to facilitate a more even and consistent interaction between PAN polymer chains and water molecules. [121]. PAN copolymer containing 6 wt% methyl acrylate (PAN-MA), used precursor copolymer for the carbon fiber manufacture, was used to investigate the effect of adsorbed water on the

mechanical properties of PAN fibers. the adequate amount of adsorbed water molecules is expected to reduce the electrostatic repulsion between the electron-poor methyl and hydrocarbon backbone, but large amount of water can form their own phase resulting in the defective void when the fiber is formed. Thus, it is important to optimize the water content for optimum mechanical properties of the precursor fiber. The amount of adsorbed water was systematically controlled by dehydration and hydration, and the source polymer, dope solutions, and wet-spun fibers were thoroughly characterized to establish the effect of the adsorbed water.

4.1. Preparation of dried and moisturized PAN

4.1.1. PAN drying

The PAN-MA copolymer (M_W = 80,000 g mol^{-1}, 6 wt% MA, Polysciences) was chosen as the polymer for the wet-spun fiber. N,N-Dimethylformamide (DMF; purity: 99.8%; high-performance liquid chromatography (HPLC) grade; Daejung Chemical) was used as the solvent. Silica gel (Daejung Chemical) was used to adsorb water vapor from drying PAN to prevent reuptake.

Commercial PAN (CPAN) powder was dried in a vacuum oven at 120°C for 48 h to remove inherently adsorbed water. The PAN powder was stored in a glass jar covered with perforated aluminum foil, and silica gel was placed on the aluminum foil to adsorb evolved water vapor (Figure 4-1). Drying at high temperature (120°C) under vacuum effectively removed water, and the long drying time (48 h) was chosen based on a preliminary experiment that showed no further weight change of CPAN after 24 h. The dried PAN (DPAN) had an average weight loss of 1.57 ± 0.09%.

Figure 4-1. Photographs illustrating the drying process of PAN powder.

The morphologies of the PAN powders were examined using field-emission scanning electron microscopes (SUPRA 55VP from Carl Zeiss and SU8010 from Hitachi Co.). Chemical bonds and residual solvents in the molecular structures were assessed by Fourier-transform infrared spectroscopy (FT-IR; Nicolet 6700; Thermo Fisher Scientific). The cyclization temperature of the PAN powder analysis by thermos gravimetric analyzer (TGA, Discovery TGA, TA instruments). The microstructures of PAN powders were characterized by wide-angle X-ray diffraction (WAXD) (D8 Discover; Bruker).

During the drying process, copolymers were demoisturized without causing any microstructural changes. The demoisturization of commercial PAN was characterized using FT-IR spectroscopy, as shown in Figure 4-2 (a). The FT-IR spectra of CPAN and DPAN exhibited characteristic peaks corresponding to the monomers, including acrylonitrile (CH_2 antisymmetrical and symmetrical vibrations (2,920 and 2,840 cm^{-1}, respectively), C≡N (2,242 cm^{-1}), and CH_2 deformation (1,440 cm^{-1})) and MA (C=O stretching (1,730 cm^{-1}), O–CH_3 deformation (1,380 cm^{-1}), and C–O stretching (1,255 and 1,090 cm^{-1})) [122, 123]. Significant changes in the peaks of the CPAN FT-IR spectrum indicated the occurrence of demoisturization. The hydroxyl stretching peak at 3,550 cm^{-1} and the H–O–H bending peak at 1,630 cm^{-1} were absent from the FT-IR spectrum of PAN after completely drying [124].

Thermogravimetric analysis revealed that DPAN did not exhibit any mass loss above 200℃, whereas CPAN experienced a reduction in mass in this temperature

range, as depicted in Figure 4-3. Despite these differences, the microstructures showed minimal changes, as illustrated in Figure 4-2 (b), and the wide-angle X-ray diffraction (WAXD) curves were nearly identical. The measured crystallinities of CPAN and DPAN were 59.00% and 58.74%, respectively, with corresponding crystallite sizes of 6.74 nm and 6.67 nm. The morphologies of CPAN and DPAN did not exhibit significant distinctions, as shown in Figure 4-2 (c) and (d).

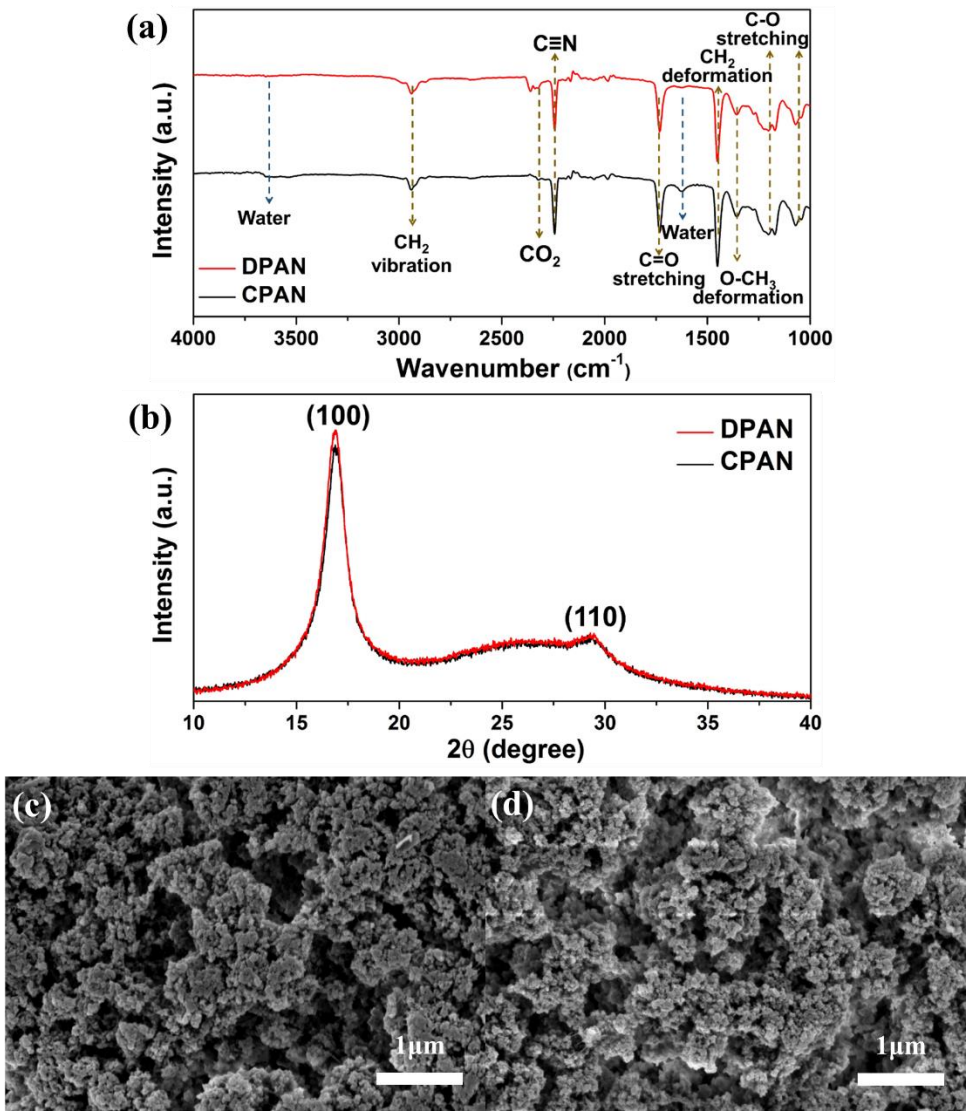

Figure 4-2. Investigations of structural and morphological changes in comme rcial PAN (CPAN)and dried PAN (DPAN) powders. (a) Fourier transform-in frared spectroscopy (FT-IR), (b) wide-angle X-ray diffraction (WAXD) patter ns, and (c, d) scanning electron microscopy (SEM) images of (c) CPAN and (d) DPAN powders.

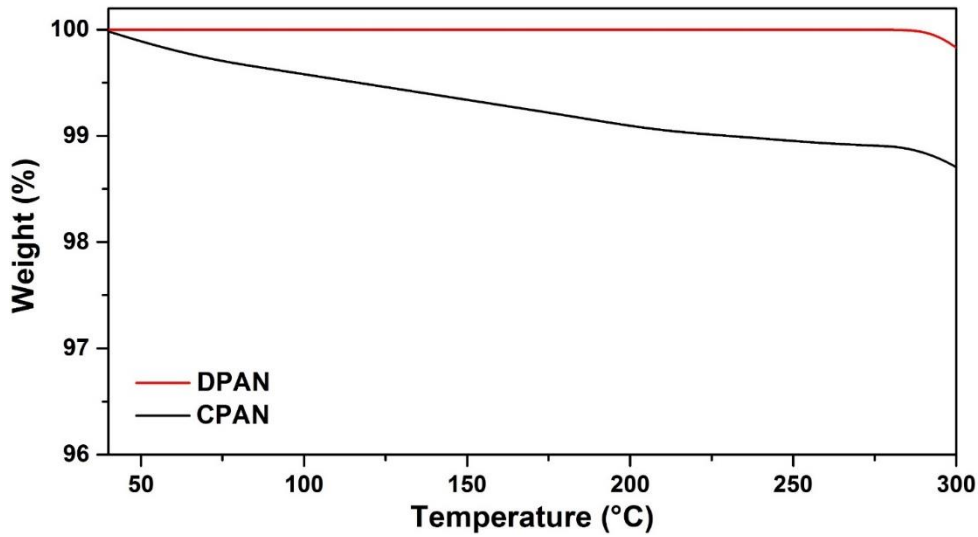

Figure 4-3. Thermogravimetric analyses (TGA) of commercial and dried PAN (CPAN and DPAN).

4.1.2. PAN moisturization

The dried PAN (DPAN) was subsequently moisturized in a lab-made humid ifying chamber (Figure 4-4). The humidity in the chamber was regulated at 90% at room temperature (25℃).

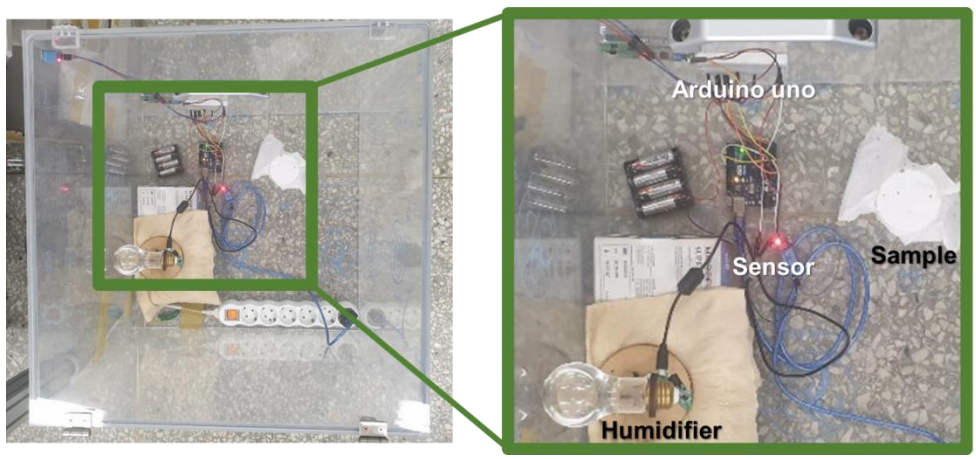

Figure 4-4. Photograph of lab-made humidifying chamber.

In the lab-made humidifying chamber, the moisturizing behavior of DPAN was monitored by measuring the weight change, as shown in Figure 4-5. Initially, the moisturization rate was high but gradually decreased over time following an exponential decay pattern. At 1.6 and 10 hours, water contents of 0.5 and 1.0 wt% were measured, respectively. The highest water content of 1.44 wt% remained unchanged even after 67 hours of moisturization. Based on these observations, water contents of 0, 0.5, 1.0, and 1.44 wt% were selected for further investigation to understand the impact of moisturization on the microstructures and mechanical

properties of PAN fibers.

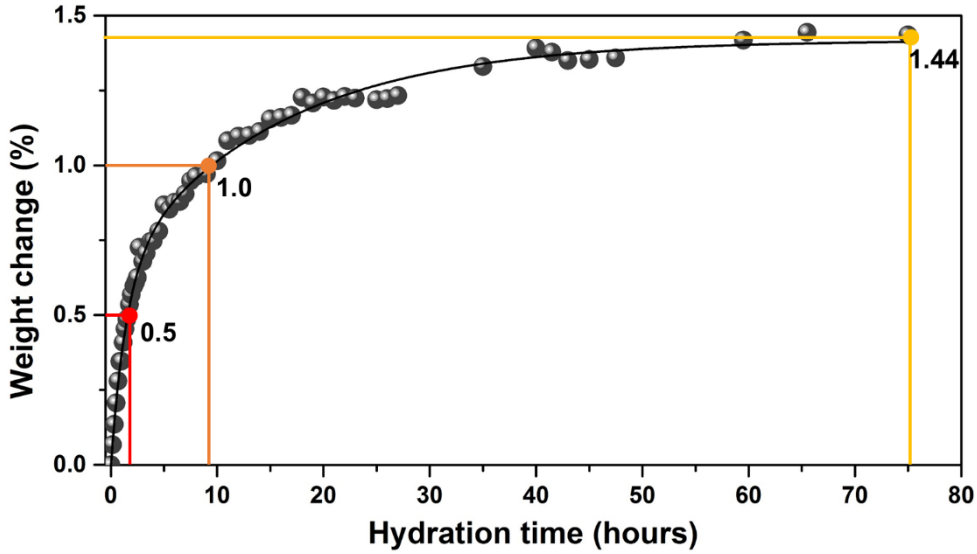

Figure 4-5. Change in the water content of DPAN as a function of time.

The rheological properties of the dope solutions were measured using a rheometer (DHR-2; TA Instruments). The dope solutions were placed between two 40-mm-diameter parallel plates separated by 1 mm. Flow sweep in the shear rate range of 0.01–500 s^{-1} and frequency sweep in the angular frequency range of 0.1–500 rad s^{-1} were used to investigate the homogeneity of the dope solutions and the PAN intermolecular interactions in the dope solution at room temperature.

The observed viscosity changes in DPAN and moisturized PAN dope solutions, as depicted in Figure 4-6 (a), exhibited typical rheological behavior of PAN dopes, characterized by shear-thinning at high shear rates [125]. The viscosities at low shear rates showed a slight decrease with increasing water content, while the onset shear

rates for shear-thinning remained the same regardless of water content. The presence of a high water content in PAN dopes can influence viscosity through various mechanisms [118, 126]. Initially, the viscosity decreases with increasing water content due to the water molecules facilitating weak interactions between PAN and DMF molecules, thereby increasing the concentration of molecular coils of PAN molecules [127]. However, as the water content continues to increase, the viscosity fsubsequently increases due to intermolecular interaction aggregation [15]. The water content of the PAN dope solution remained below 0.3 wt%, and the adsorbed water molecules primarily interacted with the PAN molecules.

To assess the homogeneity of the dope solutions, Han plots were employed, as depicted in Figure 4-6 (b). Han plots derived from flow sweep data had an identical slope of approximately 1.7, which is lower than the value of 2 for an ideally homogeneous solution [65]. Despite not achieving ideal homogeneity, moisturization did not have a significant impact on the homogeneity of the dope solutions.

In addition, the effect of moisturization on intermolecular chain interactions was examined using Casson plots, as illustrated in Figure 4-6 (c). Casson plots were constructed based on Casson's equation (equation (1)), which describes the relationship between the angular frequency and loss modulus [65].

$$\sqrt{G''} = \sqrt{\sigma_0} + \sqrt{k\omega} \quad (1)$$

where G" is the loss modulus, σ_0 is the critical stress, k is the viscosity coefficient, and ω is the angular frequency, respectively. Based on the Casson plots, it can be observed that the chain interaction was negligible, as indicated by the zero y-intercept, which signifies the absence of critical stress. Consequently, the rheological changes associated with increasing water content were not substantial. The rheological properties of the dope solution were not significantly influenced by the water content.

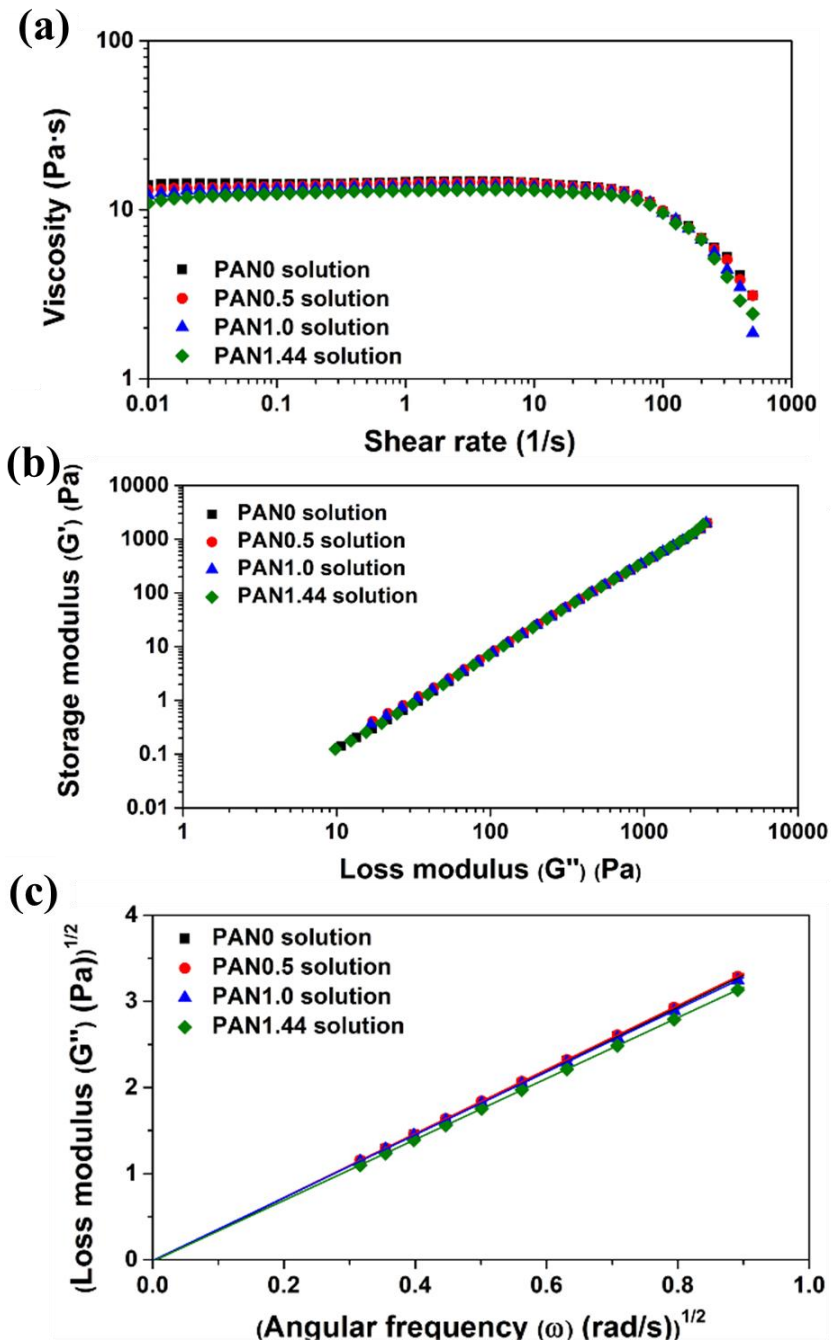

Figure 4-6. Rheological behavior in dope solution. (a) dynamic viscosity curves, (b)Han plots, and (c) Casson plots of dried and moisturized PAN (PAN0, PAN0.5, PAN1.0, and PAN1.44) dope solutions.

4.2. Fabrication of moisturized PAN fibers

4.2.1. Process condition and characterization method

DPAN and moisturized PAN were dissolved in DMF at 20 wt% to prepare the dope solutions, denoted as PAN0, PAN0.5, PAN1.0, and PAN1.44, for which the numbers represent the moisture contents The experimental setup for both lab-scale wet-spinning and electrochemical wet-spinning followed the procedures outlined in Chapter 2, with some modifications. The dope solutions were extruded into a coagulation bath consisting of a mixture of DMF and distilled water in a ratio of 7:3. This extrusion process occurred at a flow rate of 23.6 mL/h and at room temperature. A jet stretch ratio of 0.94 was applied during the extrusion stage. Subsequently, the coagulated PAN fibers underwent a series of washing and stretching steps in three separate baths. In the first bath, a 5:5 mix of DMF and distilled water was used, and the fibers were stretched at a ratio of 1.91. This was followed by a second bath containing water at a temperature of 70 °C, with the fibers being stretched at a ratio of 1.56. Lastly, the fibers were washed in distilled water at a temperature of 90 °C, with a stretch ratio of 2.93 applied. During the drying phase, residual DMF and water were removed at 70 °C. Afterward, the PAN fibers were wound with a total stretch ratio of 8.18. For electrochemical wet-spinning, 60 V was applied using an electrometer (6517B, Keithley).

The morphologies of the PAN fibers were examined using field-emission scanning electron microscopes (SUPRA 55VP from Carl Zeiss and SU8010 from Hitachi Co.). Chemical bonds and residual solvents in the molecular structures were assessed by Fourier-transform infrared spectroscopy (FT-IR; Nicolet 6700; Thermo Fisher Scientific). The microstructures of PAN fibers were characterized by wide-angle X-ray diffraction (WAXD) (D8 Discover; Bruker) and small-angle X-ray scattering (SAXS) (Xeuss 2.0; Xenocs). The radiation wavelength of both WAXD and SAXS was 0.154 nm (Cu Kα). WAXD is a good way to analyze crystallinity and crystal orientation [95, 128, 129], while SAXS is a useful way to evaluate voids in the microstructure of fibers [130, 131]. The mechanical properties of PAN fibers were measured using a FAVIMAT+ single-fiber tester (FAVIMAT+ AIROBOT2; Textechno) with a 25-mm gage length and crosshead speed of 5 mm min^{-1} in accordance with the standard ASTM D3822-14. The tensile strength was analyzed using fiber diameters measured from SEM images; 30 specimens were tested for each sample.

4.2.2. Basic characterization

PAN fibers were wet-spun from the dope solutions (Figure 4-7). The samples were labeled as GPAN0, GPAN0.5, GPAN1.0, and GPAN1.44, with the numbers indicating the water content. Interestingly, there was minimal variation in the morphologies among the wet-spun samples. Cross-sectional scanning electron microscopy (SEM) images of the GPAN samples revealed circular morphologies. The average diameters of the GPAN0, GPAN0.5, GPAN1.0, and GPAN1.44 fibers were measured as 9.95 ± 0.41, 9.01 ± 0.64, 9.57 ± 0.42, and 9.16 ± 0.43 μm, respectively. When examining the surface SEM images of the GPAN fibers, they typically displayed striped surface morphologies along the fiber axes.

The FT-IR data presented in Figure 4-8 indicate that moisturization of PAN did not lead to any significant molecular structural changes. The peak at 1,664 cm^{-1}, attributed to the amide peak of residual DMF, was evident in the FT-IR spectra of the GPAN fibers [86], and the peaks of the AN-derived CH_2 antisymmetrical and symmetrical vibrations (2,920 cm^{-1} and 2,840 cm^{-1}, respectively), C≡N (2,242 cm^{-1}), and CH_2 deformation (1,440 cm^{-1}) and of MA derived C=O stretching (1,730 cm^{-1}), O–CH_3 deformation (1,380 cm^{-1}), and C–O stretching (1,255 and 1,090 cm^{-1}) were observed [122, 123].

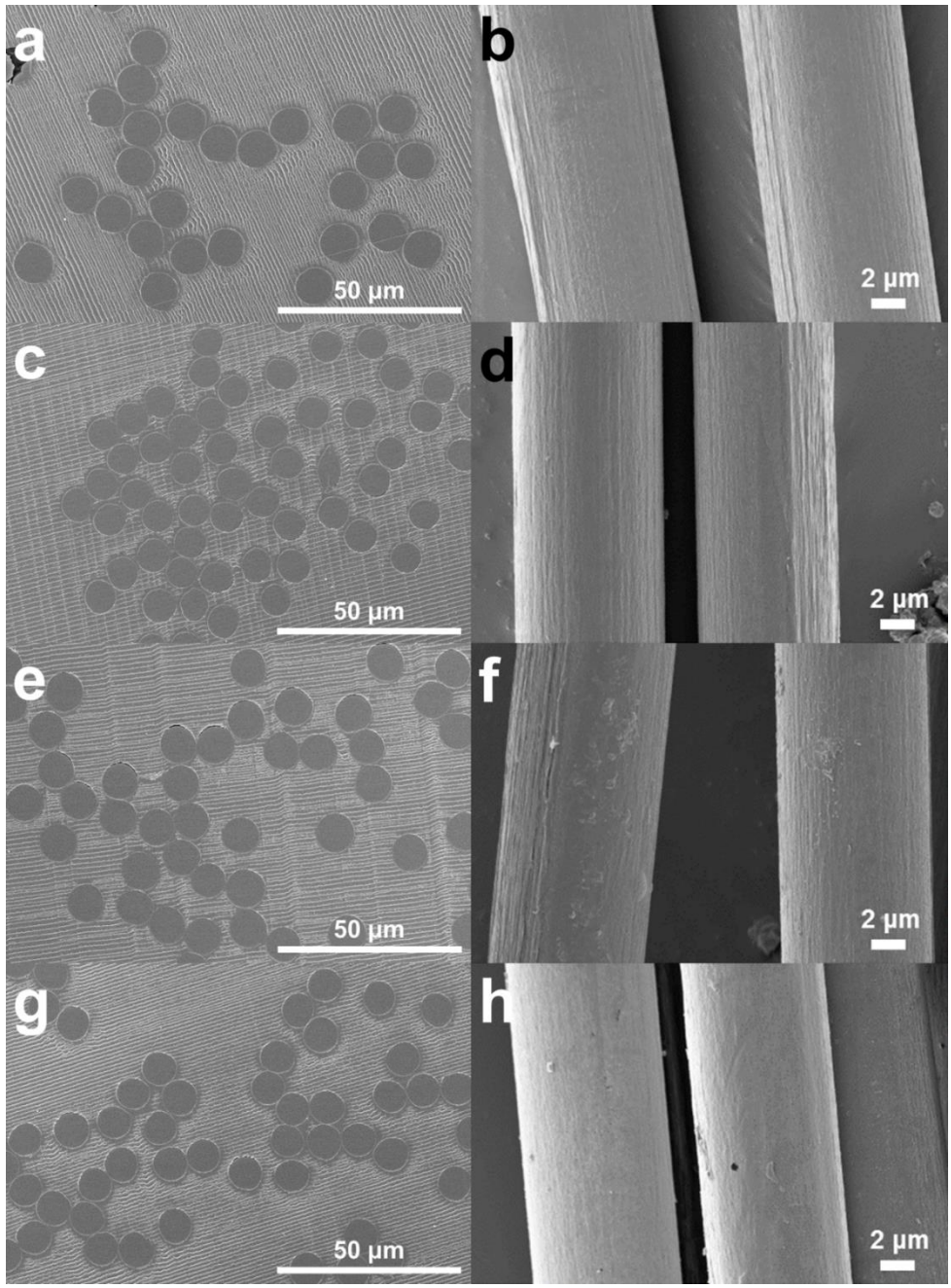

Figure 4-7. Scanning electron microscopy (SEM) images of cross-sections an d surface structures of GPAN fibers. (a, b) GPAN0, (c, d) GPAN0.5, (e, f) GPAN1.0, and (g, h) GPAN1.44.

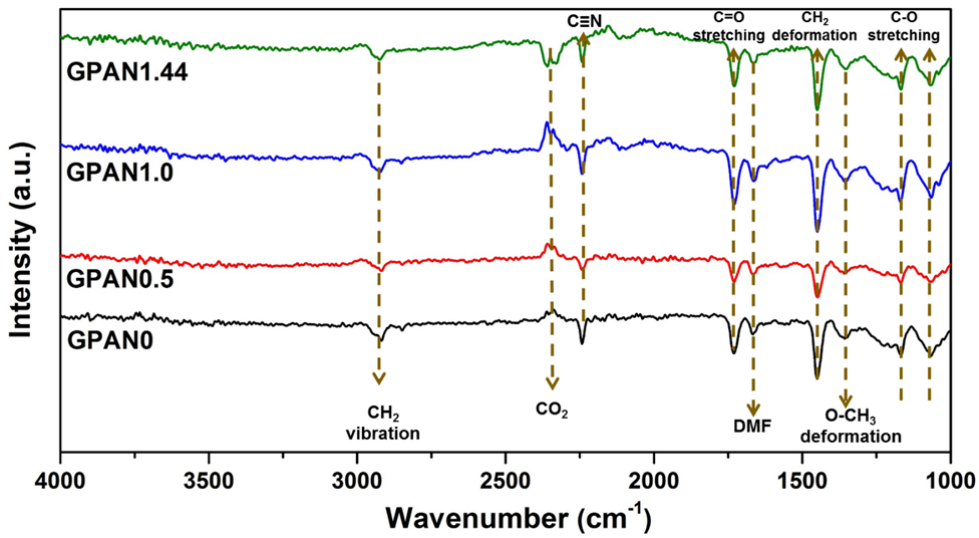

Figure 4-8. Fourier transform-infrared (FT-IR) spectra of GPAN fibers.

The effect of moisturization on the mechanical properties of PAN fibers was investigated using electrochemical wet-spinning, and the morphologies of the resulting fibers are shown in Figure 4-9. The sample codes are denoted as EPAN0, EPAN0.5, EPAN1.0, and EPAN1.44, where the numbers indicate the adsorbed water content. Similar to the GPAN fibers, the EPAN fibers exhibited a uniform morphology with no significant differences among the samples in terms of spinnability or diameter. The average diameters of the EPAN0, EPAN0.5, EPAN1.0, and EPAN1.44 fibers were 9.93 ± 0.34, 9.34 ± 0.31, 9.41 ± 0.34, and 9.05 ± 0.21 μm, respectively. These measurements indicate that the presence of moisture did not have a significant impact on the fiber diameters. However, it should be noted that the surface stripes observed in the SEM images of the EPAN fibers were more prominent compared to those of the corresponding GPAN fibers. This suggests that

the surface morphology of the fibers may be influenced by the electrochemical wet-spinning process and the presence of moisture.

According to the FT-IR data presented in Figure 4-10, moisturization did not lead to significant structural changes in the copolymer present in the EPAN fibers. The amide peak at 1,664 cm^{-1} was less intense in the EPAN0.5, EPAN1.0, and EPAN1.44 samples compared with the EPAN0 sample, which indicates less residual DMF [86]. This reduction in residual DMF can be attributed to the prevention of DMF adsorption by the more readily adsorbed water molecules. The reduced DMF adsorption was not expected to affect the strength of the EPAN fibers.

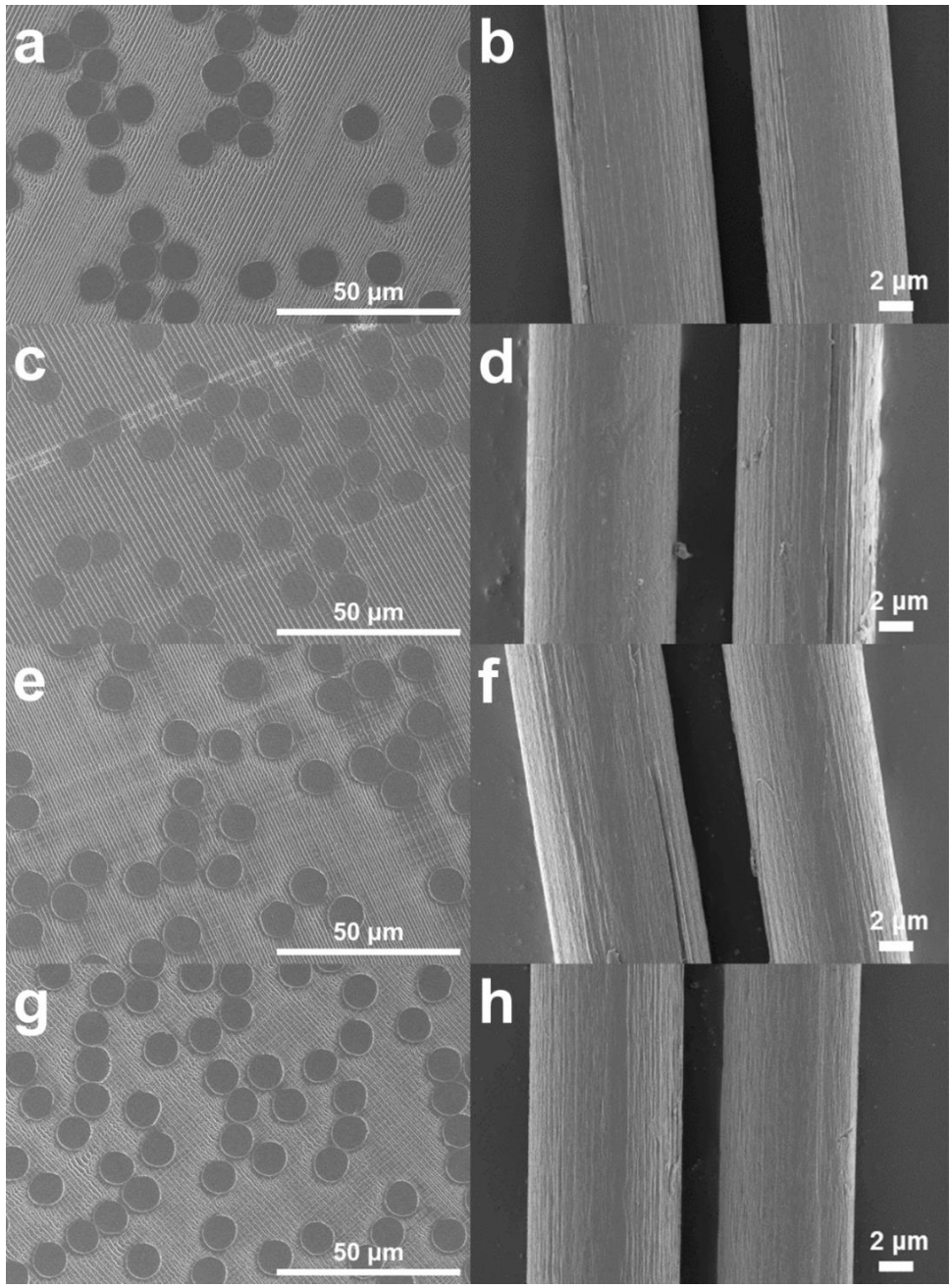

Figure 4-9. Scanning electron microscopy images of the cross-sections and s urface structures of EPAN fibers: (a, b) EPAN0, (c, d) EPAN0.5, (e, f) EP AN1.0, and (g, h) EPAN1.44.

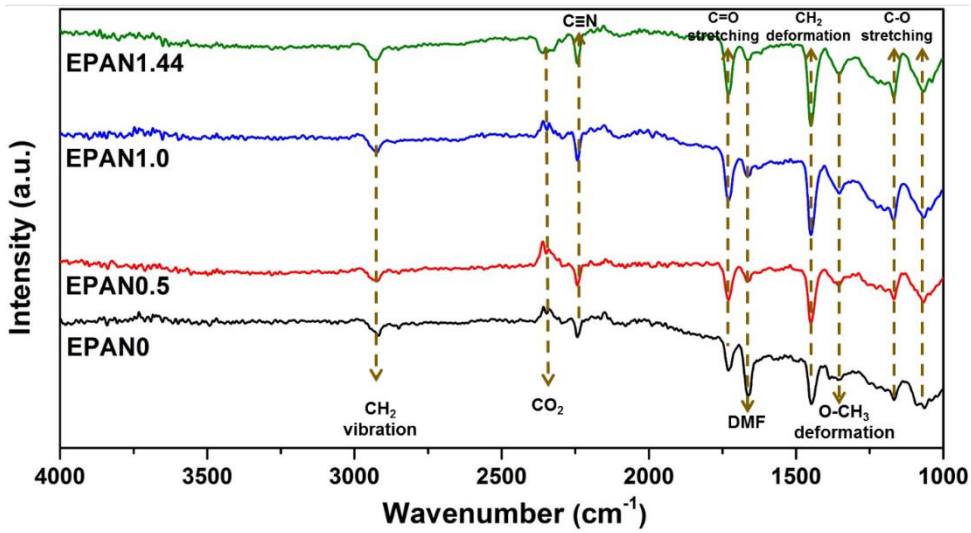

Figure 4-10. Fourier transform-infrared (FT-IR) spectra of EPAN fibers.

4.2.3. Microstructural and mechanical characterization

The presence of voids within the microstructure of GPAN fibers plays a crucial role in determining their strength [58]. Moisturization, which involves water adsorption by the macromolecules, can impact the formation of these voids. In order to investigate the effect of moisturization on voids in GPAN fibers, a two-dimensional small-angle X-ray scattering (2D SAXS) was utilized (Figure 4-11) [130, 131]. The void structures were quantified in terms of void length and angle, assuming a cylindrical shape, as the coagulation process elongates and stretches the voids into needle-like structures [132]. Ruland's streak method, which was also utilized in Chapter 2, was utilized to calculated the void structures of GPAN fibers, using azimuthal scans as a function of 2θ (γ integration) [58]. The average void length and angle were then calculated based on the analysis, as depicted in Figure 4-12 (b).

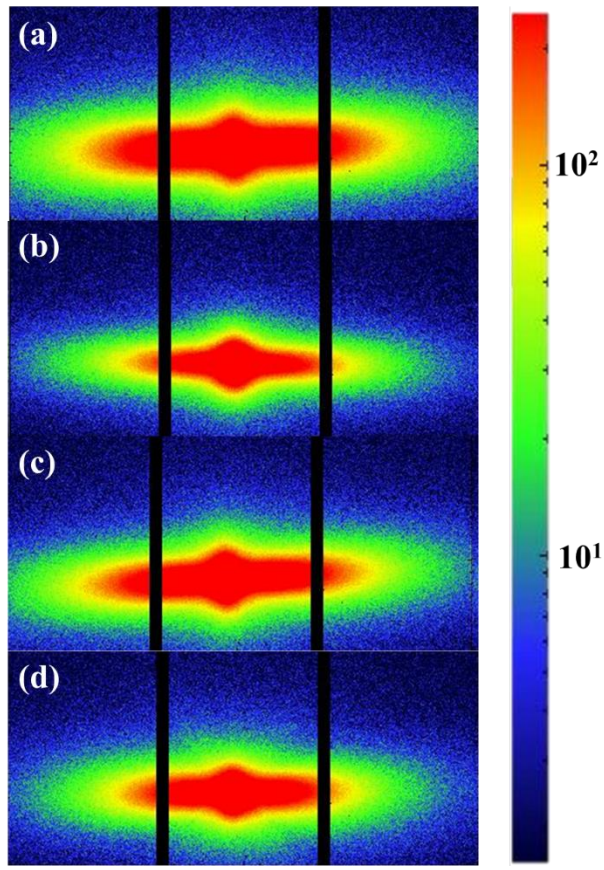

Figure 4-11. Void structure characterization of GPAN fibers. Two-dimensional small-angle X-ray scattering (2D-SAXS) images.

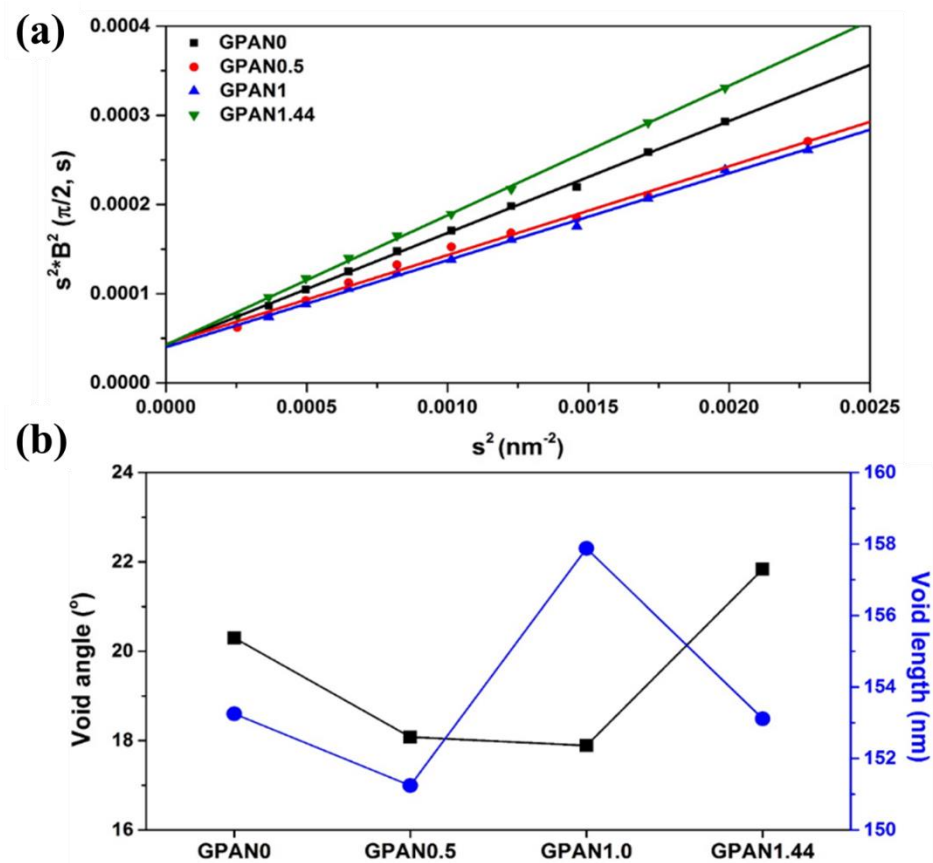

Figure 4-12. Void structure characterizations of the GPAN fibers. (a) Ruland linear fittings, and (b) void angle and void length.

The GPAN0.5 sample exhibited the least void structures, with the lowest void angle (17.79°) and void length (147.84 nm). This indicates that the presence of voids as the source of fiber fracture was minimized in this sample. The reduction in void structures at a water content of 0.5 wt% can be attributed to the enhanced nucleophilicity of MA, facilitated by the adsorbed water molecules. This improved nucleophilicity leads to enhanced interactions between the electrophilic hydrocarbon

side and the nucleophilic side of the chain, thereby minimizing void formation. On the other hand, the GPAN1.0 sample exhibited increased void length and decreased void angle compared to GPAN0, while the GPAN1.44 sample showed the opposite trend. These changes in void structures can be attributed to the complex interactions among the macromolecules and an excess amount of water molecules. The excess water can lead to disrupted interactions and increased void formation. Based on these findings, it can be concluded that the absorption of water can contribute to the improvement of strength by minimizing void defects in GPAN fibers.

The crystallographic structures of the GPAN fibers were analyzed using wide-angle X-ray diffraction (WAXD), and the results are shown in Figure 4-13. The two-dimensional (2D) WAXD patterns revealed a preferred orientation of PAN molecules along the fiber axes in all GPAN samples (Figure 4-13 (a)-(d)). The crystallographic (crystallinity, crystal size and preferred orientation) of the GPAN fibers were calculated using the same method as described in Chapter 2. To extract one-dimensional WAXD curves, the intensities of the 2D patterns were integrated, resulting in peaks at approximately $2\theta = 17°$ and 30° (Figure 4-13 (e)). The intense peak at around $2\theta = 17°$ corresponds to the (100) direction of the PAN molecules, while the weak peak at around $2\theta = 30°$ is assigned to the (110) direction [133]. These peaks indicate the presence of crystalline regions in the GPAN fibers. The calculated crystallinities of the GPAN fibers ranged from 44.55% to 46.11% and tended to increase with increasing water content. The crystallinity values were determined based on the areal ratio of the WAXD curves, providing an estimation of

the degree of ordering in the polymer chains. Overall, the WAXD analysis confirmed the presence of preferred molecular orientation and crystalline regions in the GPAN fibers. The crystallinity tended to increase with higher water content, suggesting that water molecules may influence the polymer chain arrangement and promote crystallization in the fibers.

The crystal sizes of the GPAN fibers were determined to be approximately 3.1 nm with less than 2.6% variation among the samples. The preferred orientations of the GPAN fibers were determined by analyzing the peak integrations of the azimuthal scans at $2\theta = 17°$ in Figure 4-13 (f). It was observed that the preferred orientations became less evident with increasing water content. The preferred orientation indicates the alignment of the polymer chains along a specific direction, contributing to the overall structural properties of the fibers. In Table 4-1, a summary of the crystallographic structures of the GPAN fibers is presented. The fibers exhibited relatively high crystallinity with reduced preferred orientation as the water content increased. These structural changes can be attributed to the accelerated crystallization facilitated by the intimate interaction between the adsorbed water molecules and the coagulation solvent mixture. This interaction promoted the formation of well-defined crystalline regions in the fibers. The GPAN0.5 sample, which showed minimized void structures and high preferred orientation, was expected to possess the greatest strength among the tested samples. The combination of reduced voids, larger crystal sizes, and strong preferred orientation contributes to enhanced mechanical properties and overall fiber strength.

Table 4-1. Crystallinity, crystal size and preferred orientation of GPAN fibers.

	GPAN0	GPAN0.5	GPAN1.0	GPAN1.44
Crystallinity (%)	44.55	44.97	45.77	46.11
Crystal size (nm)	3.18	3.16	3.10	3.15
Preferred orientation (%)	76.44	75.27	70.96	73.20

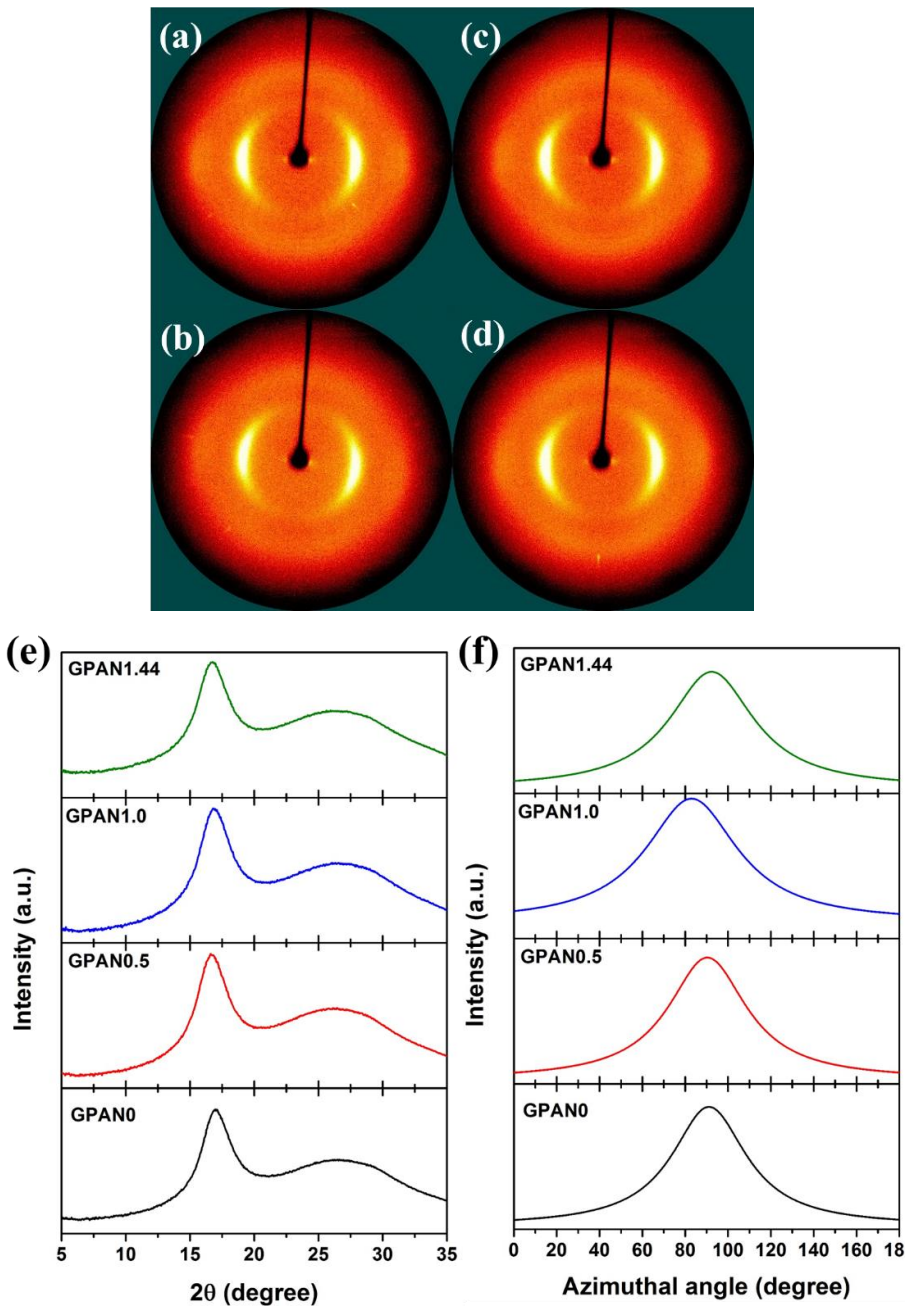

Figure 4-13. Microstructural characterizations of the GPAN fibers. Two-dime nsional wide-angle X-ray diffraction (2D-WAXD) images of (a) GPAN0, (b) GPAN0.5, (c) GPAN1.0, and (d) GPAN1.44. (e) Equatorially extracted one-d imensional WAXD curves and (f) azimuthal scans at 2θ = 17°.

The void structures of the EPAN fibers were investigated using SAXS, as shown in Figure 4-14. The void analysis was conducted using Ruland's streak method, which was also employed in Chapter 2. Azimuthal scans as a function of 2θ were used to calculate the void structures of the EPAN fibers, as depicted in Figure 4-15 (a) [58]. The results displayed in Figure 4-15 (b) indicate that the EPAN0.5 fibers exhibited the lowest void angle (16.88°). Additionally, the EPAN1.0 fibers exhibited the shortest void length (127.56 nm), which is approximately 15% smaller than that observed in EPAN0. However, the voids in EPAN0.5 and EPAN1.44 were slightly longer compared to EPAN0, potentially due to suboptimal water distribution after the demethylation process. Based on these, it can be inferred that the EPAN1.0 fibers are expected to possess the highest strength. This is attributed to the significant reduction in void length while exhibiting minimal reduction in void angle, indicating an improved structural configuration with enhanced mechanical properties.

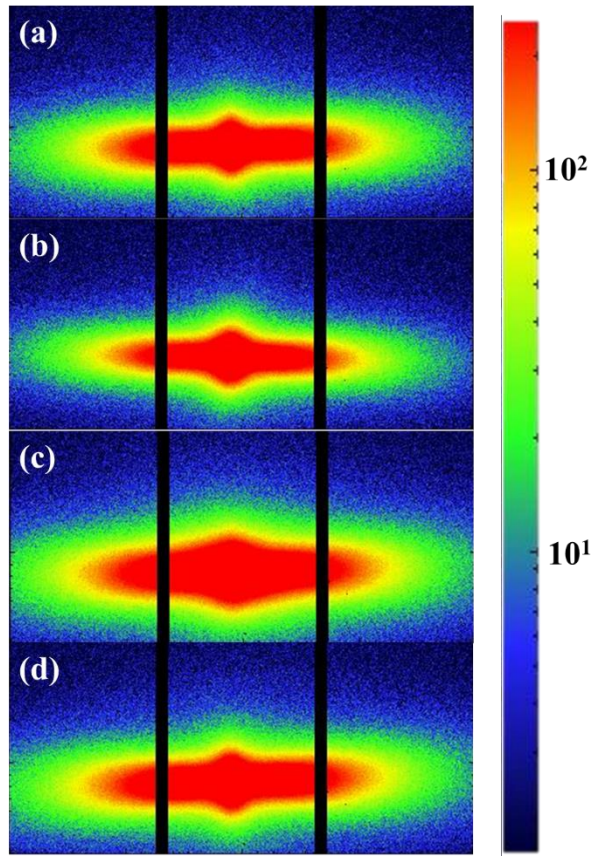

Figure 4-14. Void structure characterization of GPAN fibers. Two-dimensional small-angle X-ray scattering (2D-SAXS) images.

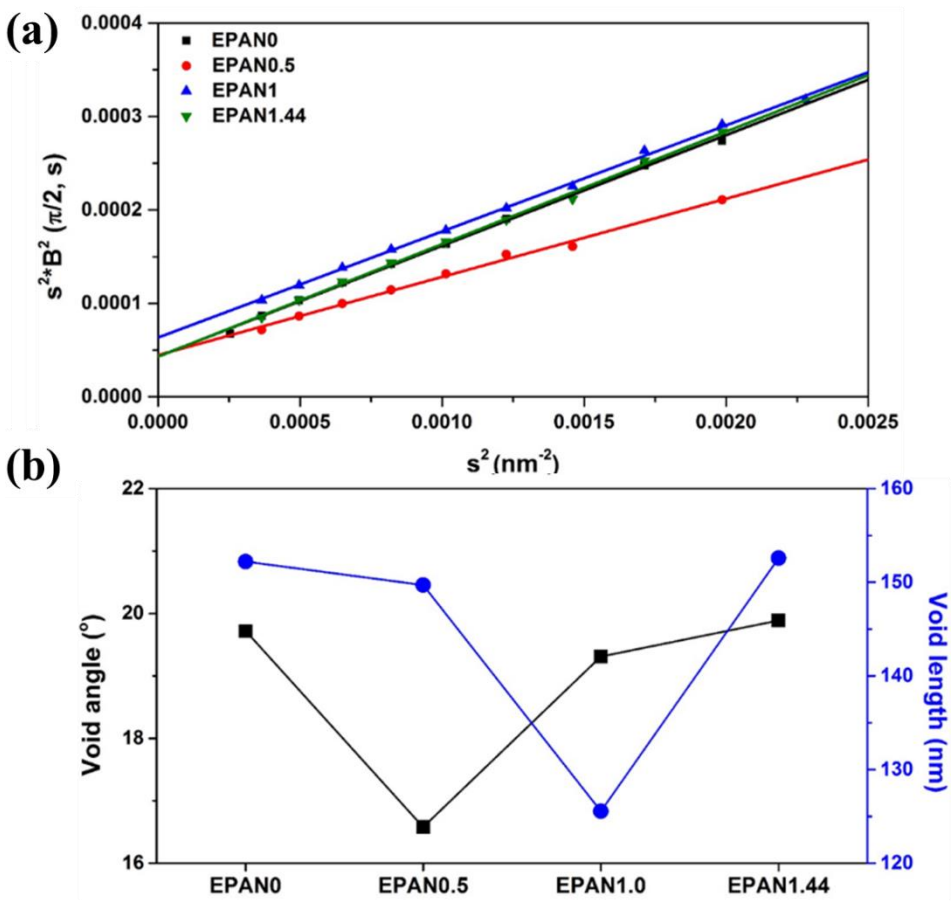

Figure 4-15. Void structure characterization of the EPAN fibers. (a) Ruland linear fittings, and (b) void orientation and void length.

The crystallographic structures of the EPAN fibers were analyzed using WAXD, as depicted in Figure 4-15. The 2D WAXD patterns in Figure 4-16 (a)-(d) indicate a preferred orientation of the PAN copolymer molecules along the fiber axes. The equatorially extracted one-dimensional WAXD curves in Figure 4-16 (e) show prominent peaks at approximately 2θ = 17° (strong) and 30° (weak), corresponding

to the (100) and (110) directions of the PAN molecules, respectively [133]. The moisturized EPAN fibers exhibited slightly increased crystallinities (~45%) with increasing water content, although the changes were not substantial. The crystallite sizes were approximately 3.10 nm. The preferred orientations were calculated based on the peak integrations of the azimuthal scans at $2\theta = 17°$ in Figure 4-16 (f). It was observed that the EPAN0.5 and EPAN1.0 samples had higher preferred orientations (>75%) compared to EPAN0 (72.58%) and EPAN1.44 (67.71%). The summarized crystallographic structures of the EPAN fibers are presented in Table 4-2. The minor differences in the crystalline structure between EPAN0.5 and EPAN1.0 were not considered detrimental to the strength of the fibers. Therefore, it can be inferred that the EPAN1.0 fibers, with minimized void length and high preferred orientation in the copolymer molecules, are expected to exhibit the highest strength among the samples.

Table 4-2. Crystallinity, crystal size and preferred orientation of EPAN fibers.

	EPAN0	**EPAN0.5**	**EPAN1.0**	**EPAN1.44**
Crystallinity (%)	45.80	44.87	45.64	46.33
Crystal size (nm)	31.97	31.93	31.01	31.64
Preferred orientation (%)	72.58	75.29	75.06	67.71

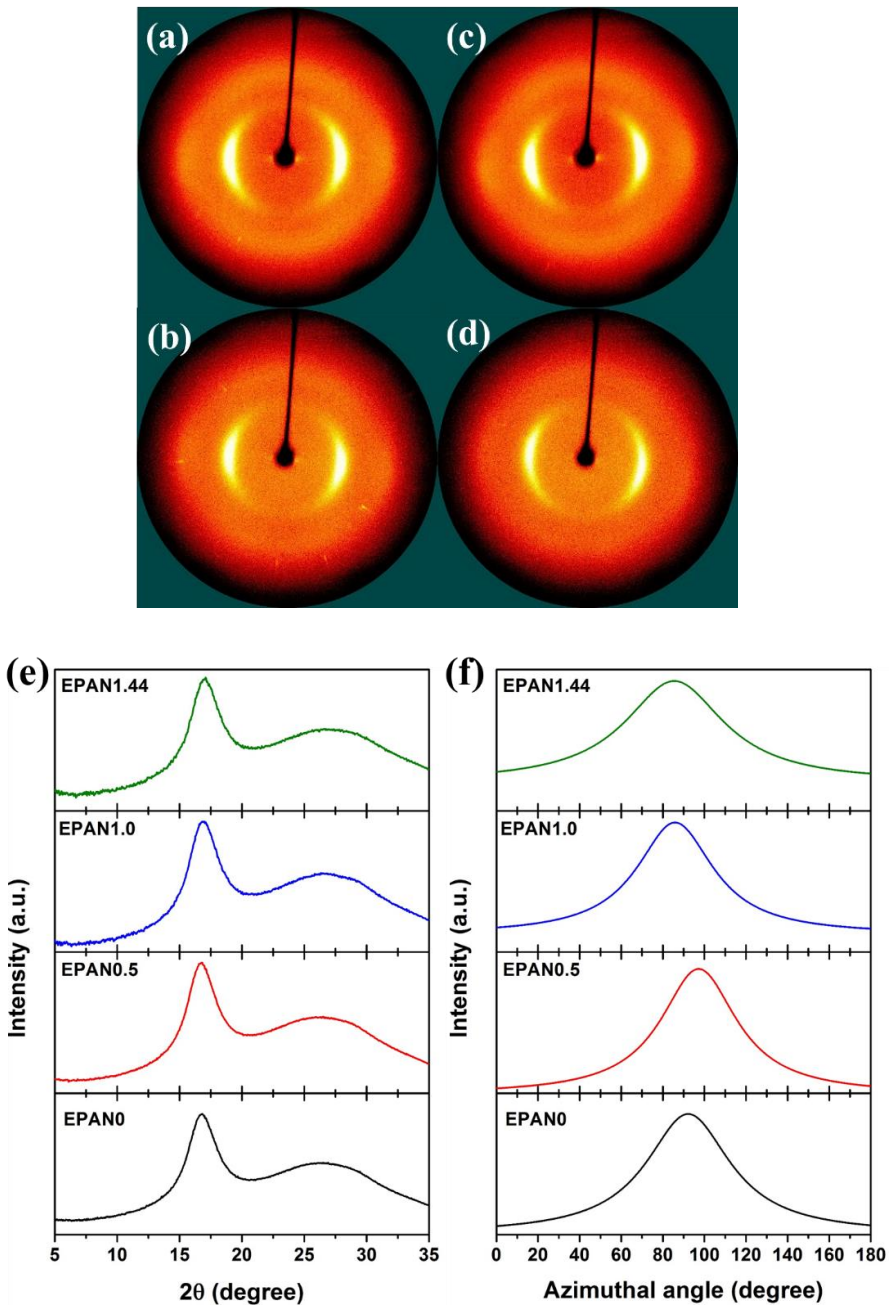

Figure 4-16. Microstructural characterization of the EPAN fibers. Two-dimensional wide-angle X-ray diffraction (2D-WAXD) images of (a) EPAN0, (b) EPAN0.5, (c) EPAN1.0, and (d) EPAN1.44. (e) Equatorially extracted one-dimensional WAXD curves. (f) Azimuthal scans at $2\theta = 17°$.

Single-filament mechanical properties were assessed to validate the effect of moisturization and compare the optimal water adsorption levels between conventional and electrochemical wet-spinning processes. Among the GPAN fibers, GPAN0.5 exhibited the highest strength with the lowest breaking strain, while the other GPAN fibers showed similar strengths but varying breaking strains, as depicted in Figure 4-17 (a). In the coagulation process, the diffusion of non-solvent into the dope solution in the coagulation bath leads to coagulation, results in coagulation induced by the trade-off between the solvent and nonsolvent composition of the dope solution. As the fiber surface solidifies, the coagulation rate decreases, resulting in phase separation-driven inhomogeneities in the fiber microstructures and reduced mechanical properties [134, 135]. These inhomogeneities in the copolymer may have contributed to the observed electrostatic effect. The optimal mechanical properties in the GPAN samples were observed at a water content of 0.5%. However, the strongest EPAN fibers, with the shortest void length, were obtained at a water content of 1.0%, as shown in Figure 4-17 (b). This can be attributed to the enhanced intermolecular interactions among the copolymer molecules, particularly optimizing the electrostatic interaction at a water content of 1.0%. Additionally, the EPAN1.0 sample exhibited the highest strain at the point of breakage.

In Figure 4-17 (c), a comparison of the strength data is presented. As in chapter 2 and 3, the EPAN fibers exhibited greater strength compared to the GPAN fibers. In both groups, the adsorbed water initially had a positive effect on the strength, but excessive water content had a detrimental impact. The Young's moduli of both

GPAN and EPAN fibers remained relatively constant within the range of 11-12 GPa. The breaking strain of the GPAN fibers did not show a clear trend, whereas the breaking strain of the EPAN fibers was synchronized with the changes in strength.

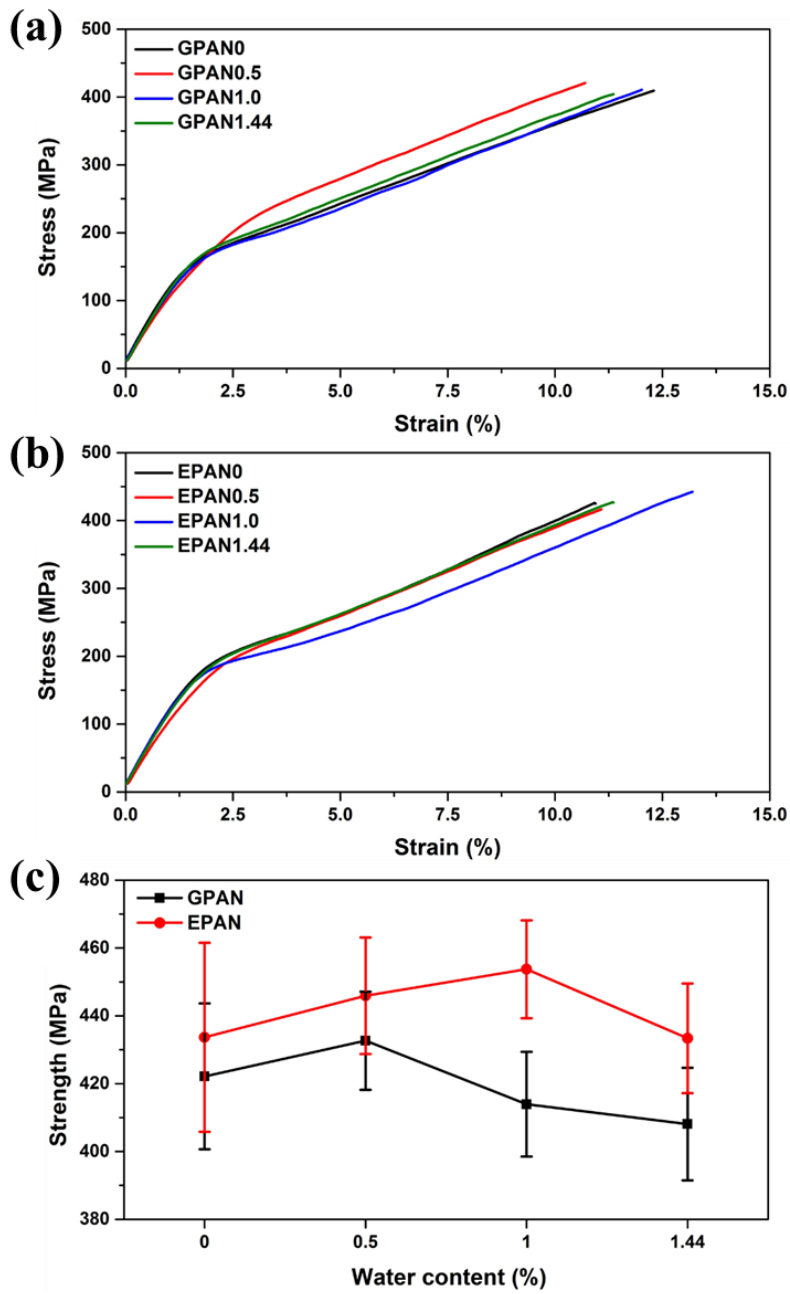

Figure 4-17. Mechanical properties of the GPAN and EPAN fibers. (a, b) Stress–strain curves of (a) GPAN and (b) EPAN fibers. (c) Strength comparison of GPAN and EPAN fibers.

4.2.4. Moisturization effects on PAN fibers

The PAN-MA copolymer possesses inherent hygroscopic properties, allowing for the manipulation of the material characteristics of PAN fibers by adjusting the electrostatic properties of the molecules and the resulting intermolecular interactions influenced by absorbed water. However, the extent of water adsorption is susceptible to external factors such as temperature, humidity, and pressure. Hence, precise management of the adsorbed water content is critical in order to uphold and enhance the performance of the PAN fiber.

During the wet-spinning process, the copolymer molecules undergo reorganization to form a polymer crystal. There is a likelihood of close interaction between the backbone and nitrile group, while the presence of the electrophilic backbone and the methyl group of MA can lead to electrostatic repulsion, potentially disrupting this interaction. Figure 4-18 (a) illustrates the electrostatic potential distribution of the copolymer, where the hydrocarbon backbone exhibits electron-poor characteristics (blue color), the nitrile group is electron-rich (red color), and the MA displays partial electron-poor properties in the methyl group and partial electron-rich properties in the acrylate group. Consequently, it is certain that electrostatic repulsion hinders the intimate intermolecular interaction between MA and the backbone. Simultaneously, water molecules tend to selectively adsorb onto the acrylate group due to its high electron density, which facilitates strong attraction to the hydrogen atoms of water molecules. The presence of adsorbed water compensates for the reduced nucleophilicity caused by the methyl group, as depicted in Figure 4-18. The optimal

hydration weight fraction, relative to the copolymer weight, is assumed to range from 0.34 to 0.68 wt% (equivalent to 1.9 to 3.8 mol%) because within this range, one to two equivalents of water can form a single-layer arrangement on the MA in the copolymer (3.8 mol%). If demethylation occurs in the MA during the electrochemical wet-spinning process, it results in the formation of a resonance-stabilized acrylate anion with an exposed region of high electron density (–COO–) [136]. Accordingly, it is expected that the optimal hydration rate would require twice the amount of water (i.e., 0.68 to 1.36 wt%) due to the presence of two electron-rich regions in the demethylated MA (Figure 4-18). The copolymers were subjected to demoisturization and subsequent hydration, as illustrated in Figure 4-18.

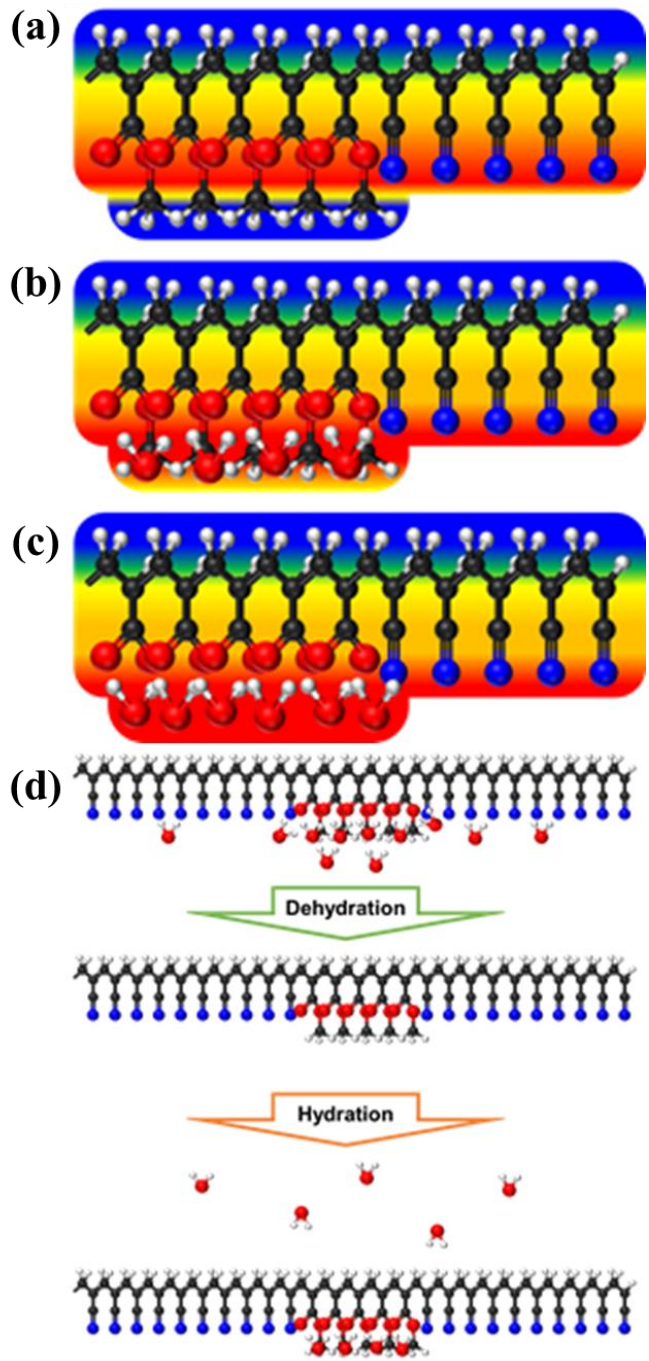

Figure 4-17. Schematic illustration of PAN-MA molecules with adsorbed wa ter. Electrostatic potential maps of (a) raw, (b) hydrated, and (c) demethylate d/hydrated PAN-MA molecules and (d) the sample preparation procedure.

4.3. Summary

The controlled adsorption of water on PAN-MA copolymer was investigated to examine its effect on the mechanical properties of PAN fibers. The molecular structure and characteristics of the dope solution were found to be unaffected by the amount of adsorbed water. Minimizing voids resulted in the highest strengths in the GPAN0.5 and EPAN1.0 PAN fibers. In GPAN0.5 fibers, the optimal amount of water enhanced the nucleophilicity of MA and facilitated improved intermolecular interactions between the electrophilic hydrocarbon side and the nucleophilic electronegative side. This led to enhanced strength properties. Similarly, in EPAN1.0 fibers, the highest strength was attributed to the intimate interaction between the stabilized demthylated MA ($-CH_3COO^-$) and an equivalent amount of double the adsorbed water. This interaction contributed to the improved mechanical performance.

Chapter 5. Molecular weight distribution (MWD) and spinnability

Extensive research has been conducted to enhance the properties of PAN fiber, with a straightforward approach being the design of its raw material, PAN. The properties of polymer materials are significantly influenced by the molecular weight of the polymer. Increasing the molecular weight results in higher entanglement of polymer chains, leading to improved properties [27, 137, 138]. Consequently, studies have focused on polymerizing high molecular weight PAN to enhance the properties of PAN fiber [12, 26-28]. However, increasing the molecular weight also leads to a significant exponential increase in the viscosity of the solution [139, 140]. The viscosity of the solution plays a vital role in the spinnability of PAN fiber, which is produced through the wet-spinning process. Unfortunately, as the viscosity of the solution rises, the spinnability decreases substantially. To address this issue, researchers have explored various methods, such as raising the temperature [141-144], using mixed solvents [141, 145], and reducing the polydispersity index (PDI) [29-31], to achieve a more efficient PAN fiber production process by reducing viscosity. However, increasing the temperature has limitations due to the potential degradation of PAN, despite effectively reducing its viscosity. Similarly, reducing the PDI poses challenges for commercialization as it requires the use of catalysts like RAFT.

The bimodal molecular weight distribution of polymers, commonly investigated in the polyethylene, involves blending high molecular weight and low molecular weight polymers. This strategy aims to enhance the mechanical properties of materials using the high molecular weight polymer, while simultaneously improving processability with the low molecular weight polymer. By utilizing both high and low molecular weight polymers, different polymer crystal formations occur under distinct conditions, thereby influencing the microstructure of the polymer material [146-148].

In this chapter, the focus was on utilizing bimodal molecular weight distribution PAN to develop of wet-spinning process for manufacturing high-strength PAN fiber with improved spinnability. The effect of bimodal molecular weight distribution PAN on both spinnability of wet-spinning process and mechanical properties of PAN fibers was investigated. By blending high molecular weight PAN and low molecular weight PAN, it was anticipated that the average molecular weight would decrease, resulting in reduced viscosity and improved spinnability. However, the reduction in polymer chain entanglement caused by the low molecular weight PAN led to a decrease in the mechanical properties of PAN fibers. Nevertheless, blending low and high molecular weight PAN leads to variations in coagulation processess inducing microstructural changes that influenced the mechanical properties. Hence, determining the optimal ratio of bimodal molecular weight distribution PAN through characterization of its properties in dope solution and wet-spun fibers is crucial to achieve significant improvements in both spinnability and mechanical properties. In

order to achieve this, PAN fiber manufacturing and characterization were carried out for various combinations of bimodal molecular weight distribution PAN, with different molecular weight ratios.

5.1. Polymer preparation

5.1.1. Polymerization of PAN with various molecular weight

To fabricate bimodal molecular weight distribution PAN fiber, low molecular weight PAN (LMW) and high molecular weight PAN (HMW) were separately polymerized. Suspension polymerization was used to polymerize LMW and HMW [12, 35]. The monomer materials used were acrylonitrile (AN, 99%, Dajung Chemical), and methyl acrylate (MA, Sigma-Aldrich) was used as a comonomer. The targeted copolymer ratio in PAN was 6wt%, and dimethylsulfoxide (DMSO, 99.5%, Dajung Chemical) was used as the solvent. Targeting molecular weight PAN was polymerized through concentration changes of initiator and catalyst. Ammonium persulfate (APS, ≧98.0%, Sigma-Aldrich) and sodium bisulfite (SBS, Sigma-Aldrich) were used as initiators, and iron(II) sulfate heptahydrate ($FeSO4 \cdot 7H2O$, ≥99.0%, Sigma-Aldrich) was acted as the catalyst.

To characterize the effects of different molecular weight ratios in bimodal MWD, two distinct ratios of bimodal MWD PAN were synthesized and named A-bimodal MWD PAN and B-bimodal MWD PAN. In the case of A-bimodal MWD, the low molecular weight PAN was designated as A-LMW, while the high molecular weight was labeled as A-HMW. Similarly, for B-bimodal MWD PAN, the low molecular weight was referred to as B-LMW, and the high molecular weight as B-HMW. A-LMW, A-HMW, B-LMW, and B-HMW were polymerized through solution polymerization [78, 79]. The same monomers and solvents were used as in the

suspension polymerization. Targeting molecular weight PAN was polymerized through concentration changes of initiator. A,a'-azobis-isobutyronitile (AIBN, 99%, Dajung Chemical) was recrystallized and used as the initiator. To recrystallize AIBN, an excess of AIBN was dissolved in ethanol at 40°C and left at -5°C for 1 day, after which the precipitated AIBN crystals were filtered. In both polymerization methods, the resulting various molecular weight PAN was washed several times with distilled water and methanol and then dried in a vacuum environment at 80°C after washing with water and methanol.

5.1.2. Preparation of PAN dope with bimodal MWD

Molecular weights of LMW, HMW, A-LMW, A-HMW, B-LMW and B-HMW were measured by gel permeation chromatography (GPC, Ultimate 3000, Thermo). The composition of the comonomer of LMW, HMW, A-LMW, A-HMW, B-LMW and B-HMW was measured using a nuclear magnetic resonance spectrometer (1H NMR, Advance III-500, Bruker).

The molecular weights and comonomer ratios of the polymerized LMW and HMW were measured. Table 5-1 presents the results of the GPC analysis for LMW and HMW. The molecular weight of LMW was determined to be 272,000, while the molecular weight of HMW was found to be 465,000. The molecular weight difference between LMW and HMW is approximately 1.71 times. Table 5-2 shows the results of the ^{1}H NMR analysis for LMW and HMW. No significant difference in comonomer composition was observed between LMW and HMW. A dope solution with a concentration of 20 wt% was prepared by blending LMW and HMW. The HMW content in the dope solution was varied, resulting in samples labeled as HMW0, HMW25, HMW50, HMW75, and HMW100, depending on the proportion of HMW in dope solution.

Table 5-1. Molecular weight and polydispersity index(PDI) of LMW and HMW.

Sample	Molecular weight (M_w)	PDI
LMW	272,000	3.31
HMW	465,000	2.41

Table 5-2. ^{1}H NMR analysis of LMW and HMW.

Sample	AN (mol%)	MA (mol%)
LMW	96.32	3.68
HMW	96.29	3.71

To investigate the effects of different combinations of low molecular weight and high molecular weight, two different molecular weight ratios were examined: A-bimodal MWD PAN, A-LMW and A-HMW blend, and B-bimodal MWD PAN, B-LMW, and B-HMW.

The molecular weights of A-LMW, A-HMW, B-LMW, and B-HMW were determined and presented in Table 5-3. A-LMW had a molecular weight of 471,000, while A-HMW had a molecular weight of 711,000. The molecular weight difference between A-LMW and A-HMW is approximately 1.51 times. Based on the HMW content in the dope solution, the samples were named A-HMW0, A-HMW25, A-HMW50, A-HMW75, and A-HMW100. Similarly, B-LMW had a molecular weight of 221,000, and B-HMW had a molecular weight of 615,000. The molecular weight difference between B-LMW and B-HMW is approximately 2.78 times. Due to the significant molecular weight difference between B-LMW and B-HMW, it was not possible to wet-spun of the same concentration for B-HMW0 and B-HMW100 dope solutions. Therefore, B-bimodal MWD PAN doper solutions at 15 wt% was used. The dope solutions were prepared by adding a small amount of B-LMW. The samples were named B-HMW67, B-HMW80, B-HMW90, B-HMW95, and B-HMW100, depending on the HMW content in the dope solution.

Table 5-3. Molecular weight and polydispersity index(PDI) of A-LMW, A-HMW, B-LMW and B-HMW.

Sample	M_w	PDI
A-LMW	471,000	2.45
A-HMW	711,000	1.96
B-LMW	221,000	3.47
B-HMW	615,000	2.39

5.2. Fabrication of PAN fibers using bimodal MWD

5.2.1. Process condition and characterization method

Bimodal MWD PAN was dissolved in N,N-Dimethylformamide (DMF; purity : 99.8%; high performance liquid chromatography (HPLC) grade, Daejung Chemical) to prepare a dope solution. Bimodal MWD PAN (LMW and HMW blend) was dissolved at concentrations of 20 wt%.

The experimental setup for lab-scale wet-spinning followed the procedures outlined in Chapter 2. Dope solutions were extruded into a coagulation bath comprising a mixture of DMF and distilled water (7:3 ratio) at a flow rate of 23.6 mL/h and room temperature. A jet stretch ratio of 0.94 was applied. The resulting coagulated PAN fibers underwent a series of washing and stretching steps in three separate baths. The first bath contained a 5:5 DMF-water mixture with a stretch ratio of 1.91, followed by a second bath with water at 70 °C and a stretch ratio of 2.11. Lastly, the fibers were washed in distilled water at 90 °C with a stretch ratio of 2.16. After removing residual DMF and water at 70 °C during the drying phase, the PAN fibers were wound with a total stretch ratio of 8.18.

For A-bimodal molecular weight distribution PAN (A-LMW and A-HMW blend), a concentration of 12 wt% was dissolved, and for B-bimodal MWD PAN (B-LMW and B-HMW blend), a concentration of 15 wt% dissolved. The wet-spinning process was conducted following same procedures.

The rheological properties of the dope solutions were measured using a rheometer

(DHR-2; TA Instruments). The dope solutions were placed between two 40-mm-diameter parallel plates separated by 1 mm. Flow sweep in the shear rate range of 0.01–500 s−1 and frequency sweep in the angular frequency range of 0.1–500 rad s−1 were used to investigate the homogeneity of the dope solutions and the polymer chain intermolecular interactions of PAN in the dope solutions at room temperature. Morphologies of the PAN fibers were observed using field-emission scanning electron microscopes (FE-SEM, SUPRA 55VP from Carl Zeiss). Chemical bonds in the PAN fibers were assessed by fourier-transform infrared spectroscopy (FT-IR, Nicolet 6700, Thermo Fisher Scientific). The microstructures of fibers were characterized by 2D wide-angle X-ray diffraction (2D-WAXD, D8 Discover; Bruker) and 2D small-angle X-ray scattering (2D-SAXS, Xeuss 2.0, Xenocs) [90, 91]. The radiation wavelength of 2D-WAXD and 2D-SAXS was 0.154 nm (Cu Kα). The mechanical properties of PAN fibers were measured using a single-fiber tester (FAVIMAT, Textechno, Mönchengladbach) with a 20 mm gage length and a crosshead speed of 20 mm/min.

5.2.2. The effect of MWD on spinnability

The spinnability of PAN fibers is greatly influenced by their viscosity. The viscosities of bimodal MWD PAN dope solutions (HMW0, HMW25, HMW50, HMW75, and HMW100) were measured and presented in Figure 5-1. All of the bimodal MWD PAN dope solutions exhibited the expected rheological behavior of PAN solution, characterized as non-Newtonian fluids, with viscosity decreasing as shear rate increased, demonstrating shear thinning behavior [149, 150]. Specifically, at a shear rate of 1 (1/s), the viscosities were measured as 4.96, 10.15, 17.16, 27.01, and 56.02 Pa·s for HMW0, HMW25, HMW50, HMW75, and HMW100, respectively. Notably, an increase in the HMW ratio resulted in a steep rise in viscosity. This can be attributed to the increased average molecular weight due to the higher HMW ratio. It suggested that incorporating low molecular weight (LMW) PAN into HMW dope solutions with higher viscosity can lead to improved spinnability. By achieving a bimodal MWD solution through the blend of LMW and HMW, the spinnability of PAN fibers can be enhanced.

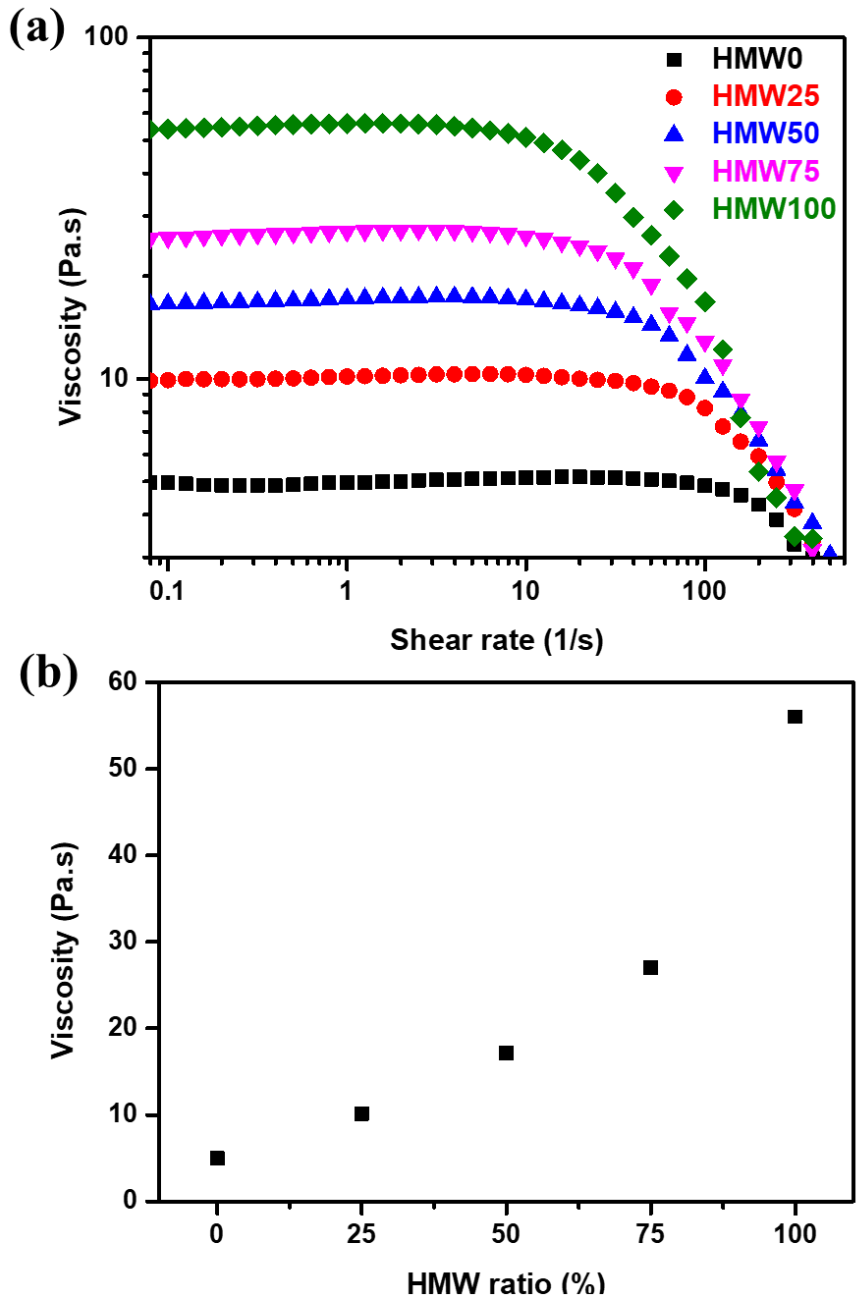

Figure 5-1. Viscosity of bimodal MWD PAN (HMW0, HMW25, HMW50, HMW75 and HMW100) in dope solution. (a) dynamic viscosity curves and (b) viscosity of bimodal PAN dope solution at shear rate is 1 (1/s).

To evaluate the homogeneity of the PAN dope solutions, Han plots were generated based on flow sweep data, as illustrated in Figure 5-2 (a). The slopes of the Han plots were found to be approximately 1.70 - 1.75, which is lower than the expected value of 2 for an ideally homogeneous solution [65]. Although the dope solutions did not exhibit perfect homogeneity, the blending of LMW and HMW did not significantly impact the homogeneity of the solutions.

Furthermore, the intermolecular chain interactions between the LMW and HMW polymer chains in the bimodal MWD PAN dope solutions were investigated using Casson plots, a previously utilized in Chapter 4, as shown in Figure 5-2 (b). The Casson plots revealed that the intermolecular chain interactions were negligible, as evidenced by the zero y-intercept, indicating the absence of critical stress. Therefore, the observed rheological changes in the bimodal MWD PAN dope solutions were primarily attributed to variations in viscosity. The homogeneity of the dope solutions and the intermolecular chain interactions between the polymer chains remained unaffected.

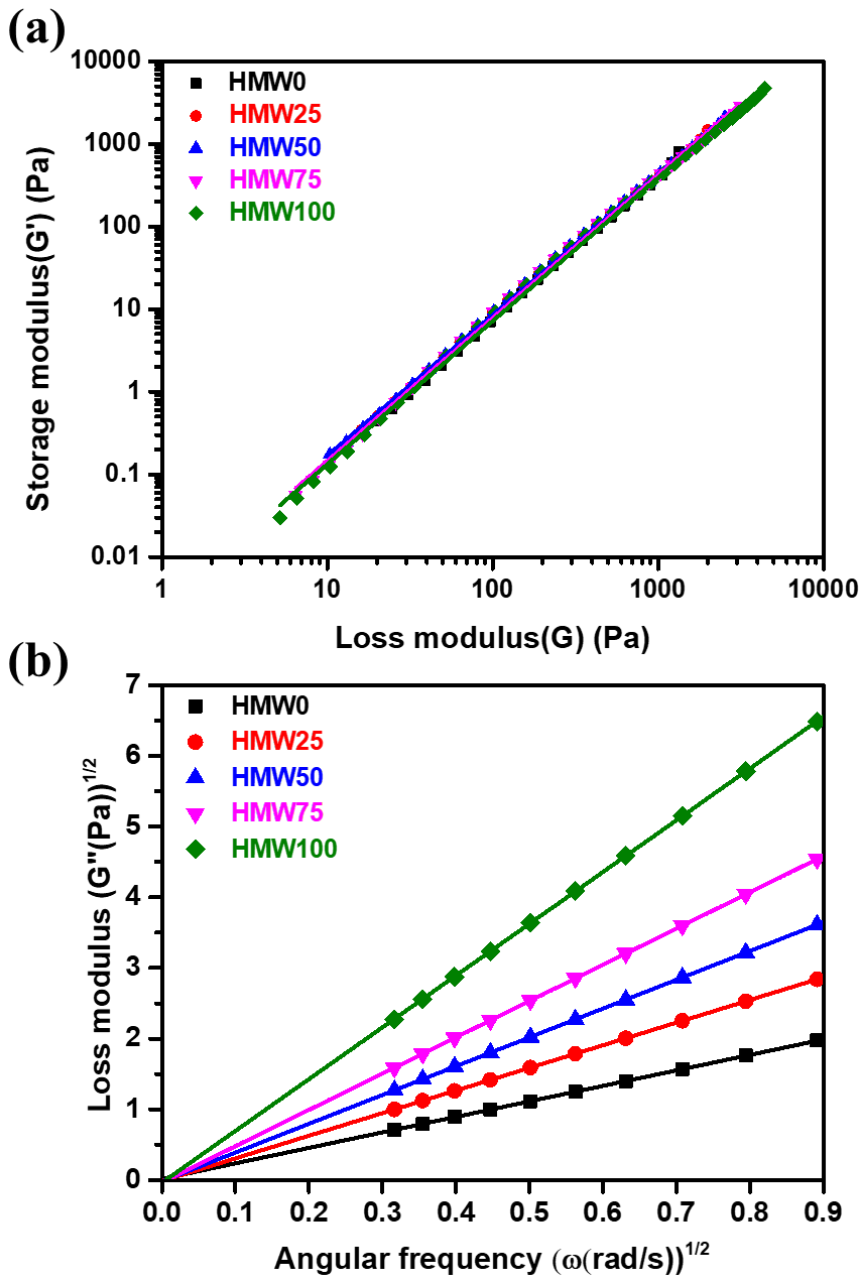

Figure 5-2. Rheological behavior in dope solutions. (a) Han plots, and (b) Casson plots of bimodal MWD PAN dope solutions (HMW0, HMW25, HMW50, HMW75 and HMW100).

The viscosities of A-bimodal MWD PAN dope solutions (A-HMW0, A-HMW25, A-HMW50, A-HMW75 and A-HMW100) were measured and presented in Figure 5-3. All of the bimodal MWD PAN dope solutions exhibited the expected rheological behavior of PAN solution. At a shear rate of 1 (1/s), the viscosities were measured as 7.91, 19.24, 29.10, 43.77, and 70.85 Pa·s for A-HMW0, A-HMW25, A-HMW50, A-HMW75, and A-HMW100, respectively. Viscosity decreased and spinnability increased of A-bimodal MWD PAN dope solutions due to A-LMW.

The viscosities of B-bimodal MWD PAN dope solutions (B-HMW67, B-HMW80, B-HMW90, B-HMW95 and B-HMW100) were measured and presented in Figure 5-4. At a shear rate of 1 (1/s), the viscosities were measured as 35.85, 44.71, 68.54, 111.78, and 171.56 Pa·s for B-HMW67, B-HMW80, B-HMW90, B-HMW95 and B-HMW100, respectively. The B-bimodal MWD PAN exhibits a significant difference in molecular weight between B-LMW and B-HMW. As a result, even a small addition of B-LMW significantly reduces the viscosity and greatly enhances the spinnability.

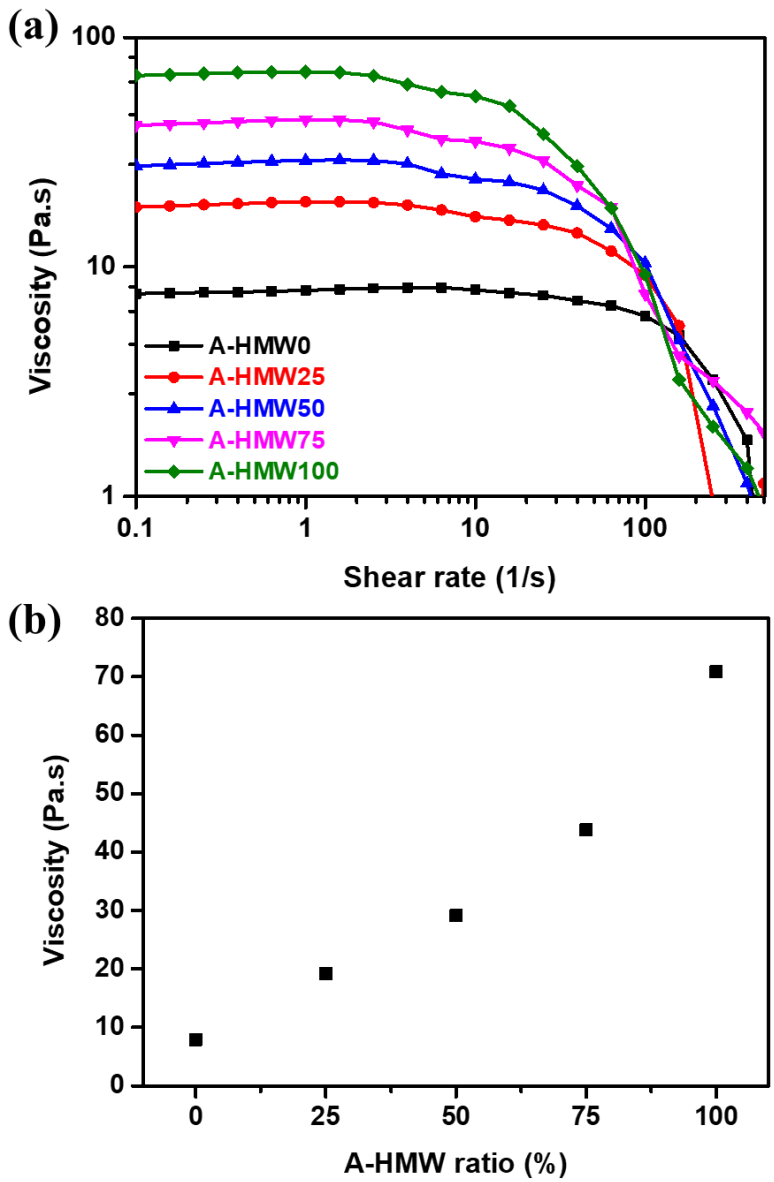

Figure 5-3. Rheological behavior of A-bimodal MWD PAN (A-HMW0, A-HMW25, A-HMW50, A-HMW75 and A-HMW100) in dope solution. (a) dynamic viscosity curves and (b) viscosity of bimodal PAN dope solution at shear rate is 1 (1/s).

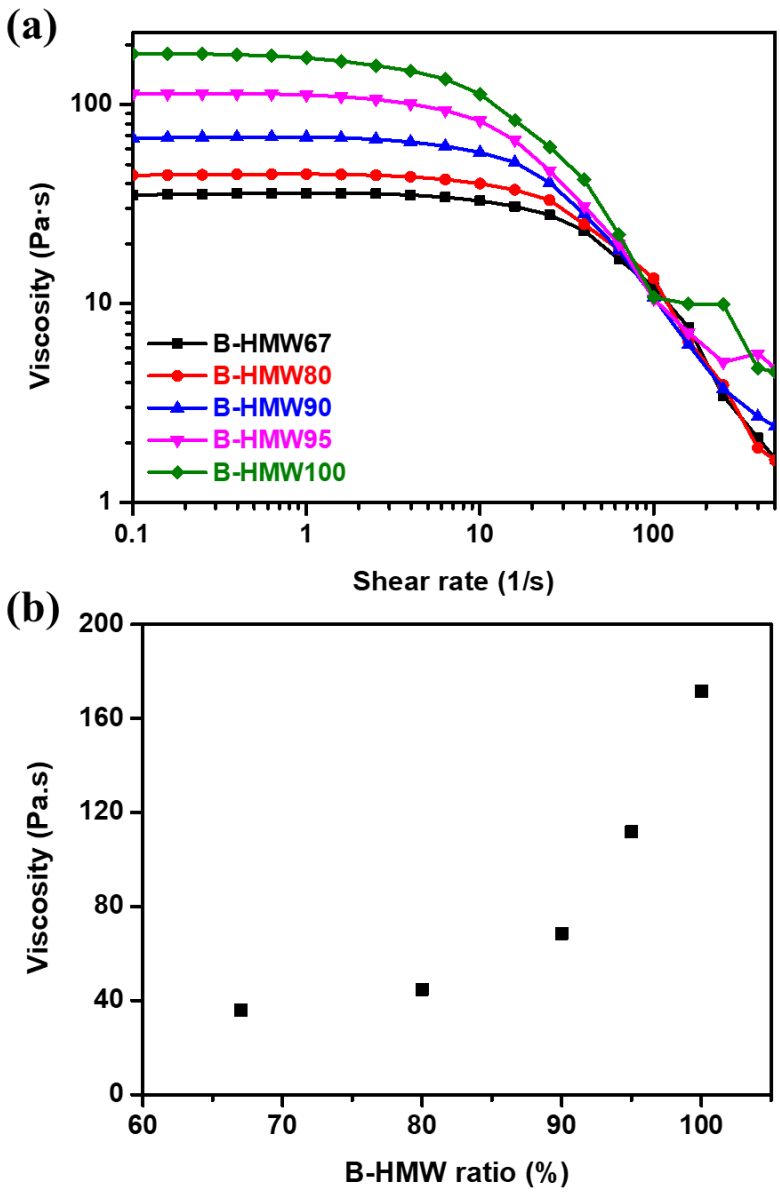

Figure 5-4. Rheological behavior of B-bimodal MWD PAN (B-HMW0, B-HMW25, B-HMW50, B-HMW75 and B-HMW100) in dope solution. (a) dynamic viscosity curves and (b) viscosity of bimodal PAN dope solution at shear rate is 1 (1/s).

5.2.3. The effect of MWD on properties of PAN fiber

The SEM images in Figure 5-5 depict the surface morphology of PAN fibers prepared from various bimodal MWD PAN dope solutions, namely HMW0, HMW25, HMW50, HMW75, and HMW100. A comparison between unimodal MWD PAN fibers (Figure 5-5 (a), (e)) and bimodal MWD PAN fibers (Figure 5-5 (c), (d)) revealed a higher occurrence of wrinkles in the latter. is observation suggests that the diffusion rate in the coagulation bath differs between unimodal and bimodal MWD PAN dope solutions [92]. The presence of LMW and HMW blends alters the diffusion rate, resulting in the formation of wrinkles. So, in this chapter, the tensile strength of PAN fibers was calculated using linear density instead of cross-sectional area to enable a precise comparison of the mechanical properties among the PAN fibers.

The chemical composition of the fibers was analyzed using FT-IR spectroscopy (Figure 5-6). Acrylonitrile peak is CH_2 vibrations (2930 and 2870 cm^{-1}, respectively), C≡N (2242 cm^{-1}), and CH_2 deformation (1452 cm^{-1}) and MA peak is C=O stretching (1732 cm^{-1}), CH_3-O deformation (1387 cm^{-1}), and C−O stretching (1253 and 1093 cm^{-1}) [84, 85]. The amide peak (1666 cm^{-1} indicated the presence of residual solvent (DMF) in the PAN fibers [86]. An increase in the HMW ratio resulted in a larger DMF peak, suggesting stronger interactions between HMW and the solvent, leading to a decrease in the diffusion rate of the solvent in the coagulation bath.

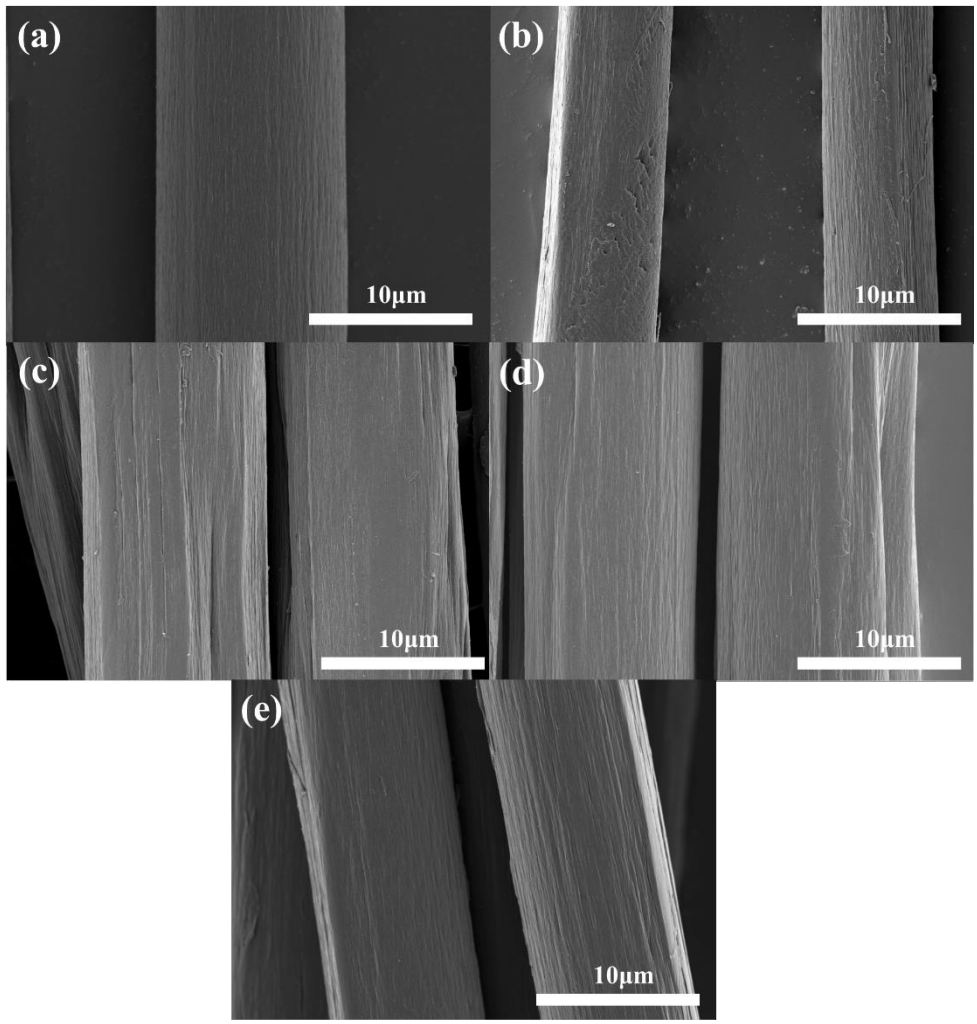

Figure 5-5. Scanning electron microscopy(SEM) images of surface structures of bimodal MWD PAN fibers. (a) HMW0, (b) HMW25 (c) HMW50, (d) H MW75 and (e) HMW100.

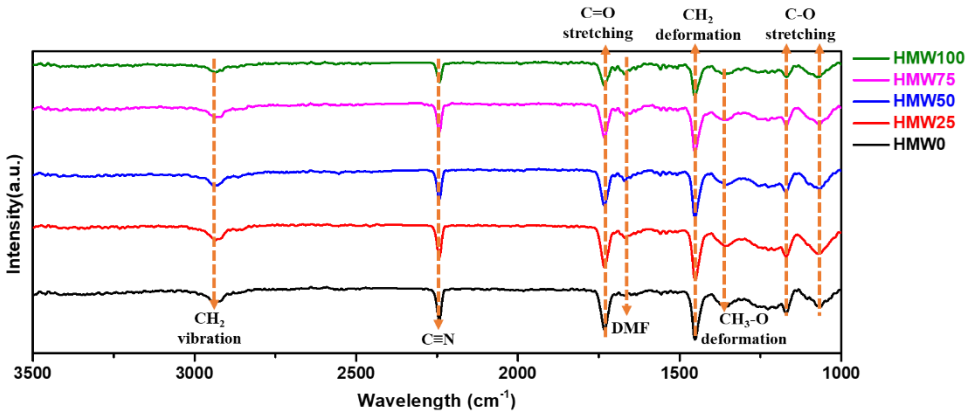

Figure 5-6. Fourier transform infrared spectra(FT-IR) of bimodal MWD PAN fibers (HMW0, HMW25, HMW50, HMW75 and HMW100).

The microstructure of a fiber critically affects its mechanical properties. To investigate the microstructural changes in bimodal MWD PAN fibers, 2D-WAXS and 2D-SAXS were used. The microstructure of the fibers was found to consist of polymer crystals, amorphous regions, and voids [89]. The polymer crystals and preferred orientation along the fiber axes were examined in detail using 2D-WAXD (Figure 5-7 (a)-(e)). Equatorially extracted one-dimensional WAXD curves showed two peaks, with a strong peak at 2θ = 17° assigned to the (100) direction of the crystal, and a weaker peak at 2θ = 27° assigned to the (110) direction of the PAN crystal [95] (Figure 5-7 (e)). The crystallinity of the fibers was calculated using Hinrichsen's method in Chapter 2 [96].

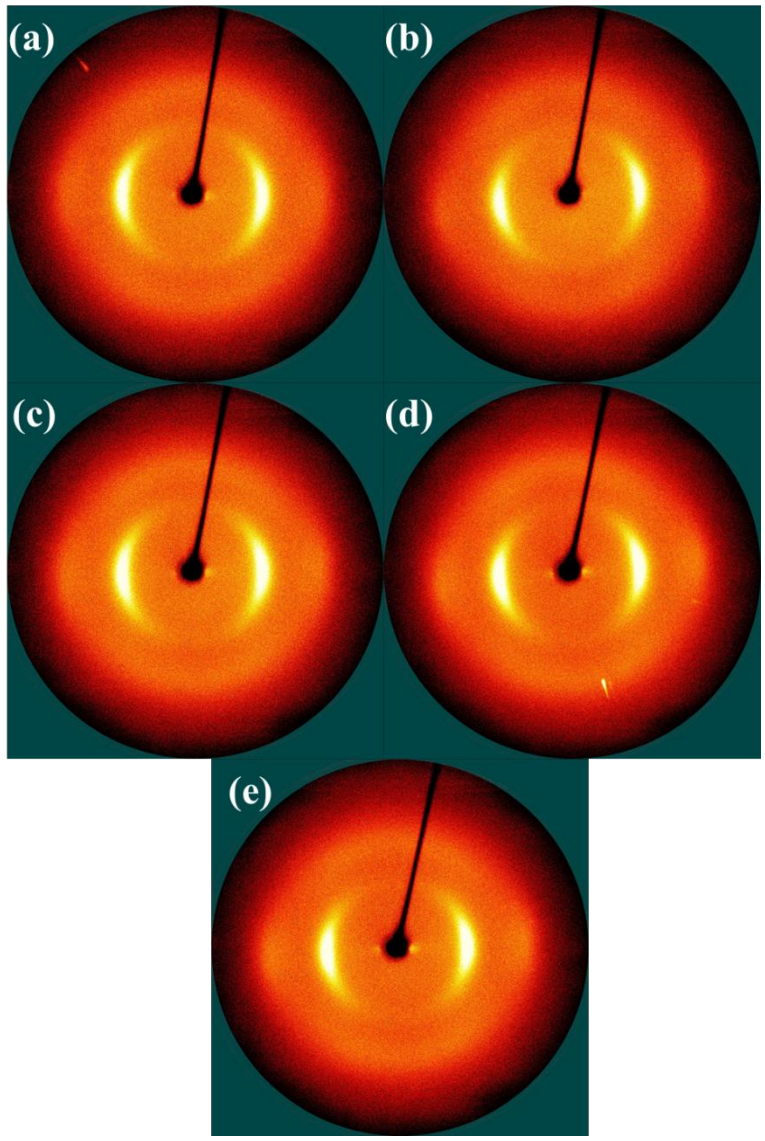
(a)
(b)
(c)
(d)
(e)

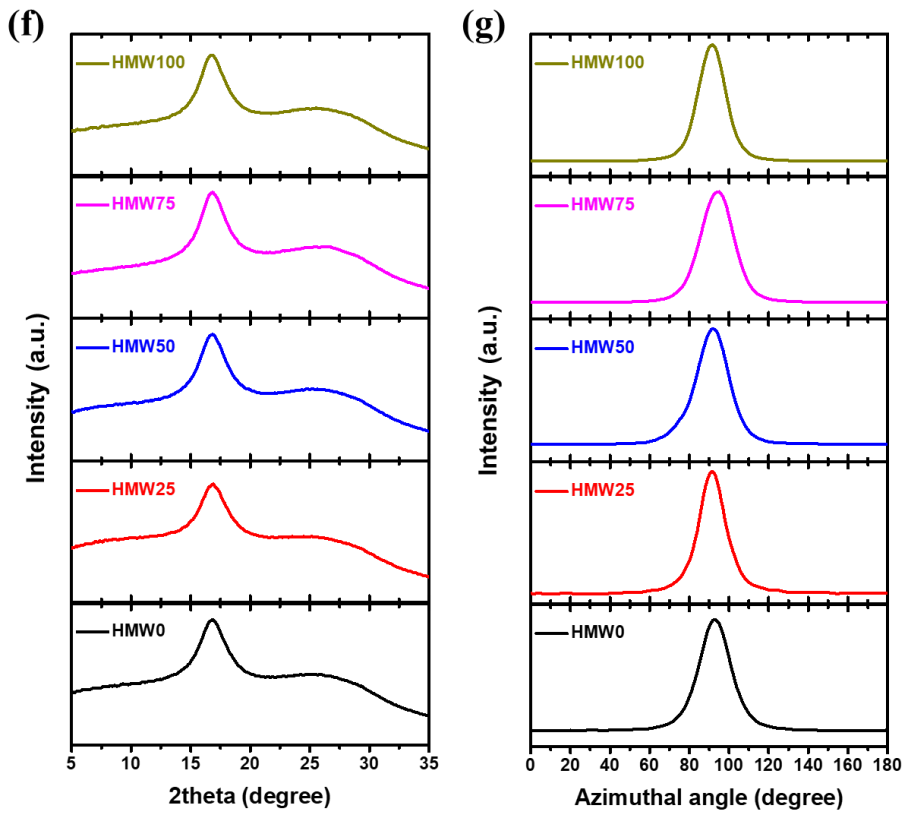

Figure 5-7. Microstructural characterizations of the bimodal molecular weight PAN fibers. Two-dimensional wide-angle X-ray diffraction (2D-WAXD) images of (a) HMW0, (b) HMW25, (c) HMW50, (d) HMW75 and (e) HMW100. (f) Equatorially extracted one-dimensional WAXD curves and (g) azimuthal scans at $2\theta = 17°$.

The calculated crystallinity HMW0, HMW25, HMW50, HMW75 and HMW100 were 53.89, 54.85, 55.90, 58.09 and 56.85%, respectively (Figure 5-8 (a)). The HMW75 has higher crystallinity than other fibers. The calculated crystal size HMW0, HMW25, HMW50, HMW75 and HMW100 were 30.54, 31.70, 31.40, 33.45 and 32.57 Å, respectively (Figure 5-8 (b)). Similarly, HMW75 exhibited the largest crystal size among the samples. The preferred orientations of fibers were calculated from peak integrations of the azimuthal scans at $2\theta = 17°$ (Figure 5-7 (g)). The calculated crystal size HMW0, HMW25, HMW50, HMW75 and HMW100 were 72.89, 76.43, 74.27, 77.50 and 78.68%, respectively (Figure 5-8 (c)). As the HMW ratio increased, the degree of preferred orientation also increased.

HMW75 fibers exhibited the highest crystallinity and crystal size. The formation of crystals in PAN fibers follows a nucleation growth mechanism, resulting in a lamellar and shish kebab structure [151, 152]. The shorter chain length decreased entanglement density and increased the nucleation rate and growth rate [148, 153]. As a result, PAN fibers containing both LMW and HMW, such as HMW75, show increased crystallinity and crystal size compared to HMW100. This phenomenon can be attributed to the LMW acting as nuclei, facilitating the formation of crystals within the fiber. Furthermore, in MWD PE, the addition of a small amount of HMW along with LMW has been observed to make HMW act as an effective nucleating agent. This is attributed to the faster solidification rate of HMW within the fiber [154, 155]. Likewise, with increasing PAN molecular weight, gelation occurs even with a smaller quantity of non-solvent addition. This implies that the coagulation bath

enables solidification even through minimal diffusion of non-solvent. The presence of HMW accelerates the initiation of coagulation in the dope solution, and the rapid nucleation and growth rates of LMW contribute to higher crystallinity in HMW25 compared to HMW0. These observations indicate that bimodal MWD PAN fibers have the potential to enhance their crystalline structure, thereby improving their strength.

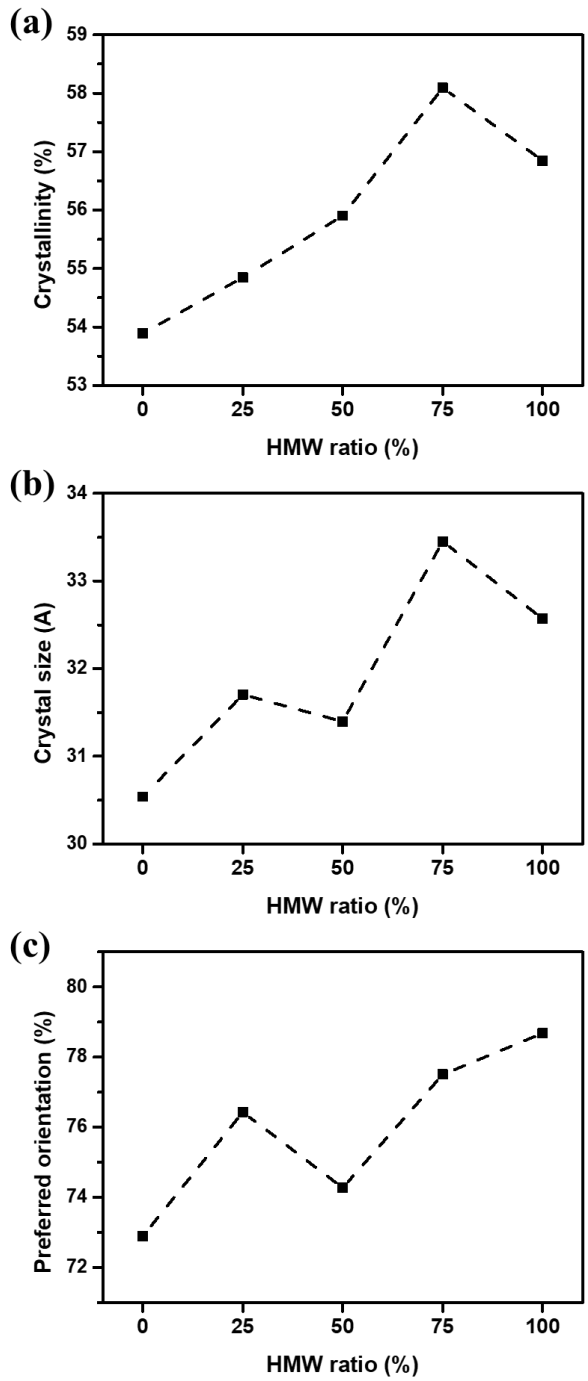

Figure 5-8. (a) Crystallinity, (b) crystal size and (c) preferred orientation of bimodal MWD PAN fibers (HMW0, HMW25, HMW50, HMW75 and HMW100).

The void structure of the HMW0, HMW25, HMW50, HMW75 and HNMW100 fibers was measured using 2D-SAXS (Figure 5-9). The void angle was calculated as the square root of the slope, and the void length was calculated as the square root of the y-intercept through linear fitting of s^2 and $s^2 B_{obs}^2$ calculated by ruland's streak method (Figure 5-10 (a)). The calculated void length HMW0, HMW25, HMW50, HMW75 and HMW100 were 269.81, 327.77, 285.33, 270.59 and 269.05 nm, respectively (Figure 5-10 (b)). And, the calculated void angle HMW0, HMW25, HMW50, HMW75 and HMW100 were 19.87, 17.01, 20.37, 20.22 and 16.81°, respectively (Figure 5-10 (c)). Notably, the bimodal MWD PAN fibers (HMW25, HMW50, HMW75) exhibited larger void lengths compared to the unimodal MWD fibers (HMW0 and HMW100), with HMW25 showing the longest void length. When the polymer concentration exceeds the critical concentration, polymer lean phase (void) nucleation and growth occur [156]. Since the critical concentration of the dope solution is approximately 5%, void nucleation and growth take place. As a result, the voids continue to enlarge until the coagulation process of the dope solution is completed. However, in the case of bimodal MWD PAN fibers, the presence of HMW accelerates the onset of the coagulation process. This leads to an increase in the growth time of the voids. Consequently, bimodal MWD PAN fibers exhibit larger voids compared to the unimodal MWD fibers.

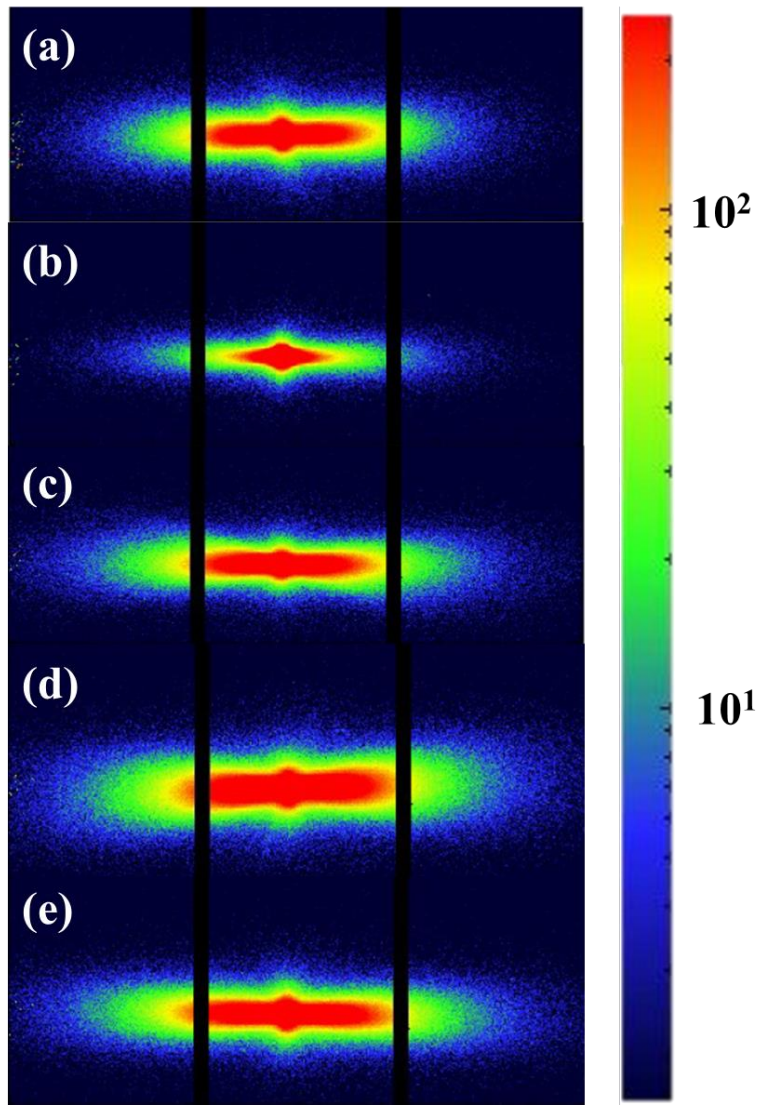

Figure 5-9. Two-dimensional small-angle X-ray scattering (2D-SAXS) images of (a) HMW0, (b) HMW25, (c) HMW50, (d) HMW75 and (e) HMW100 fibers

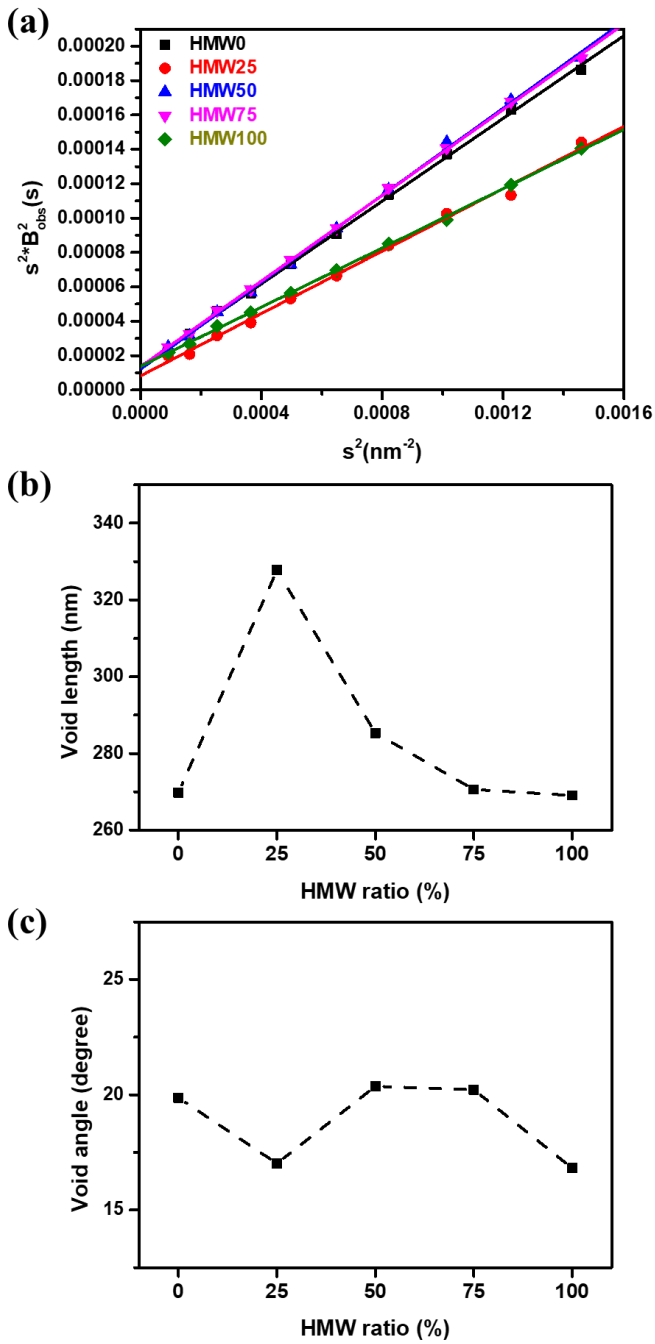

Figure 5-10. Void structure characterizations of the fibers. (a) Ruland's linea r fittings and (b) void length and (c) angle of bimodal MWD PAN fibers (HMW0, HMW25, HMW50, HMW75 and HMW100).

The mechanical properties of bimodal MWD PAN fibers were evaluated by measuring the single-filament properties (Figure 5-11). The specific strength of HMW0, HMW25, HMW50, HMW75 and HMW100 were 4.20 ± 0.16, 4.81 ± 0.23, 4.78 ± 0.15, 5.09 ± 0.17 and 4.80 ± 0.17 g/den, respectively. Generally, an increase in the HMW ratio resulted in an overall enhancement in the tensile strength, attributed to the increased polymer chain entanglement. Notably, the bimodal MWD PAN fibers exhibited higher tensile strength values compared to those predicted by the rule of mixture for unimodal MWD PAN fibers. In particular, HMW75 demonstrated a higher tensile strength than HMW100. This can be attributed to the increased nucleation rate induced by LMW during the coagulation bath, resulting in increased crystallinity and crystal size.

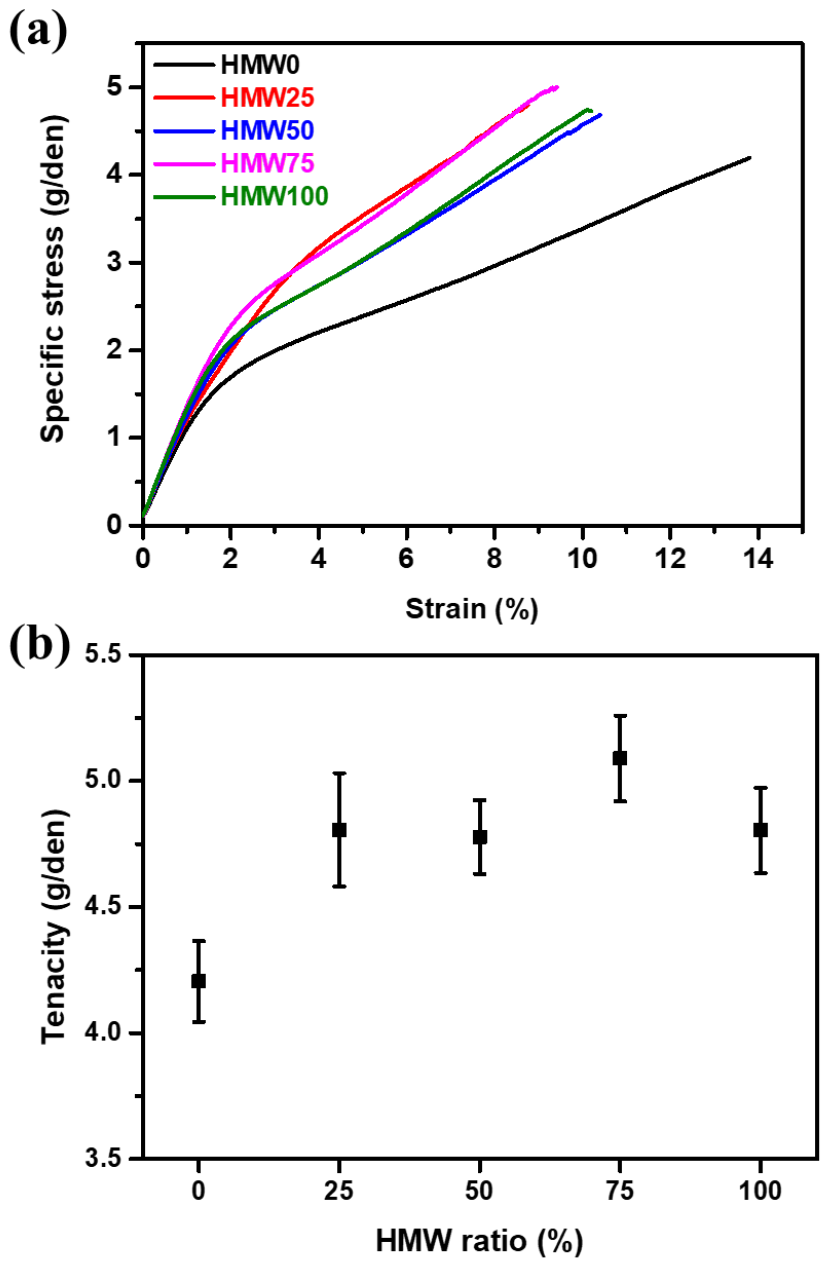

Figure 5-11. Mechanical properties of the (a) specific stress−strain curves (b) specific strength comparison of bimodal MWD PAN fibers (HMW0, HMW 25, HMW50, HMW75 and HMW100).

The crystallographic structures of the A-bimodal MWD PAN fibers (A-HMW0, A-HMW25, A-HMW50, A-HMW75 and A-HMW100) were analyzed using WAXD, as depicted in Figure 5-12. The 2D WAXD patterns in Figure 5-12 (a)-(e) indicate a preferred orientation of the PAN copolymer molecules along the fiber axes. The equatorially extracted one-dimensional WAXD curves in Figure 5-12 (f) show prominent peaks at approximately $2\theta = 17°$ (strong) and 30° (weak), corresponding to the (100) and (110) directions of the PAN molecules, respectively [133]. The calculated crystallinity A-HMW0, A-HMW25, A-HMW50, A-HMW75 and A-HMW100 fibers were 60.22, 60.34, 60.50, 60.18 and 57.42%, respectively (Figure 5-13 (a)). The A-HMW0, A-HMW25, A-HMW50, and A-HMW75 fibers exhibit similar crystallinity levels, which are higher than that of A-HMW100 fibers. The calculated crystal size A-HMW0, A-HMW25, A-HMW50, A-HMW75 and A-HMW100 fibers were 35.31, 34.59, 33.83, 31.61 and 31.33 Å, respectively (Figure 5-13 (b)). Compared to A-HMW100 fibers, A-LMW containing A-HMW75 fibers exhibits higher crystallinity and crystal size. This suggests that A-HMW75 fibers are likely to have the highest strength among the samples.

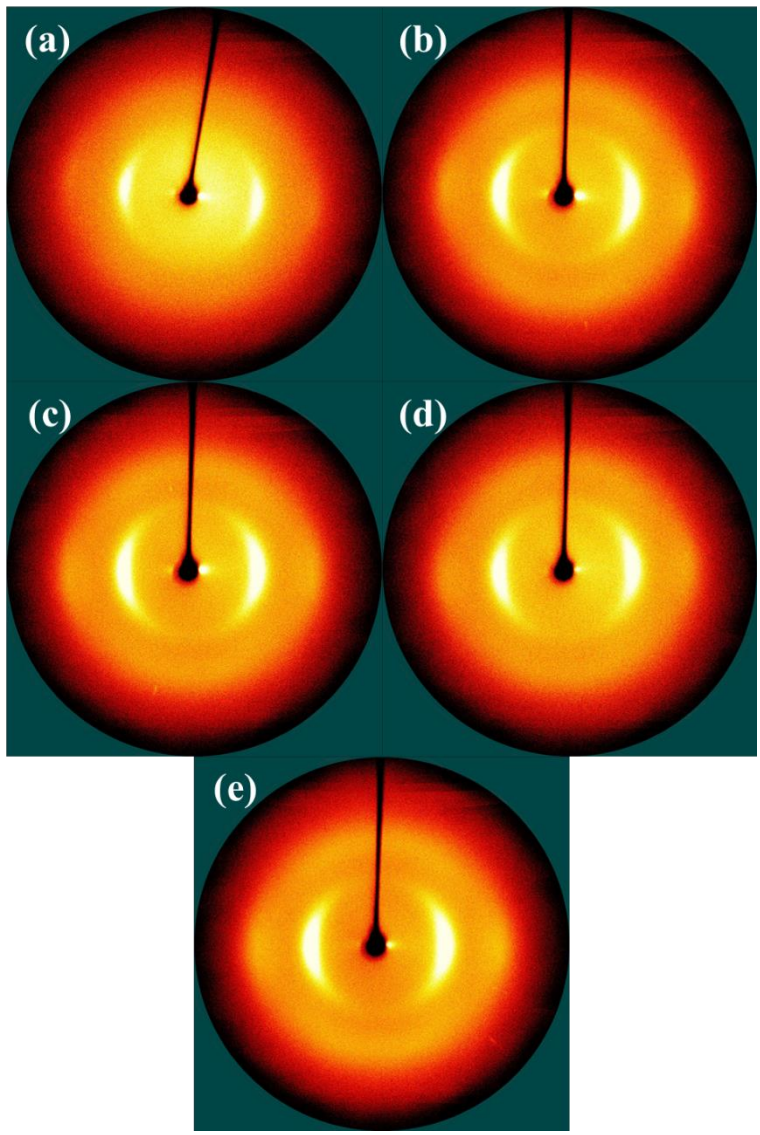
(a)
(b)
(c)
(d)
(e)

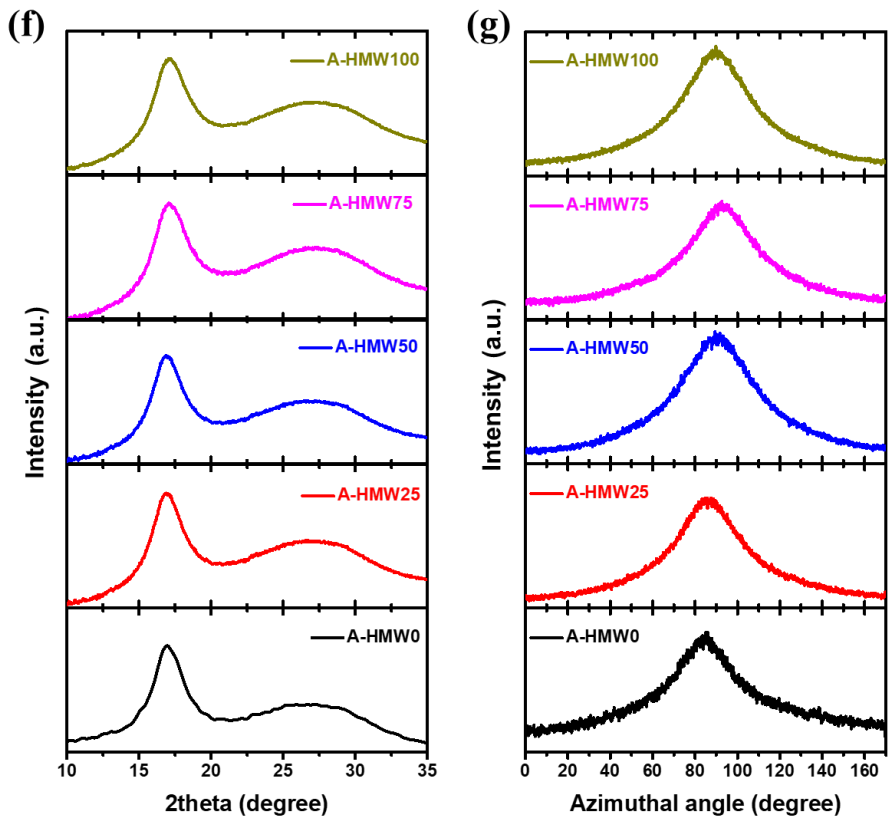

Figure 5-12. Microstructural characterizations of the A-bimodal MWD PAN fibers. Two-dimensional wide-angle X-ray diffraction (2D-WAXD) images of (a) A-HMW0, (b) A-HMW25, (c) A-HMW50, (d) A-HMW75 and (e) A-HM W100. (f) Equatorially extracted one-dimensional WAXD curves and (g) azi muthal scans at 2θ = 17°.

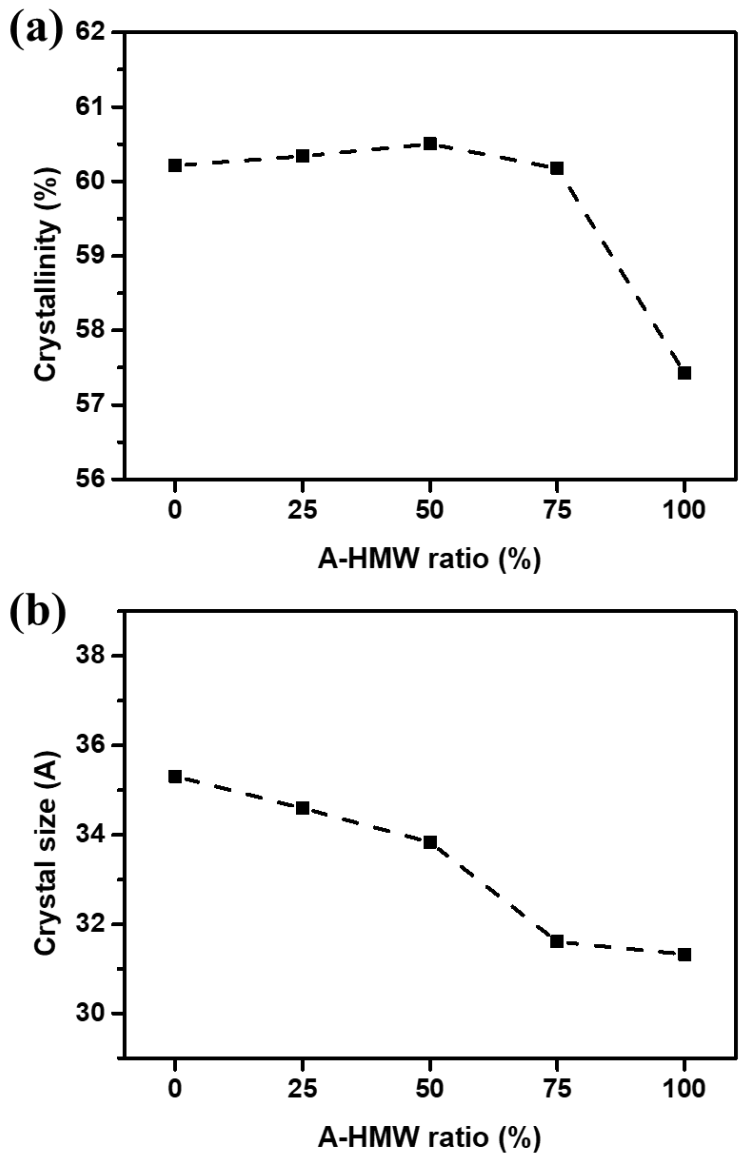

Figure 5-13. (a) Crystallinity and (b) crystal size of A-bimodal MWDPAN fibers (A-HMW0, A-HMW25, A-HMW50, A-HMW75 and A-HMW100).

The crystallographic structures of the B-bimodal MWD PAN fibers (B-HMW67, B-HMW80, B-HMW90, B-HMW95 and B-HMW100) were analyzed using WAXD, as depicted in Figure 5-14. The 2D WAXD patterns in Figure 5-14 (a)-(e) indicate a preferred orientation of the PAN copolymer molecules along the fiber axes. The equatorially extracted one-dimensional WAXD curves in Figure 5-14 (f) show prominent peaks at approximately $2\theta = 17°$ (strong) and 30° (weak), corresponding to the (100) and (110) directions of the PAN molecules, respectively [133]. The calculated crystallinity B-HMW67, B-HMW80, B-HMW90, B-HMW95 and B-HMW100 fibers were 66.31, 66.77, 65.02, 64.11 and 59.05%, respectively (Figure 5-15 (a)). The B-HMW67, B-HMW80, B-HMW90, and B-HMW95 fibers exhibit similar crystallinity levels, which are higher than that of B-HMW100 fibers. The calculated crystal B-HMW67, B-HMW80, B-HMW90, B-HMW95 and B-HMW100 fibers were 35.96, 32.97, 33.77, 36.94 and 32.96 Å, respectively (Figure 5-15 (b)). Compared to B-HMW100 fibers, B-LMW containing B-bimodal MWD PAN fibers exhibits higher crystallinity. This suggests that B-bimodal MWD fibers can have the higher strength than B-HMW100 fibers.

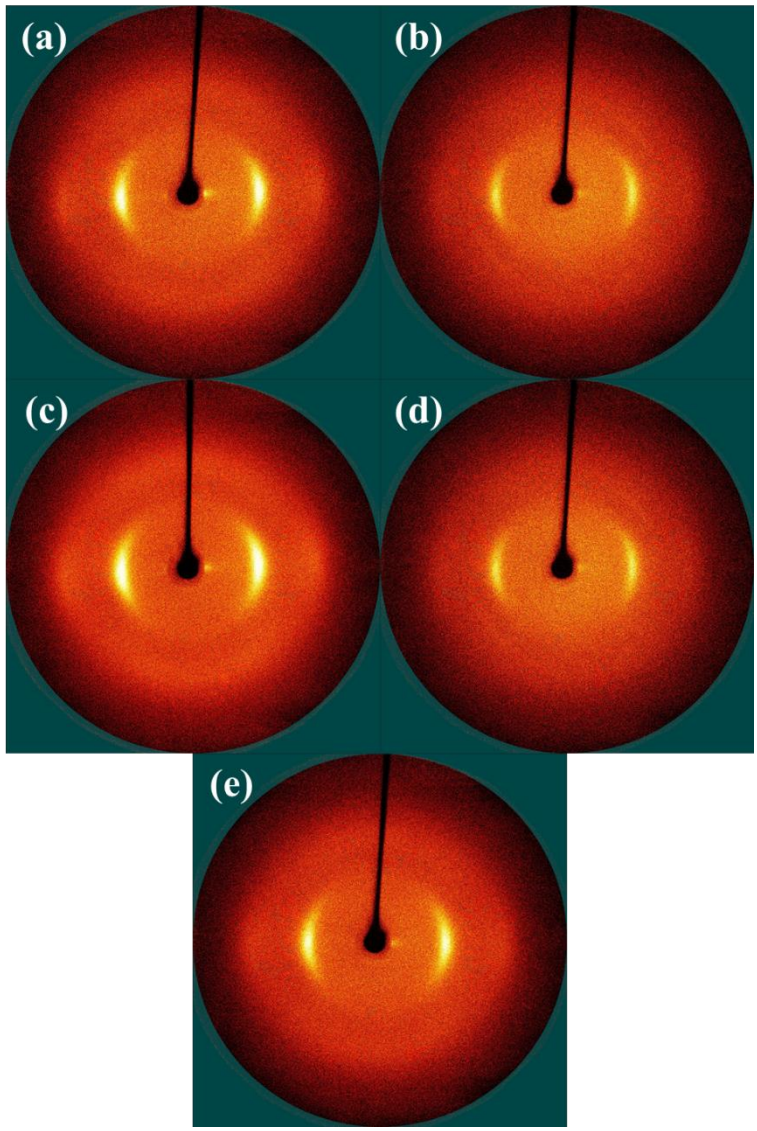
(a)
(b)
(c)
(d)
(e)

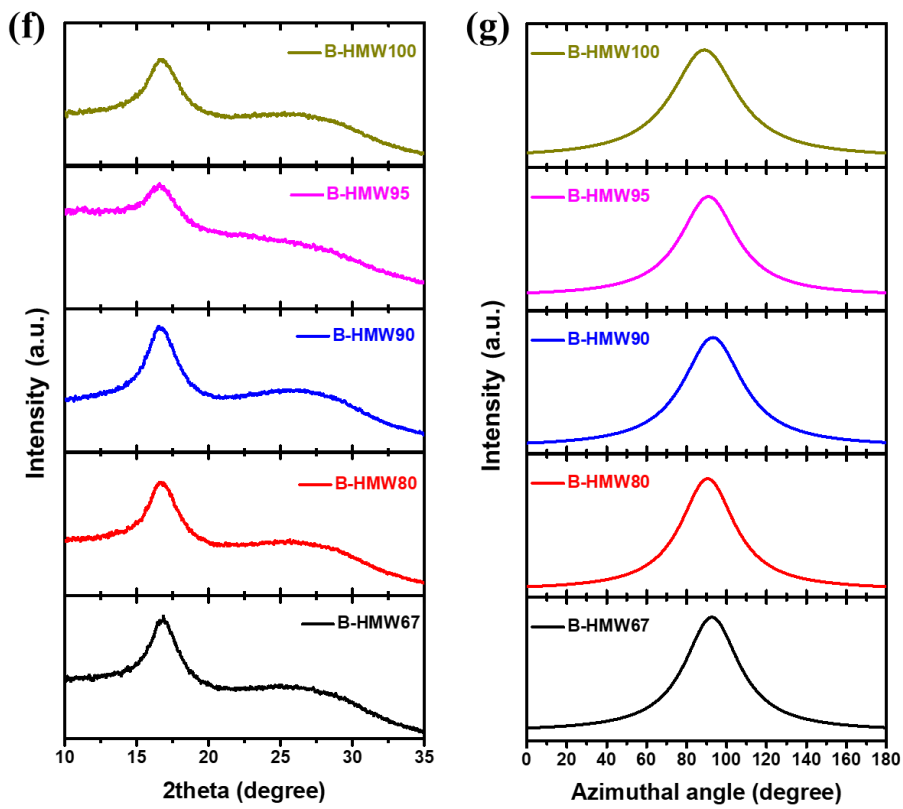

Figure 5-14. Microstructural characterizations of the B-bimodal MWD PAN fibers. Two-dimensional wide-angle X-ray diffraction (2D-WAXD) images of (a) B-HMW67, (b) B-HMW80, (c) B-HMW90, (d) B-HMW95 and (e) B-H MW100. (f) Equatorially extracted one-dimensional WAXD curves and (g) a zimuthal scans at $2\theta = 17°$.

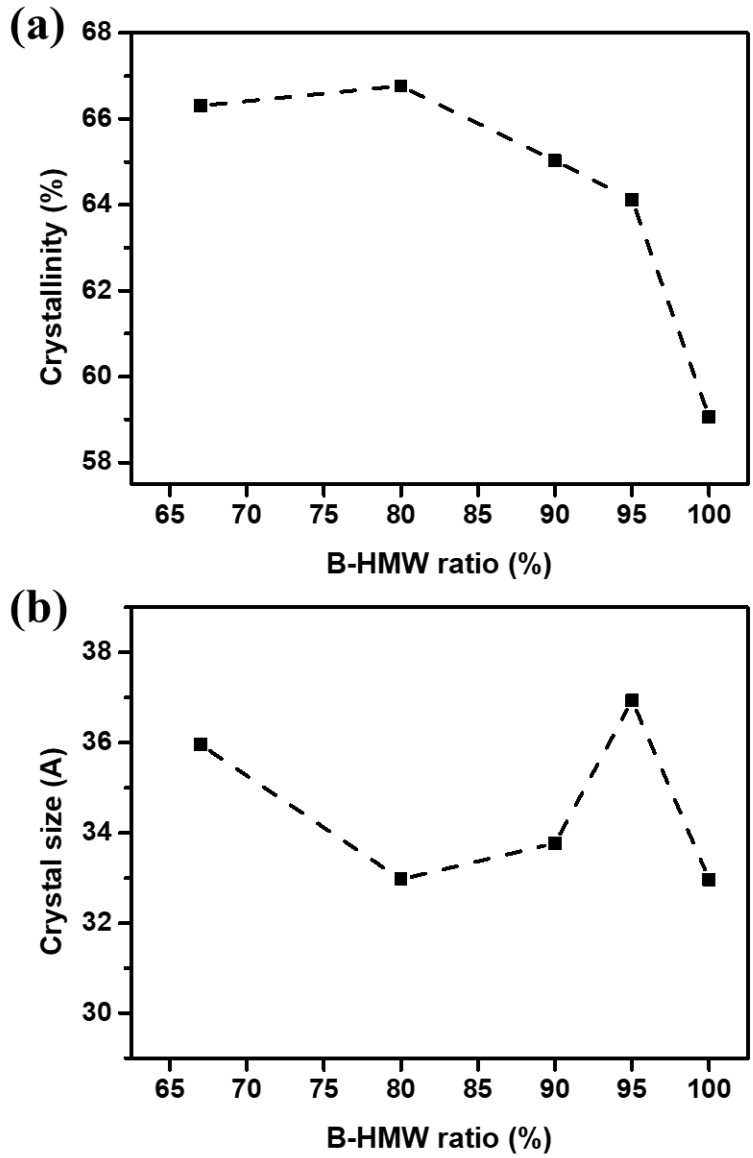

Figure 5-15. (a) Crystallinity and (b) crystal size of B-bimodal MWD PAN fibers (B-HMW67, B-HMW80, B-HMW90, B-HMW95 and B-HMW100).

The mechanical properties of A-bimodal MWD PAN fibers and B-bimodal MWD PAN fibers were assessed by measuring their single-filament properties (Figure 5-16). The specific strength of A-HMW0, A-HMW25, A-HMW50, A-HMW75 and A-HMW100 fibers were 2.84 ± 0.23, 3.19 ± 0.21, 3.64 ± 0.21, 5.43 ± 0.28 and 4.96 ± 0.18 g/den, respectively (Figure 5-16 (a)). Generally, an increase in the A-HMW ratio led to an overall enhancement in the tensile strength, attributed to the increased polymer chain entanglement Notably, A-HMW75 fibers exhibited the highest specific strength, following the same trend observed in the previous bimodal MWD PAN fibers. The specific strength of B-HMW67, B-HMW80, B-HMW90, B-HMW95 and B-HMW100 fibers were 3.50 ± 0.14, 3.87 ± 0.22, 3.96 ± 0.28, 3.96 ± 0.21 and 4.25 ± 0.28 g/den, respectively (Figure 5-16 (b)). In contrast to the previous two bimodal MWD PAN fibers, B-HMW100 fibers displayed the highest specific strength. In cases where there is a substantial difference in molecular weight, the addition of a small amount of low molecular weight can have a profound effect in reducing viscosity and consequently enhancing spinnability. However, this decrease in viscosity also results in a decrease in chain entanglement, which counteracts the improvement in mechanical properties associated with microstructure enhancement. Therefore, bimodal MWD PAN fibers fabricated by blending appropriate molecular weight ratios of low and high molecular weight PAN exhibit not only increased spinnability due to reduced viscosity but also improved mechanical properties.

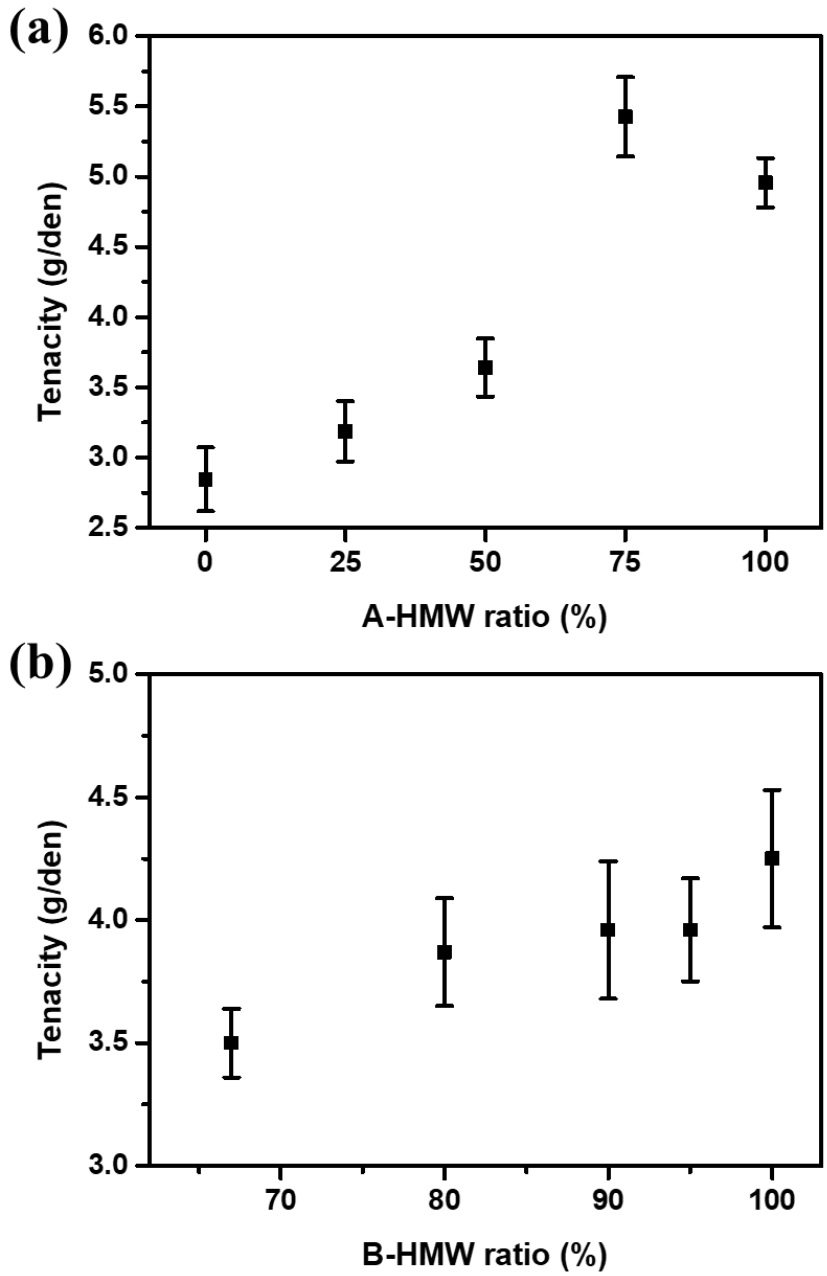

Figure 5-16. Specific strength of the (a) A-bimodal MWD PAN fibers (A-HMW0, A-HMW25, A-HMW50, A-HMW75 and A-HMW100) and (b) B-bimodal MWD PAN fibers (B-HMW67, B-HMW80, B-HMW90, B-HMW95 and B-HMW100).

5.3. Summary

The influence of bimodal MWD PAN on spinnability and mechanical properties was investigated. The addition of a low molecular weight PAN in the bimodal MWD PAN dope solution resulted in decreased viscosity, leading to increased spinnability. Solution homogeneity and intermolecular chain interaction remained unchanged. Through microstructure improvement, HMW75 fibers exhibited higher strength compared to HMW100 fibers. During the coagulation process, the rapid nucleation rate and growth rate of the low molecular weight PAN, combined with the fast solidification initiation of the high molecular weight PAN, led to an increase in crystallinity and crystal size. Consequently, the strength of PAN fibers was enhanced. These findings emphasize the simultaneous improvement in spinnability and mechanical properties achieved through the production of bimodal MWD PAN fibers.

Chapter 6. Concluding remarks

The objective of this thesis was to develop a wet-spinning process for manufacturing high-strength PAN fibers and improve the spinnability of the wet-spinning process. The electrochemical wet-spinning process was introduced for PAN fiber production, and a suitable PAN design was developed. To prevent damage to PAN during the applied electrical potential, only the comonomer reacted while PAN remained intact. Methyl acrylate (MA), a neutral comonomer, was utilized to enhance spinnability. Furthermore, cations (Na^+) were attached to the PAN chain ends to facilitate ionization of PAN during electrochemical wet-spinning. The designed cations within PAN (NaPAN) would separate the cations upon applied electrical potential, leading to ionization by reacting with the comonomer. The cations within PAN resulted in increased diffusion rate of the non-solvent in the coagulation bath, reducing void length by 17.6%. As a result, the fiber properties improved by 12.5% through electrochemical wet-spinning.

To ionize cations without PAN (nonPAN) via electrochemical wet-spinning, lithium acetate (LiPAN) was added to the dope solution. The presence of Li^+ reduced the diffusion rate of the solvent and increased the diffusion rate of the non-solvent in the coagulation bath. Consequently, both void length and void angle decreased. Through a comparison of the mechanical properties, it was confirmed that optimized salt concentration of 1 wt% was determined. The electrochemical wet-spun fibers produced with 1 wt% lithium acetate exhibited a 16.1% increase in failure strength.

Water (non-solvent) had a significant impact on PAN fibers. To investigate its influence, moisture was uniformly deposited on PAN after completely removing moisture from PAN. Fibers manufactured via conventional wet-spinning with 0.5 wt% moisture content (GPAN0.5) exhibited minimized voids. For fibers produced through electrochemical wet-spinning, the optimal moisture content for minimizing voids was 1.0 wt% (EPAN1.0). Both GPAN0.5 and EPAN1.0 demonstrated the highest strength due to minimized voids. Ionization of the comonomer via electrical potential applied enhanced molecular interactions by absorbing more water.

To enhance spinnability and mechanical properties, a bimodal molecular weight distribution of PAN was designed. Dope solutions of bimodal molecular weight distribution PAN exhibited exponential viscosity reduction as LMW increased, thereby improving spinnability. During the coagulation process, LMW exhibited rapid nucleation and growth rates, while HMW reduced the starting concentration of the non-solvent, resulting in increased crystallinity and crystal size for HMW75 compared to HMW100. Consequently, HMW75 had 6.04% higher the failure strength than HMW100. A-bimodal molecular weight distribution PAN with different molecular weight ratios also showed a 9.48% increase in failure strength at A-HMW75. However, B-bimodal molecular weight distribution PAN with a large difference in molecular weight demonstrated an increase in mechanical properties proportional to the B-HMW content. In conclusion, PAN fibers with smaller molecular weight differences (<1:2) exhibited enhanced spinnability and improved mechanical properties in an optimized bimodal molecular weight distribution.

Reference

1. Geller, B., *Status and prospects for development of polyacrylonitrile fibre production. A review.* Fibre Chemistry, 2002. **34**(3): p. 151-161.
2. Pan, W., et al., *Electrical and structural analysis of conductive polyaniline/polyacrylonitrile composites.* European Polymer Journal, 2005. **41**(9): p. 2127-2133.
3. Adegbola, T.A., O. Agboola, and O.S.I. Fayomi, *Review of polyacrylonitrile blends and application in manufacturing technology: recycling and environmental impact.* Results in Engineering, 2020. **7**.
4. Kricheldorf, H.R., *Handbook of polymer synthesis*. Vol. 24. 1991: CRC press.
5. Hou, C., et al., *High-molecular-weight polyacrylonitrile by atom transfer radical polymerization.* Journal of Applied Polymer Science, 2006. **100**(4): p. 3372-3376.
6. Zhang, Z. and M. Han, *One-step preparation of size-selected and well-dispersed silver nanocrystals in polyacrylonitrile by simultaneous reduction and polymerization.* Journal of Materials Chemistry, 2003. **13**(4): p. 641-643.
7. Matyjaszewski, K., et al., *Synthesis of well-defined polyacrylonitrile by atom transfer radical polymerization.* Macromolecules, 1997. **30**(20): p. 6398-6400.
8. Novoselova, A.V., V.V. Shamanin, and L.V. Vinogradova, *Synthesis of ultra-high-molecular-weight polyacrylonitrile by anionic polymerization.* Polymer Science Series B, 2009. **51**(7-8): p. 205-211.
9. Nakano, Y., K. Hisatani, and K. Kamide, *Synthesis of highly isotactic (mm > 0.70) polyacrylonitrile by anionic polymerization using diethylberyllium as a main initiator.* Polymer International, 1994. **35**(2): p. 207-213.
10. Fu, Z., et al., *Structure evolution and mechanism of polyacrylonitrile and related copolymers during the stabilization.* Journal of Materials Science, 2014. **49**(7): p. 2864-2874.
11. Hou, C., et al., *Kinetics of diffusion in polyacrylonitrile fiber formation.* Journal of Applied Polymer Science, 2005. **96**(5): p. 1529-1533.

12. Morris, E.A., et al., *Synthesis, spinning, and properties of very high molecular weight poly(acrylonitrile-co-methyl acrylate) for high performance precursors for carbon fiber.* Polymer, 2014. **55**(25): p. 6471-6482.
13. Tsai, J.-S. and C.-H. Lin, *Effect of comonomer composition on the properties of polyacrylonitrile precursor and resulting carbon fiber.* Journal of Applied Polymer Science, 1991. **43**(4): p. 679-685.
14. Choi, D., H.-S. Kil, and S. Lee, *Fabrication of low-cost carbon fibers using economical precursors and advanced processing technologies.* Carbon, 2019. **142**: p. 610-649.
15. Hou, C. and L. Ying, *Stability of acrylonitrile/methyl vinyl ketone copolymer solutions.* Journal of Applied Polymer Science, 2006. **100**(4): p. 3377-3381.
16. Ju, A., S. Guang, and H. Xu, *Effect of comonomer structure on the stabilization and spinnability of polyacrylonitrile copolymers.* Carbon, 2013. **54**: p. 323-335.
17. Cho, D.W. and S.C. Hong, *Synergistic effect of comonomers on the thermal oxidative stabilization of polyacrylonitrile copolymers for carbon materials.* Polymer Degradation and Stability, 2019. **161**: p. 191-197.
18. Fitzer, E., W. Frohs, and M. Heine, *Optimization of stabilization and carbonization treatment of PAN fibres and structural characterization of the resulting carbon fibres.* Carbon, 1986. **24**(4): p. 387-395.
19. Zhang, H., et al., *Thermal Analysis and Crystal Structure of Poly(Acrylonitrile-Co-Itaconic Acid) Copolymers Synthesized in Water.* Polymers (Basel), 2020. **12**(1).
20. Nguyen-Thai, N.U. and S.C. Hong, *Structural Evolution of Poly(acrylonitrile-co-itaconic acid) during Thermal Oxidative Stabilization for Carbon Materials.* Macromolecules, 2013. **46**(15): p. 5882-5889.
21. Nguyen-Thai, N.U. and S.C. Hong, *Controlled architectures of poly(acrylonitrile-co-itaconic acid) for efficient structural transformation into carbon materials.* Carbon, 2014. **69**: p. 571-581.
22. Gulgunje, P.V., et al., *Low-density and high-modulus carbon fibers from polyacrylonitrile with honeycomb structure.* Carbon, 2015. **95**: p. 710-714.

23. Newcomb, B.A., et al., *Processing, structure, and properties of gel spun PAN and PAN/CNT fibers and gel spun PAN based carbon fibers.* Polymer Engineering & Science, 2015. **55**(11): p. 2603-2614.
24. Skvortsov, I.Y., et al., *Influence of Alkyl Acrylate Nature on Rheological Properties of Polyacrylonitrile Terpolymers Solutions, Spinnability and Mechanical Characteristics of Fibers.* Materials (Basel), 2022. **16**(1).
25. Catta Preta, I., et al., *Thermal behavior of polyacrylonitrile polymers synthesized under different conditions and comonomer compositions.* Journal of Thermal Analysis and Calorimetry, 2007. **87**(3): p. 657-659.
26. Morris, E.A., et al., *High performance carbon fibers from very high molecular weight polyacrylonitrile precursors.* Carbon, 2016. **101**: p. 245-252.
27. Kaur, J., et al., *High molecular weight improves microstructure and mechanical properties of polyacrylonitrile based carbon fibre precursor.* Polymer, 2022. **247**.
28. Rui, G., et al., *A metal-free method for ultra-high molecular weight polyacrylonitrile under dimethyl sulfoxide.* Polymer, 2021. **214**.
29. Cai, J.Y., et al., *Polyacrylonitrile-based precursors and carbon fibers derived from advanced RAFT technology and conventional methods – The 1st comparative study.* Materials Today Communications, 2016. **9**: p. 22-29.
30. Zong, G., et al., *Synthesis of polyacrylonitrile via ARGET ATRP using CCl4 as initiator.* Journal of Applied Polymer Science, 2010. **118**(6): p. 3673-3677.
31. Niu, S., et al., *Synthesis of high molecular weight and narrow molecular weight distribution poly(acrylonitrile) via RAFT polymerization.* Journal of Polymer Science Part A: Polymer Chemistry, 2013. **51**(5): p. 1197-1204.
32. Moskowitz, J.D., et al., *High molecular weight and low dispersity polyacrylonitrile by low temperature RAFT polymerization.* Journal of Polymer Science Part A: Polymer Chemistry, 2016. **54**(4): p. 553-562.
33. Lamson, M., et al., *Synthesis of well-defined polyacrylonitrile by ICARATRP with low concentrations of catalyst.* Journal of Polymer Science Part A: Polymer Chemistry, 2016. **54**(13): p. 1961-1968.
34. Jang, D., et al., *Strategies for the production of PAN-Based carbon fibers*

with high tensile strength. Carbon, 2022. **186**: p. 644-677.

35. Kaur, J., K. Millington, and S. Smith, *Producing high-quality precursor polymer and fibers to achieve theoretical strength in carbon fibers: A review.* Journal of Applied Polymer Science, 2016. **133**(38).
36. Kaur, J., K. Millington, and S. Smith, *Producing high-quality precursor polymer and fibers to achieve theoretical strength in carbon fibers: A review.* Journal of Applied Polymer Science, 2016. **133**(38).
37. Dıaz, J. and L. Rubio, *Developments to manufacture structural aeronautical parts in carbon fibre reinforced thermoplastic materials.* Journal of Materials Processing Technology, 2003. **143-144**: p. 342-346.
38. Yao, S.-S., et al., *Recent advances in carbon-fiber-reinforced thermoplastic composites: A review.* Composites Part B: Engineering, 2018. **142**: p. 241-250.
39. Aamir, M., et al., *Recent advances in drilling of carbon fiber–reinforced polymers for aerospace applications: a review.* The International Journal of Advanced Manufacturing Technology, 2019. **105**(5-6): p. 2289-2308.
40. Rahaman, M.S.A., A.F. Ismail, and A. Mustafa, *A review of heat treatment on polyacrylonitrile fiber.* Polymer Degradation and Stability, 2007. **92**(8): p. 1421-1432.
41. Nunna, S., et al., *Evolution of radial heterogeneity in polyacrylonitrile fibres during thermal stabilization: An overview.* Polymer Degradation and Stability, 2017. **136**: p. 20-30.
42. Bajaj, P. and A.K. Roopanwal, *Thermal Stabilization of Acrylic Precursors for the Production of Carbon Fibers: An Overview.* Journal of Macromolecular Science, Part C: Polymer Reviews, 1997. **37**(1): p. 97-147.
43. Endo, M., *Carbon Fiber*, in *High-Performance and Specialty Fibers: Concepts, Technology and Modern Applications of Man-Made Fibers for the Future*, S. The Society of Fiber and J. Techno, Editors. 2016, Springer Japan: Tokyo. p. 327-342.
44. Wiles, K.B., *Determination of reactivity ratios for acrylonitrile/methyl acrylate radical copolymerization via nonlinear methodologies using real time FTIR*. 2002, Virginia Tech.
45. Kopeć, M., et al., *Polyacrylonitrile-derived nanostructured carbon materials.*

Progress in Polymer Science, 2019. **92**: p. 89-134.

46. Jin, X., et al., *On the structural evolution of textile grade polyacrylonitrile fibers during stabilization and carbonization: Towards the manufacture of low-cost carbon fiber.* Polymer Degradation and Stability, 2021. **186**.
47. Ahn, H., S.Y. Yeo, and B.S. Lee, *Designing Materials and Processes for Strong Polyacrylonitrile Precursor Fibers.* Polymers (Basel), 2021. **13**(17).
48. Gao, Q., et al., *Microfibril alignment induced by stretching fields during the dry-jet wet spinning process: Reinforcement on polyacrylonitrile fiber mechanical properties.* Polymer Testing, 2020. **81**.
49. Gao, Q., et al., *Correlation between fibril structures and mechanical properties of polyacrylonitrile fibers during the dry-jet wet spinning process.* Journal of Applied Polymer Science, 2019. **136**(14).
50. Hao, J., et al., *Effect of coagulation conditions on solvent diffusions and the structures and tensile properties of solution spun polyacrylonitrile fibers.* Journal of Applied Polymer Science, 2017. **134**(5).
51. Zeng, X., et al., *Investigating the jet stretch in the wet spinning of PAN fiber.* Journal of Applied Polymer Science, 2007. **106**(4): p. 2267-2273.
52. Chen, J.C. and I.R. Harrison, *Modification of polyacrylonitrile (PAN) carbon fiber precursor via post-spinning plasticization and stretching in dimethyl formamide (DMF).* Carbon, 2002. **40**(1): p. 25-45.
53. Huang, X., *Fabrication and Properties of Carbon Fibers.* Materials, 2009. **2**(4): p. 2369-2403.
54. Frank, E., et al., *Carbon Fibers: Precursor Systems, Processing, Structure, and Properties.* Angewandte Chemie International Edition, 2014. **53**(21): p. 5262-5298.
55. Al Faruque, M.A., et al., *Impact of the wet spinning parameters on the alpaca-based polyacrylonitrile composite fibers: Morphology and enhanced mechanical properties study.* Journal of Applied Polymer Science, 2020. **137**(41).
56. Dong, X.-G., C.-G. Wang, and C. Juan, *Study on the Coagulation Process of Polyacrylonitrile Nascent Fibers during Wet-spinning.* Polymer Bulletin, 2006. **58**(5-6): p. 1005-1012.
57. Gao, Q., et al., *From Microfibrillar Network to Lamellae during the*

Coagulation Process of Polyacrylonitrile Fiber: Visualization of Intermediate Structure Evolution. Macromolecules, 2020. **53**(19): p. 8663-8673.

58. Yang, H.-S., et al., *Electrochemical wet-spinning process for fabricating strong PAN fibers via an in situ induced plasticizing effect.* Polymer, 2020. **202**: p. 122641.
59. Gao, Q., et al., *Preparation of High-Quality Polyacrylonitrile Precursors for Carbon Fibers Through a High Drawing Ratio in the Coagulation Bath During a Dry-Jet Wet Spinning Process.* Journal of Macromolecular Science, Part B, 2019. **58**(1): p. 128-140.
60. Masson, J., *Acrylic fiber technology and applications*. 1995: CRC Press.
61. Knudsen, J.P., *The Influence of Coagulation Variables on the Structure and Physical Properties of an Acrylic Fiber.* Textile Research Journal, 1963. **33**(1): p. 13-20.
62. Yan-Xiang, W., et al., *Effect of the drawing process on the wet spinning of polyacrylonitrile fibers in a system of dimethyl sulfoxide and water.* Journal of Applied Polymer Science, 2007. **104**(2): p. 1026-1037.
63. I., S.A. and K.V. P., *Influence of drawing speed on some properties of acrylic fibers.* Journal of Applied Polymer Science, 1981. **26**(6): p. 1813-1818.
64. Eom, Y., et al., *Effect of dissolution pathways of polyacrylonitrile on the solution homogeneity: Thermodynamic- or kinetic-controlled dissolution.* Polymer, 2020. **205**.
65. Newcomb, B.A., et al., *Polyacrylonitrile solution homogeneity study by dynamic shear rheology and the effect on the carbon fiber tensile strength.* Polymer Engineering & Science, 2016. **56**(3): p. 361-370.
66. Tan, L., A. Wan, and D. Pan, *Pregelled gel spinning of polyacrylonitrile precursor fiber.* Materials Letters, 2011. **65**(5): p. 887-890.
67. Chen, J., et al., *Effect of coagulation temperature on the properties of poly(acrylonitrile- itaconic acid) fibers in wet spinning.* Journal of Polymer Research, 2007. **14**(3): p. 223-228.
68. Chae, H.G., et al., *High strength and high modulus carbon fibers.* Carbon, 2015. **93**: p. 81-87.
69. Alarifi, I.M., W.S. Khan, and R. Asmatulu, *Synthesis of electrospun*

polyacrylonitrile- derived carbon fibers and comparison of properties with bulk form. PLOS ONE, 2018. **13**(8): p. e0201345.

70. Sada, K., K. Kokado, and Y. Furukawa, *Polyacrylonitrile (PAN)*, in *Encyclopedia of Polymeric Nanomaterials*, S. Kobayashi and K. Müllen, Editors. 2015, Springer Berlin Heidelberg: Berlin, Heidelberg. p. 1745-1750.
71. Sagawa, N. and T. Shikata, *Are all polar molecules hydrophilic? Hydration numbers of nitro compounds and nitriles in aqueous solution.* Physical Chemistry Chemical Physics, 2014. **16**(26): p. 13262-13270.
72. Lee, B.-S., et al., *An effective method for manufacturing hollow carbon nanofibers and microstructural analysis.* Macromolecular Research, 2012. **20**(6): p. 605-613.
73. Yang, H.-S., et al., *Electrochemical wet-spinning process for fabricating strong PAN fibers via an in situ induced plasticizing effect.* Polymer, 2020. **202**.
74. Lee, B.-S., et al., *Dendrite Suppression Membranes for Rechargeable Zinc Batteries.* ACS Applied Materials & Interfaces, 2018. **10**(45): p. 38928-38935.
75. Venkatesan, S.v., et al., *Evolution of water sorption in catalyst coated membranes subjected to combined chemical and mechanical degradation.* Physical Chemistry Chemical Physics, 2015. **17**(21): p. 13872-13881.
76. Lim, H. and S.W. Hoag, *Plasticizer Effects on Physical–Mechanical Properties of Solvent Cast Soluplus® Films.* AAPS PharmSciTech, 2013. **14**(3): p. 903-910.
77. Rozanski, A. and A. Galeski, *Controlling Cavitation of Semicrystalline Polymers during Tensile Drawing.* Macromolecules, 2011. **44**(18): p. 7273-7287.
78. Bajaj, P., D.K. Paliwal, and A.K. Gupta, *Acrylonitrile–acrylic acids copolymers. I. Synthesis and characterization.* Journal of Applied Polymer Science, 1993. **49**(5): p. 823-833.
79. Ying, L., C. Hou, and W. Fei, *Diffusion coefficient of DMSO in polyacrylonitrile fiber formation.* Journal of Applied Polymer Science, 2006. **100**(6): p. 4447-4451.
80. Ebdon, J., T. Huckerby, and T. Hunter, *Free-radical aqueous slurry*

polymerizations of acrylonitrile: 1. End-groups and other minor structures in polyacrylonitriles initiated by ammonium persulfate/sodium metabisulfite. Polymer, 1994. **35**(2): p. 250-256.

81. Brandrup, J., J. Kirby, and L. Peebles Jr, *On the chromophore of polyacrylonitrile. III. The mechanism of ketone formation in polyacrylonitrile.* Macromolecules, 1968. **1**(1): p. 59-63.
82. Eom, Y. and B.C. Kim, *Solubility parameter-based analysis of polyacrylonitrile solutions in N,N-dimethyl formamide and dimethyl sulfoxide.* Polymer, 2014. **55**(10): p. 2570-2577.
83. Sebesta, F., et al., *Evaluation of polyacrylonitrile (PAN) as a binding polymer for absorbers used to treat liquid radioactive wastes*. 1995, Sandia National Labs.
84. Singhal, A., et al., *UV-shielding transparent PMMA/In2O3 nanocomposite films based on In2O3 nanoparticles.* RSC Advances, 2013. **3**(43).
85. Bajaj, P., R. Chavan, and B. Manjeet, *Saponification kinetics of acrylonitrile terpolymer and polyacrylonitrile.* Journal of Macromolecular Science—Chemistry, 1985. **22**(9): p. 1219-1239.
86. Easter, P.A. and D.M. Taylor, *Azine bridge formation during the electrografting of acrylonitrile.* Journal of Polymer Science Part A: Polymer Chemistry, 2009. **47**(6): p. 1685-1695.
87. Lee, S., et al., *Structural Evolution of Polyacrylonitrile Fibers in Stabilization and Carbonization.* Advances in Chemical Engineering and Science, 2012. **02**(02): p. 275-282.
88. Bartzis, V. and I.E. Sarris, *A theoretical model for salt ion drift due to electric field suitable to seawater desalination.* Desalination, 2020. **473**.
89. Ahn, H., et al., *Moisturized Polyacrylonitrile Copolymer for Stronger Precursor Fibers.* ACS Applied Polymer Materials, 2021. **3**(12): p. 6285-6293.
90. Wang, M., et al., *SAXS and WAXD study of periodical structure for polyacrylonitrile fiber during coagulation.* Polymers for Advanced Technologies, 2015. **26**(2): p. 136-141.
91. Li, X.-y., et al., *WAXD/SAXS study and 2D fitting (SAXS) of the microstructural evolution of PAN-based carbon fibers during the pre-*

oxidation and carbonization process. New Carbon Materials, 2017. **32**(2): p. 130-136.

92. Tsai, J.-S. and C.-H. Lin, *The effect of molecular weight on the cross section and properties of polyacrylonitrile precursor and resulting carbon fiber.* Journal of Applied Polymer Science, 1991. **42**(11): p. 3045-3050.
93. Knudsen, J., *The influence of coagulation variables on the structure and physical properties of an acrylic fiber.* Textile Research Journal, 1963. **33**(1): p. 13-20.
94. Minagawa, M. and T. Iwamatsu, *Relation between the thermal behavior of polyacrylonitrile and polymerization factors.* Journal of Polymer Science: Polymer Chemistry Edition, 1980. **18**(2): p. 481-494.
95. Gong, Y., et al., *In-situ microstructural changes of polyacrylonitrile based fibers with stretching deformation.* Polymer, 2014. **55**(16): p. 4270-4280.
96. Hinrichsen, G. *Structural changes of drawn polyacrylonitrile during annealing*. in *Journal of Polymer Science Part C: Polymer Symposia*. 1972. Wiley Online Library.
97. Karacan, I. and G. Erdogan, *The influence of thermal stabilization stage on the molecular structure of polyacrylonitrile fibers prior to the carbonization stage.* Fibers and Polymers, 2012. **13**(3): p. 295-302.
98. Liu, L., et al., *Investigation of surface properties of pristine and γ-irradiated PAN-based carbon fibers: Effects of fiber instinct structure and radiation medium.* Applied Surface Science, 2015. **337**: p. 241-248.
99. Zhu, C., et al., *A small-angle X-ray scattering study and molecular dynamics simulation of microvoid evolution during the tensile deformation of carbon fibers.* Carbon, 2012. **50**(1): p. 235-243.
100. Mengfan, W., et al., *SAXS and WAXD study of periodical structure for polyacrylonitrile fiber during coagulation.* Polymers for Advanced Technologies, 2015. **26**(2): p. 136-141.
101. Bajaj, P., D.K. Paliwal, and A.K. Gupta, *Influence of metal ions on structure and properties of acrylic fibers.* Journal of Applied Polymer Science, 1998. **67**(9): p. 1647-1659.
102. Mittal, J., et al., *Post spinning treatment of PAN fibers using succinic acid to produce high performance carbon fibers.* Carbon, 1998. **36**(7-8): p. 893-

897.

103. Chen, J. and I. Harrison, *Modification of polyacrylonitrile (PAN) carbon fiber precursor via post-spinning plasticization and stretching in dimethyl formamide (DMF).* Carbon, 2002. **40**(1): p. 25-45.

104. Fakhrhoseini, S.M., H. Khayyam, and M. Naebe, *Chemically Enhanced Wet-Spinning Process to Accelerate Thermal Stabilization of Polyacrylonitrile Fibers.* Macromolecular Materials and Engineering, 2018. **303**(8).

105. Eslami Farsani, R., A. Shokuhfar, and A. Sedghi, *Fabrication of carbon fibres from wet-spun commercial polyacrylonitrile fibres.* Fibre Chemistry, 2006. **38**(5): p. 383-386.

106. Phadke, M.A., et al., *Poly(acrylonitrile) ultrafiltration membranes. I. Polymer-salt-solvent interactions.* Journal of Polymer Science Part B: Polymer Physics, 2005. **43**(15): p. 2061-2073.

107. Beauchamp, D.L. and M. Khajehpour, *The effect of lithium ions on the hydrophobic effect: does lithium affect hydrophobicity differently than other ions?* Biophys Chem, 2012. **163-164**: p. 35-43.

108. Xin, N., et al., *Solubilities of six lithium salts in five non-aqueous solvents and in a few of their binary mixtures.* Fluid Phase Equilibria, 2018. **461**: p. 1-7.

109. Tasaki, K., et al., *Solubility of lithium salts formed on the lithium-ion battery negative electrode surface in organic solvents.* Journal of The Electrochemical Society, 2009. **156**(12): p. A1019.

110. Ong, M.T., et al., *Lithium ion solvation and diffusion in bulk organic electrolytes from first-principles and classical reactive molecular dynamics.* J Phys Chem B, 2015. **119**(4): p. 1535-45.

111. Zeng, X., et al., *Diffusion Mechanism of As-spun Polyacrylonitrile Fiber in a Dimethyl Sulfoxide-Water Coagulation Bath.* Journal of Macromolecular Science, Part A, 2006. **43**(11): p. 1711-1720.

112. Martinez, R.J. and J. Farrell, *Quantifying Electric Field Enhancement of Water Dissociation Rates in Bipolar Membranes.* Industrial & Engineering Chemistry Research, 2019. **58**(2): p. 782-789.

113. Kampalanonwat, P. and P. Supaphol, *Preparation and adsorption behavior of aminated electrospun polyacrylonitrile nanofiber mats for heavy metal*

ion removal. ACS Appl Mater Interfaces, 2010. **2**(12): p. 3619-27.

114. Arbab, S., et al., *Designing index of void structure and tensile properties in wet-spun polyacrylonitrile (PAN) fiber. I. Effect of dope polymer or nonsolvent concentration.* Journal of Applied Polymer Science, 2008. **109**(6): p. 3461-3469.
115. Tan, L., D. Pan, and N. Pan, *Thermodynamic study of a water–dimethylformamide–polyacrylonitrile ternary system.* Journal of Applied Polymer Science, 2008. **110**(6): p. 3439-3447.
116. Dong, R., et al., *Morphology control of polyacrylonitrile (PAN) fibers by phase separation technique.* Journal of Polymer Science Part B: Polymer Physics, 2009. **47**(3): p. 261-275.
117. Dong, R., et al., *Viscometric measurement of the thermodynamics of PAN terpolymer/DMSO/water system and effect of fiber-forming conditions on the morphology of PAN precursor.* Journal of Polymer Science Part B: Polymer Physics, 2008. **46**(19): p. 1997-2011.
118. Cheng, L., Q. Ouyang, and H.-J. Wang, *Effect of Water on the Viscosity Properties of Polyacrylonitrile Solution in Dimethylsulfoxide.* Journal of Macromolecular Science, Part B, 2009. **48**(3): p. 617-625.
119. Ilyin, S.O., V.G. Kulichikhin, and A.Y. Malkin, *Unusual rheological effects observed in polyacrylonitrile solutions.* Polymer Science Series A, 2013. **55**(8): p. 503-509.
120. Arbab, S., et al., *Exploring the effects of non-solvent concentration, jet-stretching and hot-drawing on microstructure formation of poly(acrylonitrile) fibers during wet-spinning.* Journal of Polymer Research, 2010. **18**(6): p. 1343-1351.
121. Bahrami, S.H., P. Bajaj, and K. Sen, *Effect of coagulation conditions on properties of poly(acrylonitrile-carboxylic acid) fibers.* Journal of Applied Polymer Science, 2003. **89**(7): p. 1825-1837.
122. Singhal, A., et al., *UV-shielding transparent PMMA/In2O3 nanocomposite films based on In2O3 nanoparticles.* RSC Advances, 2013. **3**(43): p. 20913-20921.
123. Bajaj, P., R.B. Chavan, and B. Manjeet, *Saponification Kinetics of Acrylonitrile Terpolymer and Polyacrylonitrile.* Journal of Macromolecular

Science: Part A - Chemistry, 1985. **22**(9): p. 1219-1239.

124. Frost, R.L. and A.M. Vassallo, *The Dehydroxylation of the Kaolinite Clay Minerals using Infrared Emission Spectroscopy.* Clays and Clay Minerals, 1996. **44**(5): p. 635-651.

125. Eom, Y., C. Kim, and B.C. Kim, *Effects of physical association through nitrile groups on the MWD-dependent viscosity behavior of polyacrylonitrile solutions.* Macromolecular Research, 2017. **25**(3): p. 262-269.

126. Tan, L., S. Liu, and D. Pan, *Water effect on the gelation behavior of polyacrylonitrile/dimethyl sulfoxide solution.* Colloids and Surfaces A: Physicochemical and Engineering Aspects, 2009. **340**(1-3): p. 168-173.

127. Yang, H., R. Cheng, and Z. Wang, *A quantitative analyses of the viscometric data of the coil-to-globule and globule-to-coil transition of poly(N-isopropylacrylamide) in water.* Polymer, 2003. **44**(23): p. 7175-7180.

128. Yu, M., et al., *Influence of Precursor Properties on the Thermal Stabilization of Polyacrylonitrile Fibers.* Polymer Bulletin, 2006. **57**(5): p. 757-763.

129. Lu, J., et al., *Microstructure and properties of polyacrylonitrile based carbon fibers.* Polymer Testing, 2020. **81**: p. 106267.

130. An, M., et al., *An in situ small-angle X-ray scattering study of the structural effects of temperature and draw ratio of the hot-drawing process on ultra-high molecular weight polyethylene fibers.* RSC Advances, 2016. **6**(56): p. 51125-51134.

131. Tang, H., et al., *Investigation of Voids in Polyacrylonitrile Fibers by USAXS and SAXS.* Chemical Research in Chinese Universities, 2019. **35**(6): p. 1070-1075.

132. Pauw, B.R., et al., *Analysing the nanoporous structure of aramid fibres.* Journal of Applied Crystallography, 2010. **43**(4): p. 837-849.

133. Qiao, M., et al., *Study on the Changes of Structures and Properties of PAN Fibers during the Cyclic Reaction in Supercritical Carbon Dioxide.* Polymers, 2019. **11**(3): p. 402.

134. Chen, J., et al., *Study on the Coagulation Mechanism of Wet-Spinning PAN Fibers.* Journal of Polymer Research, 2006. **13**(6): p. 515-519.

135. Tan, L., D. Pan, and N. Pan, *Thermodynamic study of a water-dimethylformamide-polyacrylonitrile ternary system.* Journal of Applied

Polymer Science, 2008. **110**(6): p. 3439-3447.

136. McMurry, J.E., *Organic Chemistry.* 2015: Cengage.

137. Liu, C., et al., *Evaluation of different methods for the determination of the plateau modulus and the entanglement molecular weight.* Polymer, 2006. **47**(13): p. 4461-4479.

138. Ahn, H., et al., *Microstructure Analysis of Drawing Effect and Mechanical Properties of Polyacrylonitrile Precursor Fiber According to Molecular Weight.* Polymers (Basel), 2022. **14**(13).

139. Cleland, R.L. and W.H. Stockmayer, *An intrinsic viscosity-molecular weight relation for polyacrylonitrile.* Journal of Polymer Science, 1955. **17**(86): p. 473-477.

140. Ilyin, S.O., et al., *Viscosity of polyacrylonitrile solutions: The effect of the molecular weight.* Polymer Science Series A, 2015. **57**(4): p. 494-500.

141. Liu, Q., et al., *Spinnability of Polyacrylonitrile Gel Dope in the Mixed Solvent of Dimethyl Sulfoxide/Dimethylacetamide and Characterization of the Nascent Fibers.* Polymer Science, Series A, 2018. **60**(5): p. 638-646.

142. Ying, L., C. Hou, and W. Qun, *Rheological behavior of acrylonitrile/ammonium acrylate copolymer solutions.* Journal of Applied Polymer Science, 2007. **103**(4): p. 2320-2324.

143. Devasia, R., C.P.R. Nair, and K.N. Ninan, *Temperature and shear dependencies of rheology of poly(acrylonitrile-co-itaconic acid) dope in DMF.* Polymers for Advanced Technologies, 2008. **19**(12): p. 1771-1778.

144. Devasia, R., C.P. Reghunadhan Nair, and K.N. Ninan, *Rheological Behavior of Dope Solutions of Poly(acrylonitrile-co-itaconic acid) inN,N-dimethylformamide: Effect of Polymer Molar Mass.* Journal of Macromolecular Science, Part A, 2008. **45**(3): p. 248-254.

145. Mahmod, D.S.A., et al., *Effect of the solvent type on the formation and physical properties of polyacrylonitrile fibers via a solvent-free coagulation bath.* Journal of Applied Polymer Science, 2011. **121**(4): p. 2467-2472.

146. Fernandez-Ballester, L., et al., *Effect of Long Chains on the Threshold Stresses for Flow-Induced Crystallization in iPP: Shish Kebabs vs Sausages.* Macromolecules, 2012. **45**(16): p. 6557-6570.

147. Kida, T., et al., *Improving the strength of polyethylene solids by simple controlling of the molecular weight distribution.* Polymer, 2021. **218**.
148. Long, C., et al., *Molecular weight distribution shape approach for simultaneously enhancing the stiffness, ductility and strength of isotropic semicrystalline polymers based on linear unimodal and bimodal polyethylenes.* Polymer, 2023. **275**.
149. Tan, L., J. Pan, and A. Wan, *Shear and extensional rheology of polyacrylonitrile solution: effect of ultrahigh molecular weight polyacrylonitrile.* Colloid and Polymer Science, 2011. **290**(4): p. 289-295.
150. Yang, T., et al., *Rheological behaviour of polyacrylonitrile in an ionic liquid solution.* 2010.
151. Kunzmann, C., et al., *Microscopic investigation of polyacrylonitrile fiber fibrils separated by ultrasonic etching.* Journal of Materials Science, 2017. **53**(6): p. 4693-4704.
152. Wang, Q., et al., *Fibrils separated from polyacrylonitrile fiber by ultrasonic etching in dimethylsulphoxide solution.* Journal of Polymer Science Part B: Polymer Physics, 2010. **48**(5): p. 617-619.
153. Long, C., et al., *Molecular Weight Distribution Shape Dependence of the Crystallization Kinetics of Semicrystalline Polymers Based on Linear Unimodal and Bimodal Polyethylenes.* ACS Applied Polymer Materials, 2023. **5**(4): p. 2654-2663.
154. Song, S., et al., *Effect of small amount of ultra high molecular weight component on the crystallization behaviors of bimodal high density polyethylene.* Polymer, 2008. **49**(12): p. 2964-2973.
155. Balzano, L., S. Rastogi, and G. Peters, *Self-Nucleation of Polymers with Flow: The Case of Bimodal Polyethylene.* Macromolecules, 2011. **44**(8): p. 2926-2933.
156. Kamide, K., H. Iijima, and S. Matsuda, *Thermodynamics of formation of porous polymeric membrane by phase separation method I. Nucleation and growth of nuclei.* Polymer journal, 1993. **25**(11): p. 1113-1131.

Korean abstract

최근 폴리아크릴로나이트릴(PAN) 섬유가 탄소섬유의 전구체로 사용되는 것이 알려지면서 많은 관심을 받고 있습니다. 탄소섬유는 다양한 분야에서 높은 강도 대비 경량성을 갖는 물성으로 인해 널리 사용되고 있습니다. 그러나 탄소섬유의 성능 요구가 증가하는 반면, 물성 개선에 한계가 있어 PAN 섬유의 기계적 특성 향상 연구가 필요합니다. 이에 본 연구에서는 전기화학적 습식 방사를 도입하여 PAN 섬유의 기계적 특성을 향상시키는 새로운 방법을 개발하였습니다. 또한, PAN 습식 방사와 전기화학적 습식 방사에서 다양한 변수를 최적화하여 고강도 PAN 섬유를 제조하고자 하였습니다.

우선, 양이온이 체인 끝에 함유된 PAN 을 디자인하여 중합하고, 이를 섬유로 제조하였습니다. 제조된 섬유의 미세 구조와 기계적 특성을 평가하여 전기화학적 습식 방사에 적합한 PAN 섬유임을 실험적으로 확인하였습니다. 이온화된 PAN 은 응고 과정에서 용매 및 비용매의 확산 속도를 변화시키고, PAN 섬유 내 공극을 최소화하며 기계적 특성을 향상시킵니다. 이후에는 일반적으로 사용되는 이온화되지 않은 PAN 으로는 전기화학적 습식 방사가 어려워 리튬 염을 첨가하여 전기 전도도를 갖는 PAN 방사 용액을 제조하였습니다. 리튬 염이 포함된 방사 용액은 전압을 가하면 이온화가 가속화되어 전기화학 반응에 의한 물성 증가 효과를 극대화합니다. 또한, 다양한 리튬 염 농도를 통해 방사 용액 내 최적의 리튬 염 농도를 제시하였습니다.

PAN 섬유가 수분에 미치는 영향을 조사하기 위해 균일하게 수증기를 PAN 에 도포하였습니다. 균일하게 수증기로 도포된 PAN 을 일반적인 습식 방사와 전기화학적 습식 방사로 섬유를 제조하였습니다. 소량의 수분은 제조된 섬유 내 공극을 최소화하고 기계적 특성을 향상시켰습니다. 전기화학적 습식 방사에서는 더 많은 수분을 통해 기계적 특성이 더욱 향상되었습니다.

또한, PAN 섬유의 기계적 특성과 방사성을 향상시키기 위해 바이모달 분자량 분포를 갖는 PAN을 디자인하였습니다. 바이모달 분자량 PAN은 저분자량 PAN 으로 인해 점도가 감소하고 방사성이 증가하였습니다. 또한, 고분자량 PAN 과 저분자량 PAN 의 응고 과정 차이로 인해 섬유 내 결정 구조를 개선하고 기계적 특성을 향상시켰습니다. 다양한 혼합 비율과 분자량 간 비율의 바이모달 분자량 분포 PAN 섬유를 제조하여 적절한 혼합 비율과 분자량 간 비율을 확인하였습니다. 이를 통해, 방사성과 기계적 특성이 모두 향상된 바이모달 분자량 분포 PAN 섬유를 제조하였습니다.

핵심어: PAN 섬유, 전기화학적 습식 방사 공정, 기계적 특성, 미세구조, 바이모달 분자량 분포, 방사성

학번: 2017-27050